

Modeling of multi-scale transport phenomena in shale gas production — A critical review



Hui Wang^{a,1}, Li Chen^{b,1}, Zhiguo Qu^{b,*}, Ying Yin^b, Qinjun Kang^c, Bo Yu^d, Wen-Quan Tao^b

^a School of Aeronautics, Northwestern Polytechnical University, Xi'an, Shaanxi 710072, China

^b MOE Key Laboratory of Thermo-Fluid Science and Engineering, School of Energy and Power Engineering, Xi'an Jiaotong University, Xi'an, Shaanxi 710049, China

^c Earth and Environmental Sciences Division, Los Alamos National Laboratory, Los Alamos, NM 87545, USA

^d Mechanical Engineering College, Beijing Institute of Petrochemical Technology, Beijing 102617, China

HIGHLIGHTS

- Multi-scale transport phenomena in shale gas transport is introduced.
- Multi-scale simulation models describing shale transport are reviewed.
- Information exchanging among micro/meso/macrosopic methods is analyzed.
- Shale gas production genome model is put forward and clarified.
- Shale gas production forecasts depend on multi- scale and -physics models.

ARTICLE INFO

Keywords:

Multi-scale
Computational modeling
Adsorption and desorption
Shale gas production genome

ABSTRACT

Shale gas, although unconventional, is a prospective clean energy source. Shale gas production is a complex multi-scale process with its spatial size ranging from the nanoscale to kilometer-scale. During shale production, the gas transport process involves the diffusion of dissolved gas molecules into the matrix bulk, desorption of adsorbed gas from the micropore surface, Knudsen diffusion and slip flow of free gas in the pore, and Darcy flow or even high-speed non-Darcy flow of free gas in the fracture network. Accordingly, understanding the shale gas transport process in the shale reservoirs poses a long-standing problem to researchers and engineers. Computational modeling offers an opportunity to effectively reveal the gas multi-scale transport mechanisms and accurately predict the amount of shale production. In this review, the shale gas transport process during shale gas production is firstly introduced. Thereafter, the multi-scale transport phenomena involving shale gas molecule desorption from the shale matrix at the atomic and molecular level, diffusion in the nanopore, diffusion and seepage into the micropore, and convection and mass flow in the mesoscopic pores and macropore are elucidated. Moreover, the corresponding multi-scale simulation models that describe the above phenomena and shale production are explained. The shale gas production genome model, which provides insights into the entire process of the shale gas production model, is proposed and clarified according to the multi-scale simulation models used in the shale gas production prediction. The shale gas production genome model is convenient for elucidating shale transport mechanisms and guiding shale gas reservoir exploitation.

1. Introduction

In recent years, unconventional natural gas extraction has drawn considerable attention due to the shortage of global energy and the increasing demand for energy consumption worldwide [1–7]. As an important unconventional gas, shale gas, which refers to natural gas trapped inside fine grained sedimentary rocks called mudrocks

(mudstone or shale) that are rich source rocks for oil and gas, offers the advantages of high combustion value and environmental friendliness [8–10]. Shale gas is an abundant natural resource, with reserves of up to 7299 trillion cubic meters [11]. The “shale gas revolution” in North America has had a profound effect on global energy markets as well as those in the United States. The research and exploration of shale gas are increasingly common, and the number of published papers on shale gas

* Corresponding author.

E-mail address: zgqu@mail.xjtu.edu.cn (Z. Qu).

¹ These authors contributed equally to the work.

Nomenclature	
<i>Symbols</i>	
$a(t)$	Acceleration ($\text{m}\cdot\text{s}^{-2}$)
$A(\mathbf{q}, \mathbf{p})$	Physical property of a shale gas molecule at equilibrium
b_k	Klinkenberg's slippage factor
c	Coefficient ($c \approx 1$)
C	Gas concentration ($\text{mol}\cdot\text{m}^{-3}$)
d	Shale matrix spatial dimension (3 for shale gas)
DFT	Density functional theory
$D_{i,j}$	Binary diffusivity of species i and j
$D_{i,kn}$	Knudsen diffusivity of species i
D_s	Shale gas self-diffusion
E	Total energy of the system
$E(\mathbf{q}, \mathbf{p})$	Total energy including both potential and kinetic energies
f	Fugacity
f_c	Correction factor in Klinkenberg's slippage factor
f_i	Particle velocity distribution function
$f_i^{\text{eq}}(x, t)$	Equilibrium distribution function
\mathbf{F}	Linear (Darcy) drag force
F_i	Forcing term
FVM	Finite volume method
\mathbf{G}	External body forces
$GCMC$	Grand canonical Monte Carlo
\hat{H}	Hamiltonian operator
J_i^D	Diffusion flux
k	Boltzmann constant ($1.380649 \times 10^{-23}\text{J}\cdot\text{K}^{-1}$)
k_∞	Klinkenberg's corrected permeability
Kn	Knudsen number
LBM	Lattice Boltzmann method
m	Mass of shale gas molecule (kg)
MD	Molecular dynamics
M	Relative molecular mass ($\text{kg}\cdot\text{mol}^{-1}$)
M_a	Relative molecular mass of shale gas molecule
M_s	Substance amounts of a single crystal cell for shale matrix
n	Total number of constrained degrees for shale gas freedom
N	Total number of shale gas molecules
N_i	Number of shale gas molecules of components i
N_j	Number of shale gas molecules of components j
N_a	Number of structure cells
N_A	Avogadro's constant ($6.02 \times 10^{23} \text{ mol}^{-1}$)
$P(\mathbf{q}, \mathbf{p})$	Probability for the particular atom arrangement in a molecule
$p_{m \rightarrow n}^*$	Acceptance probabilities from m configuration to n configuration
p	Pressure (kPa)
\mathbf{p}	Momentum
q	Amount of adsorption ($\text{mol}\cdot\text{kg}^{-1}$)
\mathbf{q}	Coordinates of the shale gas molecule
q_i	Charge value for particle i (e)
q_j	Charge value for particle j (e)
<i>Greek</i>	
Q	Adsorption heat ($\text{kJ}\cdot\text{mol}^{-1}$)
r	Radius (m)
$r_i(t)$	Position of the center of mass position of shale gas molecule i at any time t
$r_i^i(t)$	Shale gas molecule position of component i at any time t
r_{ij}	Distance between i and j interacting atoms
S	Source
\mathbf{u}	Velocity vector ($\text{m}\cdot\text{s}^{-1}$)
V	Simulation volume (m^3)
t	Time (s)
T	Temperature (K)
z	Compressibility factor
<i>Superscripts</i>	
\wedge	Hamiltonian operator
i	Component
$*$	Probability
Eq	Equilibrium
<i>Subscripts</i>	
Excess	Excess amount
i	Interacting atoms or component
ff	Adsorbate-adsorbate
fs	Adsorbate-adsorbent
free	Free volume of a single crystal cell
j	Interacting atoms
m	Configuration m
n	Configuration n
s	Solid
$m \rightarrow n$	From configuration m to configuration n

has increased exponentially in recent years, as shown in Fig. 1.

The shale matrix porosity is relatively low (5–10%), and its permeability is of the extremely small order of nano-Darcy, with highly heterogeneous porous/fractured structures. Economically producing shale gas from such low-permeability formations is nearly impossible, and thus shale gas is often referred to as “unconventional” natural gas. Over recent decades, advanced techniques such as horizontal wells and hydraulic fracturing stimulations have been performed to increase the permeability of the shale formations by extending and/or widening the existing fractures and creating new ones through the injection of a pressurized fluid and proppants into the rock formation [12–14]. The

detailed comparisons of different production techniques can be found in Ref. [15]. Through these fractures, shale gas can flow from the shale matrix to the wellbore, allowing commercial exploitation of shale gas reservoirs. However, the process of shale gas production is still difficult, because the shale stratum exhibits complex petrophysical properties with abundant microscale and nanoscale pore throat structures [16]. The macroscopic gas transport properties namely, adsorption and desorption, diffusivity, and permeability, are dependent on shale microstructures, components and flow regimes [17,18]; these complex structures make the exploitation of shale gas difficult. A shale image obtained by a typical scanning electron microscope (SEM) is shown in

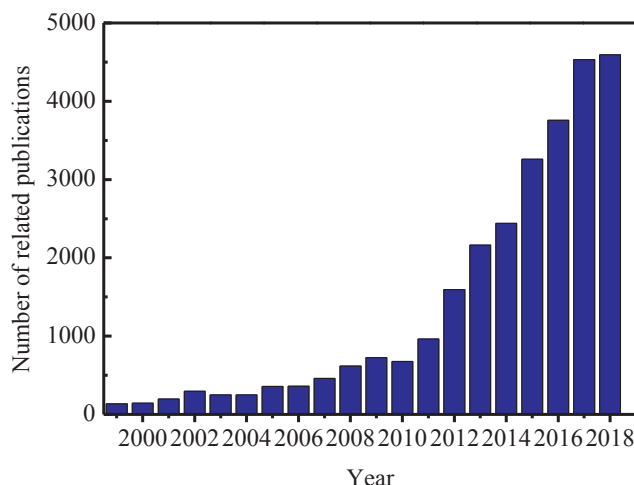


Fig. 1. Number of articles on the topic of shale gas during 1999–2018 from the web of science index; the number of published papers about shale gas increased exponentially from 1999 to 2018.

Fig. 2. Evidently, shale is a heterogeneous and anisotropic porous material; it contains inorganic matter, such as clay minerals (montmorillonite, chlorite, kaolinite, and illite), calcite, pyrite, quartz and organic matter (kerogen) [19]. Natural fractures and hydraulic fractures also exist in the shale matrix [19–21]. The composition proportion, porosity, pore size, *in-situ* pressure and temperature, permeability and adsorption capacity of shale gas reservoirs are summarized in Table 1.

A major component of shale gas is methane (CH_4) (> 94%), and small amounts of CO_2 , N_2 , H_2O , ethane (C_2H_6), and propane (C_3H_8) also exist [32,33]. Shale gas is widely distributed in the microscale and nanoscale pores of the shale matrix [34,35]. Shale gas is stored in shale reservoirs in different forms, including free gas, adsorbed gas, and dissolved gas [21]. Free gas refers to the gas stored in the void space of the shale matrix including pores, cracks, and natural fractures. Adsorbed gas refers to the gas adsorbed on the walls of matrix pores, and most is found in the surface of kerogen owing to its high affinity. Shale gas is also dissolved in water and oil, although only small amounts are dissolved because solubility of shale gas in water is very low ($0.007 \text{ g}\cdot\text{kg}^{-1}$ of water at the standard condition). Gas dissolved in kerogen also exists, and it has been confirmed as an important storage form that cannot be neglected [36,37]. Various storage forms, together with multi-scale porous systems, particularly those containing abundant nanosize pores, lead to strongly coupled multi-scale multiple physicochemical processes with non-continuum behaviors occurring during the shale gas extraction [21,38]. With the hydraulic fracturing operation, matrix-fracture coexist in the shale reservoirs, leading to

Table 1
Characteristics of shale gas reservoirs.

Properties	Values
Location	3 km below the surface, exhibiting a thickness of 20–150 m [23–25]
Contents [26]	Organic matter (OM) Clay minerals (16–33%) Quartz (37–59.3%) Calcite (1–5%)
Porosity	5–10% [27]
Permeability	10^{-27} to 10^{-15} m^2 [28]
Organic pores	< 10 nm in diameter
Temperature	150–200 °C [29]
Pressure	5–30 MPa in North America [30]
Adsorption capacity	0.50–3.41 $\text{cm}^3\cdot\text{g}^{-1}$ [31]

multi-scale porous systems including OM nanoscale pores; inorganic matter nano-, micro-, macro-scale pores; microscale natural fractures and meso- and macro-scale hydraulic fractures [19,21,39]. Thus, the transport space of shale gas ranges from the atomic level to the macropore level, as schematically shown in Fig. 3. The sub-processes involved include solid diffusion of dissolved gas in the bulk OM, desorption of shale gas from the walls of nano and micro pores, particularly OM pores, Knudsen diffusion, transition flow, slip flow, and Darcy flow. The transport processes are further complicated by co-existing processes such as Klinkenberg's effect in small pores, adsorbed layer on the solid surface, deformation of rock and proppant due to stress change, and rock dissolution due to acid injection to open the fractures near the wellbore. Therefore, shale gas production is a complex multi-scale process coupled with multiple mechanisms [34,40–42]. Owing to the low pressure in the fractures, the equilibrium state in the shale matrix is broken, and the generation, migration, and production of shale gas consist of the following sub-processes, as shown in Fig. 3: (1) at the nanoscale, shale gas begins to desorb from the internal surface of nano and micro pores, and travel in the nanopores with Knudsen diffusion as the dominant transport mechanism. The concentration differs between the surface and the kerogen bulk, and the dissolved gas begins to move toward the internal surface of the nanopores by solid diffusion; (2) at the microscale, Knudsen diffusion and viscous flow of shale gas in the pore network of the shale matrix; (3) at the mesoscale, the gas travels within the fracture network to the wellbore mainly by Darcy's flow; and (4) at the macroscale, the gas in the shale matrix migrates to the reservoir system (wellbore).

Experimental studies on shale gas production have been widely reported [43–46]; however, most experimental investigations simply focus on shale matrix information, for example, adsorption capacity [47,48], and geometrical characteristics of shale matrix [19,49–56], such as porosity [57–59], pore scale and volume [60,61], surface area

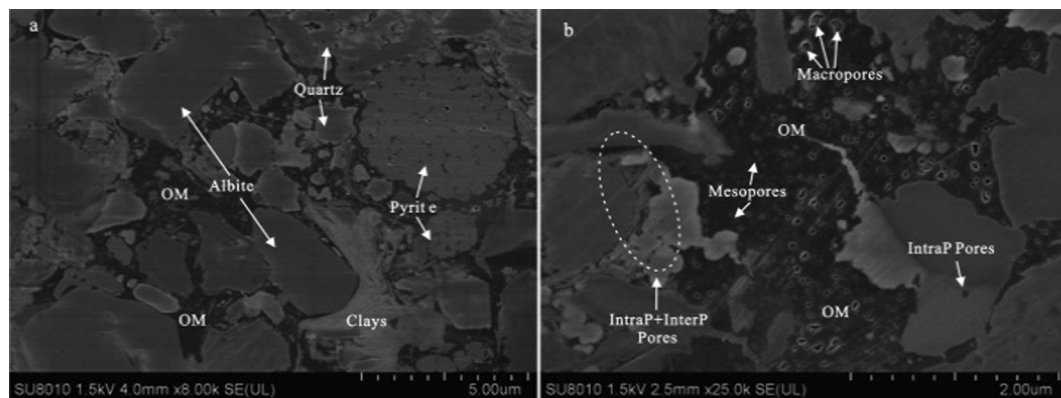


Fig. 2. SEM image of shale matrix; the inorganic matter [clay minerals (montmorillonite, chlorite, kaolinite, and illite), calcite, pyrite, quartz] and organic matter (kerogen), Intraparticle/Interparticle (IntraP/Interp) pores, mesopore and macropore are existed in the shale sample. Reprinted with permission from Ref. [22].

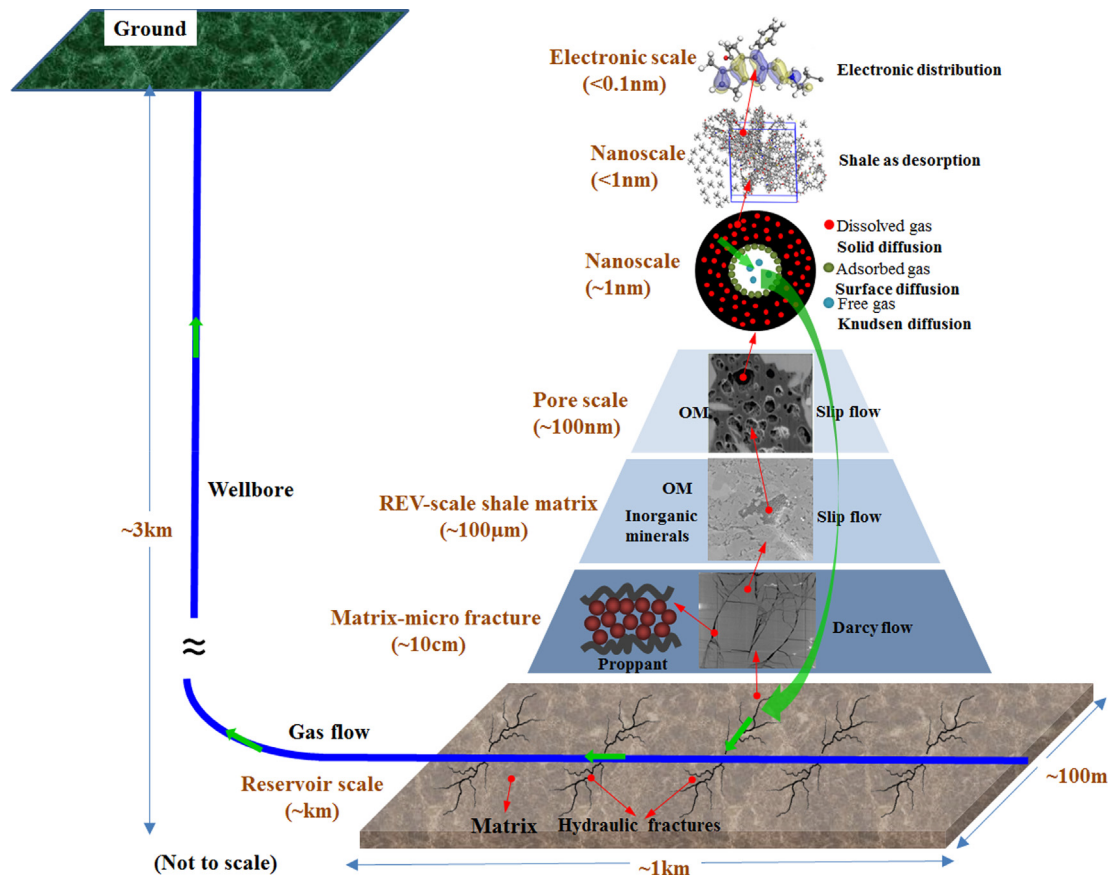


Fig. 3. Multiscale physicochemical processes during shale gas extraction. From the electronic distribution during the desorption process, desorption in the shale crystal, solid diffusion and Knudsen diffusion occurring in the nanosize OM pores, to the large-scale migration of shale gas in the shale reservoirs, the length scale covered exceeds 12 magnitudes. Multiple physicochemical processes simultaneously take place at different scales within the multiscale spanned exploitation, including solid diffusion in solid organic matter, desorption from the pore walls, surface diffusion, Knudsen diffusion, slip flow and Darcy flow. The existence of a two-phase (gas and water) flow, chemical reactions, solid–fluid interaction, and proppant particle deformation make the processes even more complicated.

and pore size distribution [36,62]. In fact, numerous factors, influence the pore types and networks in mudrocks, including rock composition, grain size, spatial arrangement of hard or compliant phases, burial depth, pressure, temperature, mechanical compaction and diagenesis [19,49–56] and permeability [34,57,63,64]. To date, the pore properties and their evolution are still incompletely understood and need to be further studied. External factors, such as pressure [26,65–68], temperature [26,66–70], depth range [67], and shale matrix contents [26,66–68,71], which have considerable effects on the amount of shale gas adsorption capacity and production, have also been experimentally investigated. It has been found that the absolute adsorption amount increases with the pressure, whereas it decreases with the increase in temperature [66–68,70,72], and the maximum CH₄ sorption capacities of organic shale increase with geological depth [67]. The absolute adsorption amount of shale gas increases with the organic carbon content, but there is no distinct association with the contents of clay minerals [73]. Moreover, these studies summarized the factors that influence the rate of shale gas production [68,74] and concluded that the portions of adsorbed gas and dissolved gas will not be producible once the shale gas pressure exceeds a constant value. The functions of the adsorbed, free, and dissolved gas for shale gas production also vary with the shale gas temperature and pressure [75].

In fact, experimental methods are generally expensive and time-consuming; they only obtain information pertaining to the fluid transport characteristic of shale gas under certain conditions. For example, Merey et al. [76] analyzed the experimental adsorption uncertainty on shale gas production. They found that experimental adsorption uncertainty influences the adsorbed shale gas amount. Excluding these

methods, experiments have some inherent limitations. For example, highly permeable shale samples do not exhibit good mechanical stability; consequently, they often fail during plug drilling as samples are prepared [77].

The computer simulation method can overcome the aforementioned limitations of experimental methods in predicting shale gas production. Some researchers have summarized the shale matrix mass transfer process in the simulation modeling method, and their main focus is only limited to certain segments of the shale production process. Wang et al. [78] reviewed the shale gas adsorption and desorption, and diffusion processes in the shale matrix calculated by different molecular simulation models at the micro level. Liu et al. [79] recently summarized molecular simulations in the phase behavior and compared the deviated phase behavior in the shale matrix nanopores. Wang et al. [80] reviewed several boundary conditions and relaxation times used in the Lattice Boltzmann method (LBM) models for gas flow at the mesoscopic level. At the macroscopic level, the simulation methods pertaining to the multiphase flow [81], fluid transport characterization [77,82], effect of water on shale gas transport behavior [83], and multi-scale fluid flow [84] have been summarized. Hyman et al. [85] summarized discrete fracture network models, which are used to predict the production of a hydraulically fractured well from a fracture network at the field scale; then, triaxial fracture experiments and a finite-discrete element model were also adopted at the core scale. Lastly, the LBM was adopted to study the shale flow and transport phenomena in the shale matrix, including multi-phase flow and fluids mixing. They found that the mechanistic integration of these multiple scales is required for accurate predictions of production from unconventional reservoirs.

Generally, a deep knowledge of the shale gas transport process in the shale matrix pores is important to achieve more accurate predictions of shale gas production from wells. Understanding such processes will facilitate more thorough and cost-effective recovery of hydrocarbons from tight reservoirs. However, the process of gas desorption and production from the matrix is not yet well understood, specifically the multiscale process from the atomic to the macropore level.

As stated above, comprehensive review articles about the shale gas transport from the electronic to the macro level have not been reported. The major aims of the present study, therefore, are to investigate such multiscale multiple physicochemical processes and main methods that are used to describe the complex multi-scale transport phenomena during the shale gas extraction. Thus, the whole gas exploitations from the electronic to macro scales in kilometers are referred. In this review, the shale gas production process at different scale levels is introduced. Thereafter, the characterization of shale gas transport at each level and simulation methods for shale gas adsorption and desorption, diffusion, slip flow, and seepage are presented in detail. Widely adopted models used to describe the shale gas transport process [the density functional theory (DFT), grand canonical Monte Carlo (GCMC), molecular dynamics (MD) simulation, LBM method, and finite volume (FVM) and empirical correlation methods] at all scales are presented. Finally, to predict the rate of shale gas production in an unknown shale gas reservoir, the shale gas production genome model is proposed. The present study is expected to provide a fundamental understanding of the multiscale multiple physicochemical processes that occur within the shale matrix and serve as an essential starting point for continuing the research at the reservoir scale which is highly dependent on accurate transport properties and should encompass properly the transport mechanism at the nano-, micro-, meso-, and macro scales.

It should be noted that this review is focused on fluid flow and mass transport during shale gas extraction. Therefore, issues during hydraulic fracturing such as pore properties [86], fracture propagation [12,87–89], proppant migration [90], and pore network [91] are not examined in depth, although they are critically important for shale gas production.

2. Adsorption and desorption of shale gas at the electronic level

2.1. General knowledge

Some quantities of shale gas molecules that are in the state of adsorption or desorption equilibrium at the atomic level in the shale matrix crystal; the location of these molecules in the shale matrix is regarded as the adsorption site. The process of gas molecule adsorption or desorption in the shale matrix crystal can be depicted by the quantum mechanics (QM) method, which visualizes the electronic movement at the electronic level that cannot be captured by molecular mechanics. The QM method can offer information pertaining to the physical and chemical interactions involved in gas adsorption [92]. The method includes the ab initio, semi-empirical orbit, and DFT techniques. The DFT, as the most typical technique in QM, is widely used in depicting the shale gas adsorption and desorption process [93]. The initial configuration for DFT calculation can be obtained from the snapshot calculated by using GCMC and MD method.

2.2. Density functional theory (DFT) method

The information pertaining to the nuclear atomic numbers along with the total number of electrons during shale gas adsorption and desorption is afforded by the electron density in the physical observable-electron density. It determines the Hamiltonian operator during solving the Schrödinger equation, which can be expressed as

$$\hat{H}\Psi = E\Psi \quad (1)$$

where \hat{H} is the Hamiltonian operator, Ψ is the wave function, and E is the total energy of the system, respectively. The detailed calculation process of the Schrödinger equation for obtaining the electron density in the DFT method is found in Refs. [94–96]. The DFT method can be applied to investigate the adsorption enthalpy of shale gas adsorption in the shale matrix, as well as the electronic properties and shale matrix structures [97].

2.3. Density functional theory calculations applied to shale matrix

Before any information regarding the characteristics of the shale

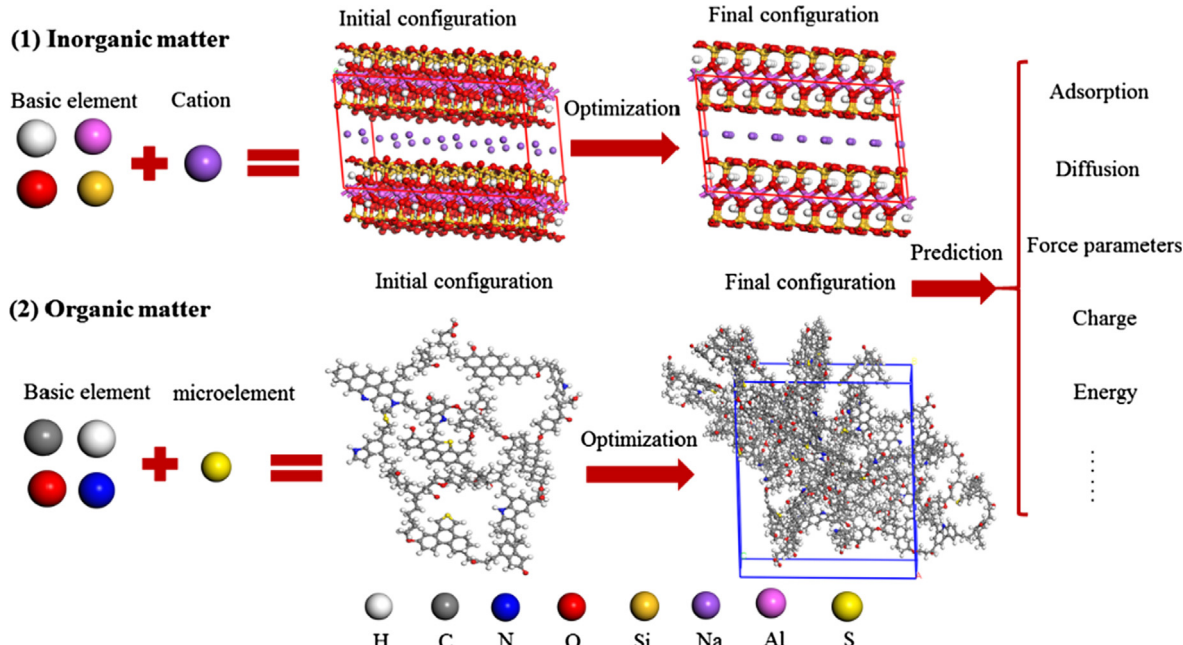


Fig. 4. Configuration optimization process of inorganic and organic matters; the inorganic and organic matters contains the carbon, oxygen, hydrogen, and different microelements (sulfur).

matrix can be obtained, its structure should be determined. The complex structure of the shale matrix is composed of different atoms; thus, it can be built and visualized using software, such as Materials Studio (MS) [98] and VESTA [99,100]. However, structures built by the software do not always satisfy the criteria for real shale matrix structures. Thus, the structure of the shale matrix is optimized by adopting the DFT method to satisfy the criteria for real shale matrix structures [101], as shown in Fig. 4. For example, the single shale matrix [102–104] and the complex inorganic–organic composite matrix (silica - kerogen interfaces) are optimized by the DFT method [105]. The function of the B3LYP functional [106] with 6-31G (d) and 6-311G (d, p) [107] basis set together with the generalized gradient approximation functional Perdew-Burke-Ernzerhof [108] is widely used during geometry optimization. Then, the optimized shale matrix structure can be treated as the input parameter to calculate the value of the adsorption amount and adsorption heat in the GCMC method along with the diffusion in the MD method. The values of the Lennard-Jones (L-J) potential [109,110] and the charges of adsorbent and adsorbate in the process of adsorption or desorption calculation in the GCMC and MD method can be also calculated by the DFT method [111].

After the optimized structures are obtained, the values of the adsorption and desorption energy can be calculated by adopting the DFT model, which can be expressed as [112]

$$E_{\text{adsorption/desorption}} = E_{\text{adsorbates}} + E_{\text{host}} - E_{\text{adsorption/host}} \quad (2)$$

where $E_{\text{adsorption/host}}$ represents the energy of the matrix system or gas system, $E_{\text{adsorbates}}$ denotes the energy of the shale matrix, and E_{host} represents the energy of the gas molecule [113]. When adsorption occurs, the heat of adsorption is exothermic with the positive value of $E_{\text{adsorption/host}}$; otherwise, for negative value of $E_{\text{adsorption/host}}$, desorption occurs, and the heat of adsorption is endothermic with the negative value of $E_{\text{adsorption/host}}$. The adsorption and desorption energy in different shale matrixes and adsorbates has been investigated through calculations using Eq. (2). Researchers have found that shale gas adsorbs more easily in an organic matrix than in an inorganic one [114–116], and the CO₂ adsorption energy is higher than that of CH₄; this illustrates that the CO₂ molecule has a stronger polar adsorption capacity than CH₄ [114], which is also a principle used to produce CH₄ in coal bedded methane by injecting CO₂. The aforementioned phenomena can be further illustrated by the distribution of electron cloud patterns near the adsorption sites of the shale matrix calculated by the DFT method [117]. For example, Liu et al. [118] investigated the distribution of electron cloud patterns of CH₄ in the graphene adsorption site and they found that the interaction between graphene and CH₄ is slightly dependent upon the graphene adsorption sites. This can be further illustrated by the electrostatic charge around the graphenes shown in Fig. 5.

Moreover, Qajar et al. [120] built a dual-site adsorption model to study the adsorption state of the CH₄ molecule in the shale matrix. The surface energy is found to be the crucial factor that influences the shale

gas adsorption capacity, whereas the lateral forces between adsorbed molecules have no effect on such capacity.

Characterization is also essential to understand the shale matrix fully for building a shale matrix structure and predicting the shale gas storage capacities and transport properties of shale gas reservoirs; such characterization includes the distribution of the shale matrix pore size, which is calculated by the DFT method [121,122]. Recently, DFT method is also used to predict the competitive sorption of CO₂ in CO₂/CH₄ gas mixtures in nanoporous shale for enhanced gas recovery [123].

3. Adsorption and desorption amount at the molecular level

3.1. State of the art

The accurate prediction of shale gas adsorption capacity is a prerequisite for evaluating the gas productivity-in-place under different geological conditions, because approximately 20–85% of the total amount of shale gas in a shale reservoir is the adsorbed shale gas, and gas desorption dominates the production in some shale matrixes [124,125]. Therefore, the information of shale gas adsorption on the subsurface shale formations can improve the resource assessment. Furthermore, the amount of desorption is frequently obtained by subtracting the adsorption amount at low pressure from that at high pressure. It is typically assumed that there is no hysteresis in the desorption process. The GCMC model offers a good opportunity to explain the adsorption and desorption mechanism.

3.2. Theory of grand canonical Monte Carlo method and main calculation process

3.2.1. Basic input parameters

The shale matrix structures, shale matrix force field parameters, and adsorbate, which are calculated by the DFT method, can be used as the input parameters in the GCMC method calculation.

The shale matrix structure is fundamental in shale gas storage. The prediction of adsorption amount reported in the literature mainly focuses on inorganic matter, such as clay minerals (montmorillonite, chlorite, kaolinite, and illite), calcite, pyrite, quartz, and organic matter (kerogen). Fig. 6 displays a typical crystal structure of montmorillonite, quartz, calcite, pyrite, and organic matter. It can be observed that the clay minerals have two blocks: one is the tetrahedral silicate sheet with oxygen ion and the other is the octahedral sheet linked to a hydroxyl/aluminum ion. The shale matrix structure is associated with the following: the chemical component for the quartz is SiO₂; calcite is composed of CaCO₃, and pyrite contains FeS₂; the kerogen is mainly composed of carbon, oxygen, nitrogen, and hydrogen with a small amount of sulfur. It can be divided into three types: I, II, III, based on its composition and type of hydrocarbon.

The force field parameters, which describe the contact relation between the adsorbate and adsorbent, and between the adsorbate and

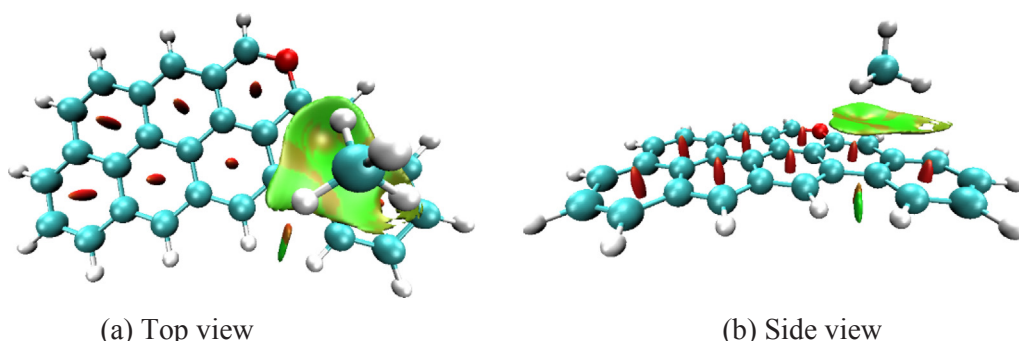


Fig. 5. Color-filled map of graphenes calculated by the DFT method. The interaction between graphene and CH₄ is slightly dependent upon the graphene adsorption sites. Reprinted with permission from Ref. [119].

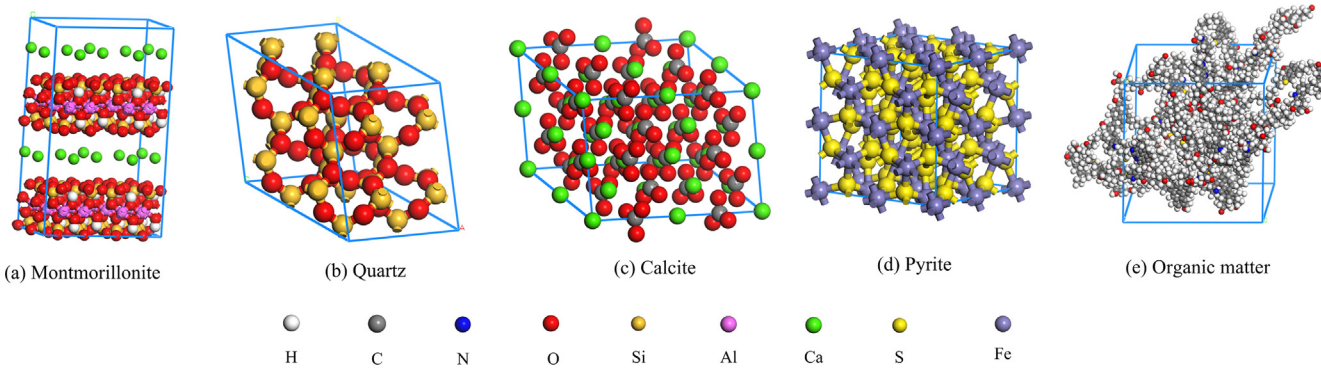


Fig. 6. Main contents in the shale matrix. The shale matrix contains several components.

another adsorbate, can be used as input parameters in the GCMC, MD, and LB methods calculation. In shale gas, the existing CH₄, CO₂, N₂, H₂O, C₂H₆, and C₃H₈ are considered as adsorbates. The parameter details of adsorbates in the force field are found in Ref. [78]. The inorganic and organic matters are regarded as adsorbents. The parameters of the force field adsorbents can only be obtained with a different software, such as COMPASS force parameters in the sorption module of MS (kerogen) [126], CLAYFF force parameters in the sorption module of MS [127] and MUSIC [128] (montmorillonite), CLAYFF force parameters in RASPA package (illite) [129], Dreiding force parameters in the sorption module of MS (kaolinite) [130,131], Dreiding force parameters in the sorption module of MS (quartz) [132] and COMPASS force parameters in the sorption module of MS (calcite) [133].

Accordingly, the force parameters obtained through the software can satisfy various systems, but their accuracy may not be sufficient; in fact, the force parameter values for shale matrix can be obtained through the calculated result from the DFT method. However, no force parameters for the shale matrix calculated by the DFT method has been reported in extant literature.

3.2.2. Grand canonical Monte Carlo calculation method

The adsorption and separation characteristics of shale gas in the shale matrix are calculated by the GCMC simulation method with constant values of the simulation volume (V), chemical potential (μ), and temperature (T) [134]. The aforementioned temperatures and pressures are typically considered the input parameters in the simulation process. The initial configuration (m) has an adsorbate (N_m), and the process of insertion, random movement, and deletion of a shale gas molecule are repeated. The acceptance probabilities for movement ($p_{m \rightarrow n}^*$), insertion ($p_{m \rightarrow n}^{*+}$), and deletion ($p_{m \rightarrow n}^{*-}$) in a new configuration (n) are written as

$$p_{m \rightarrow n}^* = \min\{1, \exp[-\beta(U_n - U_m)]\} \quad (3a)$$

$$p_{m \rightarrow n}^{*+} = \min\left\{1, \frac{\beta f V}{N_n} \exp[-\beta(U_n - U_m - \mu)]\right\} \quad (3b)$$

$$p_{m \rightarrow n}^{*-} = \min\left\{1, \frac{N_m}{\beta f V} \exp[-\beta(U_n - U_m + \mu)]\right\} \quad (3c)$$

where μ is the chemical potential, and f is the fugacity, which should be translated into pressure (p) calculated by the Peng-Robinson equations. The coefficient β is expressed as

$$\beta = \frac{1}{kT} \quad (4)$$

where k is the Boltzmann constant.

The energy of the configuration n and m are U_n and U_m , respectively. U_{ij} contains the electrostatic potential (U_{Eq}) and L-J potential (U_{LJ}). The total potential energy, U_{ij} , is read as

$$U_{ij} = U_{LJ} + U_{Eq} = 4\varepsilon_{ij} \left[\left(\frac{\sigma_{ij}}{r_{ij}} \right)^{12} - \left(\frac{\sigma_{ij}}{r_{ij}} \right)^6 \right] + \frac{q_i q_j}{4\pi \varepsilon_0 r_{ij}} \quad (5)$$

The first term is the interatomic potential described by the L-J model, and the second one is the electrostatic potential energy (or Coulomb component). Where ε_{ij} and σ_{ij} are the L-J depth and diameter of the i and j interacting atoms, respectively, r_{ij} is the distance between the i and j interacting atoms, q_i and q_j are the charge values of the i and j interacting atoms, and ε_0 is the dielectric constant. The Ewald summation technique is adopted during the electrostatic interaction calculation [135]. The cutoff radius of the simulation system is set to the value of over half of the simulation box for all the L-J interactions, and the Lorentz-Berthelot mixing rules are used in the processes of determining all the L-J cross-interaction parameters [136].

Several steps are used for each state point of pressure and temperature to guarantee that the chemical potential between the bulk and adsorbed phase is in equilibrium; the same steps are used to obtain the desired thermodynamic properties. Finally, the total number of shale gas molecules (N_{am}) adsorbed in the shale matrix is obtained. The calculated adsorbate-adsorbate potential energy (U_{ff}) and adsorbate-adsorbent potential energy (U_{fs}) are used to obtain the shale gas adsorption heat. The detailed calculation process is found in Ref. [137].

The number of adsorbate molecules only pertains to the number of shale gas molecules adsorbed in the simulation box; this number of shale gas molecules should be converted to the total adsorption amount (q_{total}) [138]:

$$q_{total} = q_{excess} + \rho V_{free} \quad (6)$$

where ρ is the bulk density and V_{free} is the free volume of a single crystal cell, which is calculated through N₂, Ar, or the CO₂ molecule as the probe [139]. q_{excess} is the excess amount of shale gas adsorption, which can be used to compare with the experimental data directly [140]. The expression of q_{excess} is given by

$$q_{excess} = 1000 \left(\frac{N_{am} M_a}{N_a} - \rho V_{free} N_A \right) / (M_s M_a) \quad (7)$$

where M_s is the substance amount of a single crystal cell for the shale matrix, M_a is the relative molecular mass of the shale gas molecule, N_a is the number of structure cells, and N_A is the Avogadro's constant. The heat of adsorption in the shale matrix, Q , is expressed as follows [141]:

$$Q = RT - \frac{\langle U_{ff} N_{am} \rangle - \langle U_{ff} \rangle \langle N_{am} \rangle}{\langle N_{am}^2 \rangle - \langle N_{am} \rangle \langle N_{am} \rangle} - \frac{\langle U_{fs} N_{am} \rangle - \langle U_{fs} \rangle \langle N_{am} \rangle}{\langle N_{am}^2 \rangle - \langle N_{am} \rangle \langle N_{am} \rangle} \quad (8)$$

where $\langle \rangle$ represents the ensemble average [136].

3.3. Grand canonical Monte Carlo method applied to shale gas adsorption and desorption process

The shale matrix primarily contains inorganic and organic matter

(kerogen). Accordingly, the adsorption and desorption processes in inorganic and organic matrixes are studied. The adsorption amounts of shale gas at different pressures and temperatures in different shale matrixes are presented in Table 2. Although for the shale structure is the same, the predicted amount of adsorbed shale gas can vary. This means that the structure of the shale matrix content has a key influence on the shale matrix adsorption capacity. Different shale matrixes also have different shale gas adsorption capacities. Thus, the transport properties should be investigated deeply.

Montmorillonite is a typical type of clay mineral. The adsorption properties of CH₄ and the CO₂/CH₄ gas mixture in Na-montmorillonite clay have been investigated [156,157]; it has been observed that competitive adsorption between CH₄ and CO₂ exists in Na-montmorillonite clay. The negatively charged clay surface and the interlayer sodium cations enhance the Na-montmorillonite interactions with CO₂ molecules compared with CH₄ molecules [158]. Jin et al. [159] also found that the charges affect the orientation of CO₂ molecules around the montmorillonite surface; they perform a key function in CO₂ adsorption, whereas the CH₄ adsorption capacity has a relationship with the surface area of montmorillonite. Wang et al. [160] investigated the adsorption behavior of the CH₄ / C₂H₆ gas mixture in montmorillonite. They found that the preferential adsorption of C₂H₆ at high pressures is facilitated by simply increasing its mole fraction in the bulk fluid, as shown in Fig. 7.

The moisture reduces the amount of surface sites available for other molecules to be adsorbed, and thus, it plays an important role in the CH₄ adsorption in the shale matrix. Most H₂O is likely to be absorbed on the surface of clay minerals, which are hydrophilic [39]. Water adsorption in clay can lead to clay swelling, which can reduce the pore volume and block the pore throat, thus decreasing and restricting access to the adsorption sites for CH₄ [161,162]. The influence of H₂O on the adsorption behavior of the CH₄/CO₂ gas mixture in varied cation-montmorillonite clays, such as Na, Cs, and Ca, is firstly analyzed. It was demonstrated that the presence of an increasingly pre-adsorbed H₂O component in the interlayer of clay minerals can reduce the amounts of CO₂ and CH₄ adsorption; this illustrates that there also exist competing adsorption sites between the CH₄, CO₂, and H₂O [163]. Thereafter, Wang et al. [164] and Li et al. [165] summarized the factors, such as clay type, structure heterogeneity, clay pore size, H₂O content, pressure, and temperature, that affect CH₄ adsorption and CO₂/CH₄ selectivity. They found that the intermolecular interaction forces and adsorption area perform important functions on CH₄ adsorption, which

is controlled by the chemical composition, physical properties of clay, and crystal structure. They also investigated the influence of shale matrix depth (*i.e.* pressure) on shale gas adsorption [166,167]; it was found that the CO₂/CH₄ selectivity is a function of geological depth (*i.e.* pressure). Furthermore, the optimum operating conditions for shale gas displacement by CO₂ are found in a depth of 1 km with CH₄ partial pressure hydrostatic of 15000 kPa; this information can provide guidance on the displacement of shale gas by injected CO₂ gas to exploit the shale gas reservoir [168].

The adsorption properties of shale gas in other clay types are also examined. For example, Zhang et al. [169] reported that pressure has a large effect on the adsorption capacity properties of CH₄ and C₂H₆ in K-illite clay. At the low pressure, the adsorption capacity of C₂H₆ is stronger than that of CH₄. While with the increasing pressure, CH₄ molecule displays the stronger increasing adsorption behavior than C₂H₆. Chen et al. [115] found that the CH₄ molecules are adsorbed in the ring center, and CO₂ molecules are close to the oxygen atom with polarity in the ring. This illustrates that the electric quadrupole moment strengthens the adsorption capacity of CO₂ compared to that of CH₄ in K-illite pores. A typical CH₄ adsorption in illite is shown in Fig. 8, where it can be observed that the CH₄ molecules are randomly distributed.

Zhang et al. [171] examined sequentially the influence of the pore sizes 0.72, 2.88, and 11.52 nm on CH₄ adsorption in kaolinite. They discovered that the absolute adsorption amount of CH₄ decreases exponentially with the increase in pore size; eventually, a constant value is reached when the pore size ranges 6–8 nm. The adsorption behaviors of the CH₄/CO₂ gas mixture in quartz nanopores show that a tight adsorption molecule layer of CH₄ gas of 0.3–0.5 nm exists; the CO₂ molecules are preferentially adsorbed on the nanopore compared to those of CH₄ because of a stronger interaction between the CO₂ molecules and hydrophilic groups on the pore surface [172]. Subsequently, Xiong et al. [146] investigated the effects of H₂O content on CH₄ adsorption in quartz. It was noted that the relationships between CH₄ and H₂O molecules in the quartz pores are not adsorption site competitive but adsorption space competitive; this indicates that the H₂O molecule can occupy the adsorption space of the CH₄ molecule. Images of CH₄ adsorption on quartz at different pressures are shown in Fig. 9.

The accurate prediction of the adsorption and desorption behaviors of shale gas in the shale matrix is crucial to understand the fundamental mechanisms that can govern the shale gas condensate, transport, storage or recovery in shale reservoirs [116]. Kerogen, which has no accurate molecular formula, is an intricate amorphous hydrocarbon

Table 2
Adsorption amount of shale gas in different shale matrixes.

Shale matrix	Adsorption amount	Pressure (kPa)	Temperature (K)	Refs.
Montmorillonite (Ca)	0–0.31 mmol·g ⁻¹	0–9000	308	[142]
Montmorillonite (Ca)	0–2.09 mmol·cm ⁻³	0–45000	353	[143]
Montmorillonite (Na)	0–3.54 mmol·g ⁻¹	0–20000	323	[144]
Montmorillonite (Na)	0–2.00 mmol·g ⁻¹	0–50000	363	[127]
Montmorillonite (Na)	0.08 cm ³ ·m ⁻²	0–50000	333	[145]
Kaolinite	0–0.06 cm ³ ·m ⁻²	0–50000	333	[145]
calcite	0–2.28 mmol·cm ⁻³	0–45000	353	[143]
slit-like quartz	0.26–4.84 mmol·cm ⁻³	2000–40000	333.15	[146]
Multilayer graphene slit	2.61–7.36 mmol·cm ⁻³	1250–20000	333.15	[147]
K-illite	0–0.04 cm ³ ·m ⁻²	0–50000	333	[115]
Illite	0–0.04 cm ³ ·m ⁻²	0–50000	333	[145]
Illite	0–15.1 mmol·g ⁻¹	0–50000	298	[148]
Nanoporous kerogen	0–3.86 mmol·g ⁻¹	0–20000	300	[149]
graphene	0–16 kg·m ⁻³	0–40000	300	[150]
graphene	0–2.5 mmol·cm ⁻³	0–45000	353	[143]
Kerogen	0–0.12 cm ³ ·m ⁻²	0–50000	333	[145]
Functional group rich organic shale	0–10 mmol·m ⁻³	0–14000	373	[151]
Kerogen slit	0–8.55 mmol·g ⁻¹	0–20000	298.15	[114]
Kerogen-Type II	0–3.8 mmol·g ⁻¹	0–20000	298.15	[152]
Kerogen-Type II	0–2.5 mmol·g ⁻¹	0–25000	298.15	[153]
Kerogen	0–1.64 mmol·g ⁻¹	0–16000	338	[154]
kerogen	0–3.6 mmol·g ⁻¹	0–25000	338	[155]

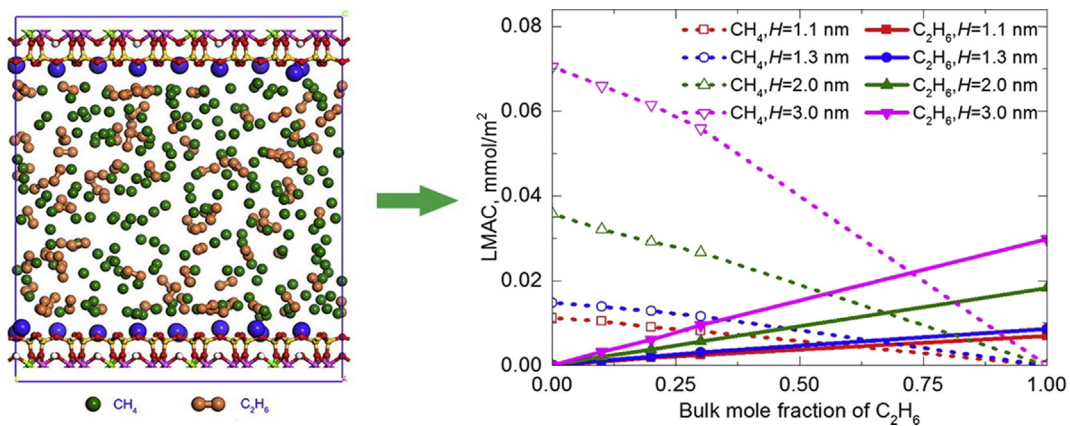


Fig. 7. Adsorption site of CH_4 and C_2H_6 captured by the GCMC method; competition between CH_4 and C_2H_6 exists in the shale matrix. Reprinted with permission from Ref. [160].

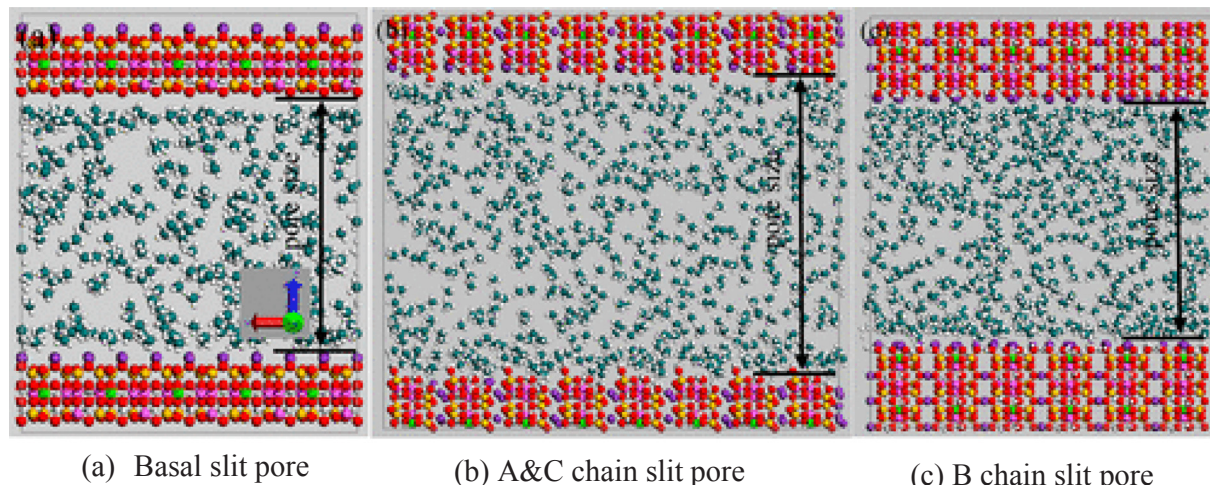


Fig. 8. Illite with adsorbed CH_4 molecules in different pore structures. The CH_4 molecules are randomly distributed in all three kinds of illites. Reprinted with permission from Ref. [170].

macromolecule. Kerogen mainly consists of hydrogen, carbon, nitrogen, oxygen, and small amounts of sulfur. The real structure of kerogen is difficult to determine because it depends on the deposition surroundings and the nature of the organic matter [173,174]. Although the different chemical structure models for kerogen in different conditions reflect its local structural characteristics, they cannot obtain the kerogen's chemical and physical characteristics; consequently, these models are not widely adopted [175,176]. Guan et al. [104] and Bousige et al. [177] proposed a mature kerogen through the hybrid experimental method. However, it just can provide a nanostructure picture of

kerogen without considering the clays and other minerals. Several different types of organic matter have been reported in the literature [104,177], and details of their various models have been developed, as shown in Fig. 10. It can be noted that the accuracy of the organic matter structure remains a problem in the prediction of shale matrix properties.

Previously, the simplified two-dimensional carbon slit [183] or graphene [150] was regarded as a kerogen structure. Wang et al. [184] treated the carbon slit nanopores as the kerogen structure to describe the micro-structure of organic materials. They discovered that pores

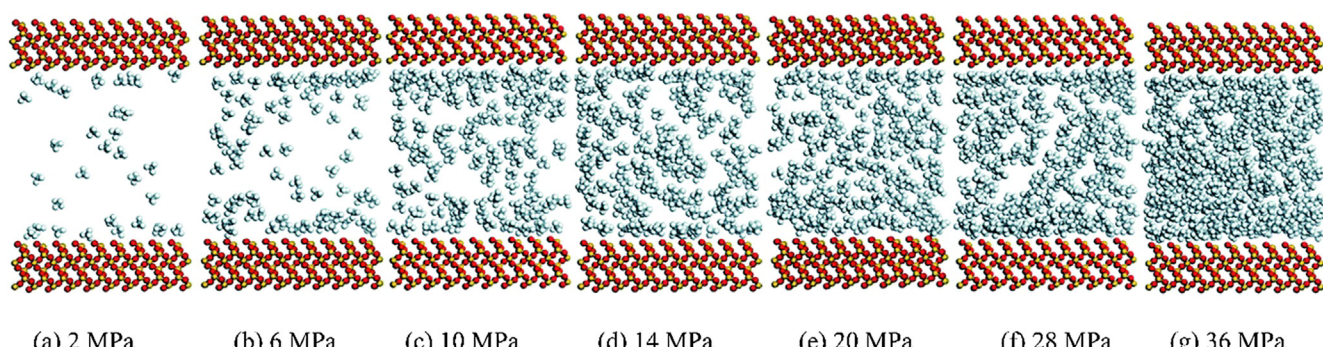


Fig. 9. Images of CH_4 molecules on quartz with pore of 4 nm under various pressures at 333 K; the CH_4 adsorption amount increases with an increase in pressure. Reprinted with permission from Ref. [146].

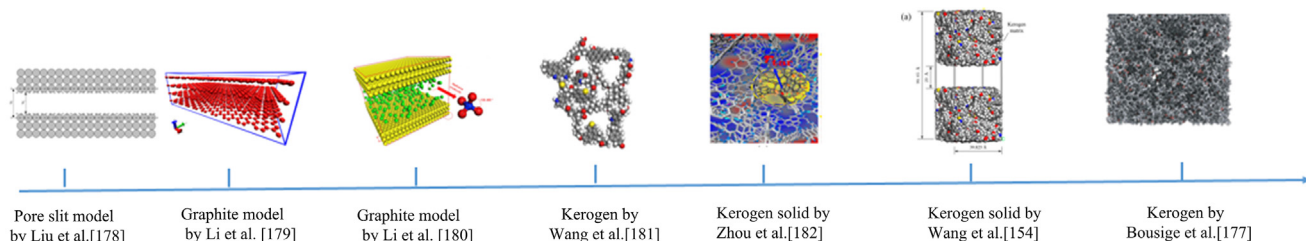


Fig. 10. Structure models of organic matrix. Reprinted with permission from Ref. [154,177–182].

with sizes ranging from 1 to 50 nm are the dominant adsorption sites in the shale reservoir. Sequentially, Liu et al. [178] discovered that the excess adsorption amount exhibits a stepped increase with an increase in pore size when the pore sizes ranging from 0.5 to 1.5 nm. However, once the value of the kerogen pore size is over 1.5 nm, the excess amount of shale gas adsorption keeps unchanged despite the increase in pore size; typically, this is caused by the specific surface area. Subsequently, He et al. [185] characterized the CH_4 transport in graphite layers (treated as kerogen) with high roughness. They found that the mass flux of the CH_4 gas has a linear relationship with the shale gas pressure gradient in the shale gas reservoir.

Although the laws in carbon slit and graphite can reflect the rules in kerogen, the structure of the real kerogen is different from those of carbon slit and graphite. Thus, the shale gas transport mechanism is different in the corresponding structure. Xiong et al. [176] studied the adsorption properties of the CH_4 gas in organic matrix. They discovered that most of CH_4 molecules are in a free state under a high pressure once the pore size is over 6 nm under different types of pores. The CH_4 adsorption capacity in the different types of pores decreases according to the following: organic matrix pore > inorganic matrix pore. This means that both the comprehensive effects of the distribution density and differential adsorption capacities of the adsorption sites in the organic and inorganic matter determine the shale gas adsorption capacity [145,186].

Wang et al. [181] studied the separation properties of the CO_2/CH_4 gas mixture in kerogen and found that the CO_2 molecule is adsorbed around a low energy absorption site when it is compared to that of CH_4 ; this indicates that the adsorption capacity of the CO_2 molecules in kerogen is stronger than that of CH_4 . The selectivity of the CO_2/CH_4 gas mixture first decreases with an increase in pressure until it reaches a critical pressure; thereafter, it remains approximately 3.8 as the pressure continues to rise. Some researchers consider that kerogen is hydrophobic, thus, adsorption of water molecule in the kerogen is limited. Therefore, as the total organic content (TOC) increases, an increase in CH_4 sorption capacity and decrease in moisture content were observed [36,161]. However, Huang et al. [126] investigated the adsorption properties of the CH_4/CO_2 gas mixture in moist kerogen. The results show that the H_2O molecule is preferentially adsorbed in the sulfur-and oxygen-containing groups at low moisture. The moisture has a considerable influence on the CO_2 adsorption compared to that of CH_4 . These different conclusions result from the different types of kerogen structure they use.

Apart from the function of the adsorbate (shale gas) on shale gas adsorption, the adsorbent (kerogen) structure also has a strong influence on shale gas adsorption and selectivity [187]. For example, Michalec et al. [188] focused on the adsorption properties of two shale gas proxies (CH_4 and $\text{CH}_4/\text{C}_2\text{H}_6/\text{C}_3\text{H}_8$ (82:12:6)) in type II kerogen. It was noted the preferential adsorption of C_3H_8 and to a lesser extent of C_2H_6 on both mesopores and micropores of the shale structures. Subsequently, Song et al. [189] found that the influence of the kerogen type on the adsorption capacity is ordered as follows: type III > type II > type I, which means that it is easier for the CH_4 molecules to be adsorbed on type III kerogen. The structure of kerogen is usually treated as rigid during the simulation. Recently, Wu et al. [190] treated the

structure of kerogen as a flexible one. They found that the shale gas adsorption amount in the flexible kerogen is higher compared to that in the rigid one. This means that the structure of the real kerogen is flexible. However, studies on flexible kerogen are rarely reported.

4. Shale gas diffusion at the molecular level

4.1. General knowledge

The shale gas desorbs from the organic/inorganic surfaces, and thereafter the desorbed shale gas molecules diffuse; slippage flow in the micropores along with viscous flow in the natural fractures will occur. Thus, the diffusion properties of shale gas in the shale matrix have a key function in predicting shale gas production. The MD can be considered capable of acquiring dynamic properties such as transport behavior and diffusion coefficient.

4.2. Theory of molecular dynamic method and calculation process

Shale gas diffusion in the crystal of the shale matrix is referred to as self-diffusion owing to the small size of the chosen shale matrix cell; diffusion is the result of random Brownian motion of shale gas molecule in the shale matrix, which can be calculated by the MD method.

The MD method is based on solving the Newton's equations of shale gas motion for a shale matrix adsorption system [144]. The potential energy of the interaction between the shale gas molecule and shale matrix, and between the shale gas molecules can be described by the force fields of molecular adsorption mechanics, whose values can be obtained from the DFT method. The MD is usually solved by using the integration through propagation and iteration. Therefore, the leapfrog and Verlet algorithms are adopted during the processes of solving the Newton's equations [191]. Recently, the Gear predictor-corrector, and Runge-Kutta algorithms are also used to increase the stability of the MD method. During the process of MD method simulation, the values of volume, temperature, and the number of adsorbed molecules are imposed to be constant. Thus, the MD method simulated system is also called the *NVT* ensemble or canonical ensemble. In fact, temperature usually has a relationship with the momenta of the shale matrix system, and the total energy of the shale gas adsorption system should be altered through the Nose-Hoover thermostat method [192]. The MD is suited to investigate the dynamics of transport phenomena or non-equilibrium structure, such as shale gas diffusion in the shale matrix. Therefore, the transport behavior and diffusion coefficients can be calculated using MD [193].

For complicated shale gas diffusion systems, the momentum (\mathbf{p}) and position (\mathbf{q}) coordinates of the shale gas molecule are written as

$$\mathbf{p}(t + \Delta t) = \mathbf{p}(t) + m\mathbf{a}(t)\Delta t \quad (9)$$

$$\mathbf{q}(t + \Delta t) = \mathbf{q}(t) + \frac{\mathbf{p}(t)}{m}\Delta t \quad (10)$$

where $\mathbf{a}(t)$ is the acceleration, and m is the mass of the shale gas molecule. The initial coordinates can be chosen randomly. The correlation between initial momentum and temperature for each shale gas

molecule is expressed as

$$T(t) = \frac{1}{(3N - n)k_B} \sum_{i=1}^N \frac{|\mathbf{p}_i(t)|^2}{m_i} \quad (11)$$

where n is the total number of constrained degrees for shale gas freedom, N is the total number of shale gas molecules, and m_i is the mass of shale gas molecule. The equilibrium physical property for the shale gas adsorption system can be written as

$$A = \iint A(\mathbf{q}, \mathbf{p}) P(\mathbf{q}, \mathbf{p}) d\mathbf{q} d\mathbf{p} \quad (12)$$

where $A(\mathbf{q}, \mathbf{p})$ is the physical property for a shale gas molecule at equilibrium, $P(\mathbf{q}, \mathbf{p})$ is the probability for a particular atom arrangement in a molecule, which agrees with the Boltzmann distribution; this probability is expressed as

$$P(\mathbf{q}, \mathbf{p}) \propto \exp\left[-\frac{E(\mathbf{q}, \mathbf{p})}{kT}\right] \quad (13)$$

where $E(\mathbf{q}, \mathbf{p})$ is the total energy, which includes both potential and kinetic energy values.

Einstein approach is adopted during the shale gas diffusion simulation in the MD method. Then, the slope of the mean squared displacement over a long period should be calculated to estimate the diffusivity. The shale gas self-diffusion, D_s , can be written as

$$D_s = \frac{1}{2dN} \lim_{t \rightarrow \infty} \left\langle \sum_{i=1}^N |\mathbf{r}_i(t) - \mathbf{r}_i(0)|^2 \right\rangle \quad (14)$$

where $\mathbf{r}_i(t)$ is the position of the center of mass of the shale gas molecule i at any time of t , and d is the shale matrix spatial dimension (3 for shale gas). In general, the three foregoing diffusivities are treated as the same value, except in case of the vanishing concentration of shale matrix.

To describe the diffusion behaviors of shale gas mixtures in the shale matrix, there are several formalisms. Every element Δ_{ij} of the shale matrix can be calculated from the MD method simulation by

$$\Delta_{ij} = \frac{1}{2dN_j} \lim_{t \rightarrow \infty} \left\langle \sum_{l=1}^{N_i} \left| \mathbf{r}_l^i(t) - \mathbf{r}_l^i(0) \right| \sum_{k=1}^{N_j} |\mathbf{r}_k^j(t) - \mathbf{r}_k^j(0)| \right\rangle \quad (15)$$

where N_i and N_j are the number of shale gas molecules of components i and j , respectively, and $\mathbf{r}_l^i(t)$ is the shale gas molecule position of component i at any time t .

4.3. Molecular dynamic method applied to shale gas diffusion

The initial shale matrix crystal configuration with adsorbed shale gas is a dominant factor for predicting the shale gas diffusion accurately. Two approaches exist to obtain the shale diffusion in the shale matrix: one involves assuming the quantity of adsorbed shale gas molecules in the shale matrix (usually over the real saturation amount of shale gas adsorption); another way is using the equilibrium configuration calculated by the GCMC method as the initial input configuration for further simulation with the MD method. The second method is widely reported in the literature.

The condition of gas diffusion in the inorganic shale matrix is first reported. The effects of content, cation, geometric structure, and external factors, namely, pressure and temperature, on the shale gas diffusion are summarized. Sun et al. [194] studied the diffusion behaviors of CH_4 and CO_2 in montmorillonite and it was noted that the diffusion coefficients for CH_4 and CO_2 both decrease with an increase in pressure; moreover, CO_2 has a relatively weaker value of the diffusion coefficient compared to that of CH_4 . This means that CO_2 is easier to be adsorbed in the shale matrix crystal compared to that of CH_4 . The transport properties of the CO_2/CH_4 gas mixture in Na-montmorillonite clay in the presence of water are also investigated [195]. It has been discovered that the diffusion coefficients of the CO_2 and CH_4 molecules in

the Na-montmorillonite decrease with an increase in their loads due to the steric hindrance. The diffusion coefficient of CO_2 gas with a constant loading amount of CO_2 molecules is not significantly affected by the CH_4 molecule. Wang et al. [196] found that the diffusion coefficients of shale gas keep an extremely small value within 2.8 nm basal spacing, and then it can increase by several order of magnitude when continuing to increase the basal spacing. This illustrates that the shale gas diffusion coefficient has gone through the microscopic pore into the mesoscopic pore. Sharama et al. [197] investigated the structural and dynamic properties of the CH_4 gas in montmorillonite slits with 1.0, 2.0, and 3.0 nm pore sizes; they observed that diffusion across models is anisotropic, which indicates that the limiting pore region crossing is the main factor on the controlling step of the shale gas transport process.

The diffusion properties of shale gas in other clay types are also considered. Hao et al. [169] studied the adsorption behavior of CH_4 confined in a nanoscale illite slit pore considering the basal and edge surfaces; they discovered that basal surfaces have stronger van der Waals interactions compared to those in edge surfaces when the value of adsorption thickness is only 0.9 nm. Wang et al. [198] simulated the diffusion behavior of supercritical CH_4 in calcite; they reported that the adsorbed CH_4 molecules in the confined space diffuse rapidly with the increase in pore size and temperature, but they diffuse slowly with an increase in pressure. Sun et al. [133] studied the diffusion behaviors of CH_4 and CO_2 in calcite with a pore size of ~2.2 nm. They noted that CO_2 molecules have a higher capacity in calcite compared to that of CH_4 . The diffusion value of CO_2 molecules is significantly lower than that of CH_4 molecules; this is due to diverse interactions between the calcite surfaces and CO_2 gas molecules. Zhang et al. [199] studied the CH_4 adsorption properties in kaolinite, and its loading effect on kaolinite swelling at different pressures and temperatures. They observed that the diffusion value of shale gas in the shale matrix also decreases with an increase in pressure [142].

Regarding shale gas diffusion in kerogen, graphene is firstly treated as kerogen to investigate the shale gas diffusion condition in the organic matrix [200]; this is done because the structure of kerogen is difficult to be determined [201]. Vasileiadis et al. [153] investigated the diffusion properties of CH_4 , CO_2 , and C_2H_6 in the kerogen region; the temperature and pressure effects, maximum pore diameter, limiting pore diameter, accessible surface, and accessible volume on the diffusion properties in the shale matrix are considered. It was noted that the confined pore region is the key factor to determine the step of the diffusion process. Chen et al. [202] adopted the GCMC method combining the MD method simulations to explore the molecular mechanisms of the adsorption and desorption hysteresis; the influences of temperature, surface strength, and pore width on the hysteresis loop are considered. They observed that when the temperature is over a threshold, the hysteresis disappears, indicating that capillary condensation cannot be applied in the hysteresis of shale gas under the normal temperature condition. Thus, a certain amount of energy is required for CH_4 to pass through the throat because of repulsive interactions existing between shale gas and shale matrix.

4.4. Molecular dynamic method applied to shale gas flow

Shale gas flow in the shale matrix is produced after the desorbed shale gas molecules meet in the shale fracture. The shale gas flow in the shale matrix can also be described by the MD method and Darcy's laws.

The recovery of CH_4 from the shale matrix is a key factor that affects shale gas production. Other gases (more strongly adsorbed by the shale matrix compared to CH_4) are injected into the fracture of the shale matrix to recover the CH_4 gas. Thereafter, the CH_4 gas desorbs from the shale matrix; frequently, CO_2 or H_2O is used to drive the CH_4 desorption in the reservoir [203,204]. The CO_2 injection into the shale matrix is thoroughly investigated [205,206]. It was noted that the shale gas desorption when CO_2 is injected is higher compared to that without CO_2 injection. Moreover, the energy barrier, which is required for displacing

CH_4 by CO_2 injection, just depends on the displacement angle. When the CO_2 molecule reaches the shale matrix surface vertically, the displacement of the CH_4 molecule by a CO_2 molecule occurs very easily. The effects of curvature and size of the carbon nanopore (treated as kerogen) on CH_4 recovery are also identified; it is indicated that an optimum pore size exists, which makes the displacement occur most efficiently, as shown in Fig. 11.

Wu et al. [207] indicated that velocity oscillation will exist along the nanochannel cross-section, and whether the total mass flow can be either enhanced or not just depends on the adsorption conditions under the different nano-channels, which are composed of illite and graphene. Kazemi et al. [208] noted that the nano channel lengths have an obvious impact on gas transport through them. This is because the force field of the wall in the nano-scale confinement and on the shale surface are significant [209,210]. Liu et al. [211] investigated the mass flow of CH_4 and H_2O in the nanopores of slit-shaped silica with the hydrophilic surfaces. They discovered that the sandwich structure of H_2O film- CH_4 - H_2O film and the sandwich structure of the CH_4 gas bubble, which is wrapped in the H_2O bridge, exist in the nanopore because of H_2O wetting the surfaces, as shown in Fig. 12. However, Lee et al. [212] reported that recovery can be reduced by interfacial effects when gas is stored in a wet kerogen surface; this indicates that the knowledge on the effect of H_2O on CH_4 recovery in the shale matrix is still vague.

5. Shale gas flow at pore level

5.1. General knowledge

Unlike conventional hydrocarbon reservoirs, abundant microscale and nanoscale pores with irregular geometric structures coexist in the shale reservoirs. The conventional continuum theory is not valid in this region, and the microscopic effects are significant. The Knudsen number (Kn), defined as the ratio of the mean free path of the shale gas molecule to the shale matrix characteristic length, is usually adopted to reflect the extent of microscopic effects. According to the magnitude of Kn , the gas flow regimes are classified as follows: continuum flow ($Kn < 0.001$), slip flow ($0.001 < Kn < 0.1$), transition flow ($0.1 < Kn < 10$), and free molecular flow ($Kn > 10$) [213]. Pores in the shale are $< 2 \mu\text{m}$, and pores in kerogen are considerably smaller with sizes ranging from 2 to 50 nm; this leads to slippage ($0.001 < Kn < 0.1$) and early transition flow regimes ($0.1 < Kn < 1$) in the shale formation. Furthermore, the adsorbed gas on the pore surface of the nanoporous organic matter is rich, which affects the free gas flow in the middle of the pore space [214]. At this scale, in addition to the viscous flow, it involves desorption/adsorption and surface diffusion, which can be described as particles of the adsorbed phase jumping between adjacent adsorption sites on the solid surface and Knudsen diffusion. The details are shown in Fig. 13.

To accurately describe these transport mechanisms, a powerful tool

is required. The LBM, benefitting from its nature, which is aligned with the gas kinetic theory, is regarded as a powerful approach to investigate the gas flow and transport in the shale matrix at the pore scale [216–218]. The pore level simulation conducted by the LBM not only captures the gas microscopic flow mechanisms but also predicts the macroscopic flow capability, such as the apparent permeability and effective diffusivity [219]. The DFT, GCMC and MD methods are difficult to extend to a relatively larger pore scale and the applications of which are restricted by their high computational costs. More commonly, the GCMC and MD results, such as the adsorbed amount, adsorbed heat, and diffusion coefficient, are adopted as the input parameters of the LBM simulation. The fundamental theory of the LBM and its applications in shale gas flow at the pore level are elaborated in the following sections.

5.2. Theory of Lattice Boltzmann method

As a mesoscopic method, the LBM bridges the microscopic and macroscopic methods. It has become a promising numerical method for simulating the fluid flow and transport phenomena in the shale matrix at the pore scale; in particular, it has been successfully applied under the conditions involving interfacial dynamics and complex boundaries [220–223]. The LBM constructs a simplified kinetic model, in which the essential physics of microscopic or mesoscopic processes are involved, and the averaged macroscopic properties should obey the targeted macroscopic equations. The advantages of the LBM result from its clear physical pictures, and easy treating of boundary conditions, along with the fully parallel algorithms [201,224–226].

The basal lattice Boltzmann (LB) equation is written as

$$f_i(x + c_i \delta_t, t + \delta_t) - f_i(x, t) = \Omega_i(f(x, t)) + \delta_t F_i \quad (16)$$

where f_i is the particle velocity distribution function, $\Omega_i(f(x, t))$ is the collision operator including the single relaxation time (SRT) and multiple relaxation time (MRT) schemes, and F_i is the forcing term [227]. For the SRT scheme, $\Omega_i(f(x, t))$ is expressed as

$$\Omega_i(f(x, t)) = -\frac{1}{\tau} [f_i(x, t) - f_i^{\text{eq}}(x, t)] \quad (17)$$

where τ is the relaxation time that relies on the fluid kinematic viscosity, and $f_i^{\text{eq}}(x, t)$ is the equilibrium distribution function. Detailed information on the LBM theory is found in Ref. [228]. For applying the LBM to simulate a discontinuous shale, two important problems should be addressed. First, in microscale gas flows, the gas dynamic viscosity μ is affected by the local Kn . Because in the LBM, μ is related to the relaxation time τ , the relationship between the relaxation time in the LBM and Kn should be derived, and different models have been proposed in the literature, such as those of Nie et al. [229], Tang et al. [230], and Zhang et al. [231]. The gas mean free path (MFP) in the Knudsen layer (a layer near the wall with non-equilibrium phenomena and a nonlinear

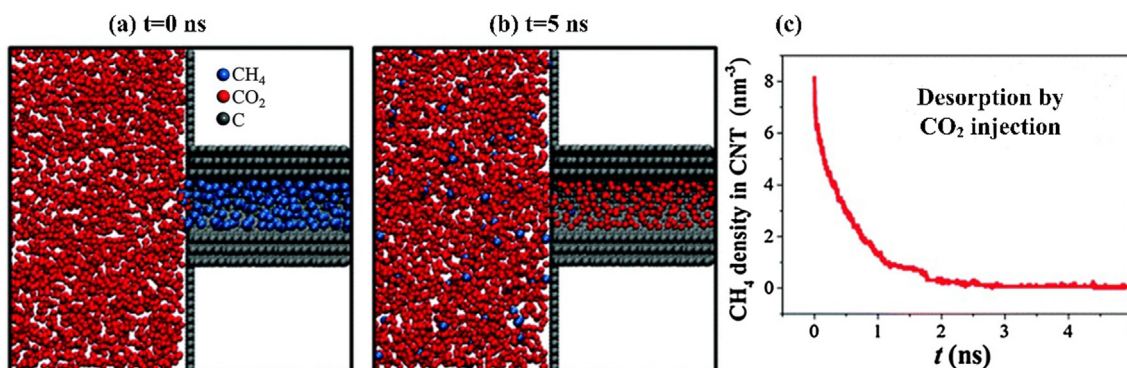


Fig. 11. (a) Desorption by CO_2 injection at 0 ns, (b) Desorption by CO_2 injection at 5 ns, and (c) Evolution of CH_4 density during the desorption process by CO_2 injection at different times. Reprinted with permission from a modified version of Ref. [205].

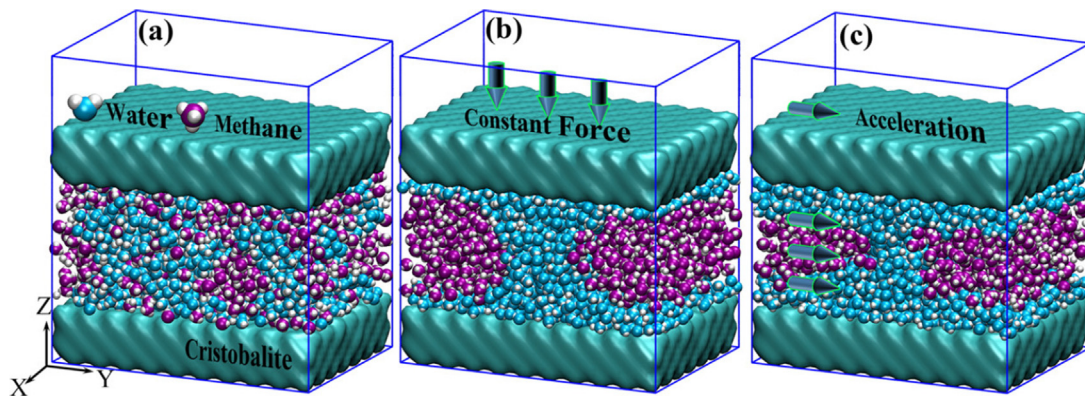


Fig. 12. Schematic of adsorption configuration model. (a) Initial adsorption configuration, (b) Pressure control adsorption configuration, and (c) Flow adsorption configuration. Reprinted with permission of Ref. [211].

stress-strain relationship, typical with thickness of a few MFPs) is smaller than that in unbounded systems owing to more frequent gas molecule-solid wall collisions. Based on the kinetic theory of gas, viscosity can be interpreted in terms of molecule collisions and of the MFP. Therefore, the wall effects on the MFP, and thus on Kn , μ or relaxation time τ , should be considered, and wall-distance scaling functions have been proposed to correct the MFP in the Knudsen layer [232–234]. Second, accurate and efficient LB slip boundary conditions (BCs) should be developed to mimic the slippage on the solid walls. Currently, two models are widely adopted to describe the slip velocity. The first model is the Maxwell slip model [235], in which the slip velocity is a function of Kn , the velocity gradient, and accommodation coefficient. Later, the original first-order model is extended to a second-order or even higher-order model for higher Kn flow [236]. The second model is the Langmuir slip model, where the slip velocity is caused by the time lag between adsorption and latter desorption of gas molecules [237,238]. Tremendous efforts have been devoted in the literature to develop the LB slip BC related to the above two slip models. For the Maxwell-type slip model, a model is developed by combining the non-slip bounce-back and free-slip specular-reflection (CBBSR) BCs [239]; Tang et al. [230] proposed a combined specular-reflection and diffusive-reflection (CSRDR) BC. Discrete effects exist for the above two BCs [240], which can be eliminated using the multi-relaxation-time (MRT) LB model [241]. For the Langmuir slip model, Chen et al. [242] implemented it using the non-equilibrium extrapolation scheme. Detailed discussions of the slip models and corresponding LB models are beyond the scope of the present study, and one can refer to recent review papers [243,244].

5.3. Lattice Boltzmann method applied to shale gas flow at the pore level

To accurately describe the complex transport mechanisms of shale gas, a series of LB models have been established. In the following sections, they are described from the simple to the complex. The main four steps for the investigation of the shale gas transport at the pore level are

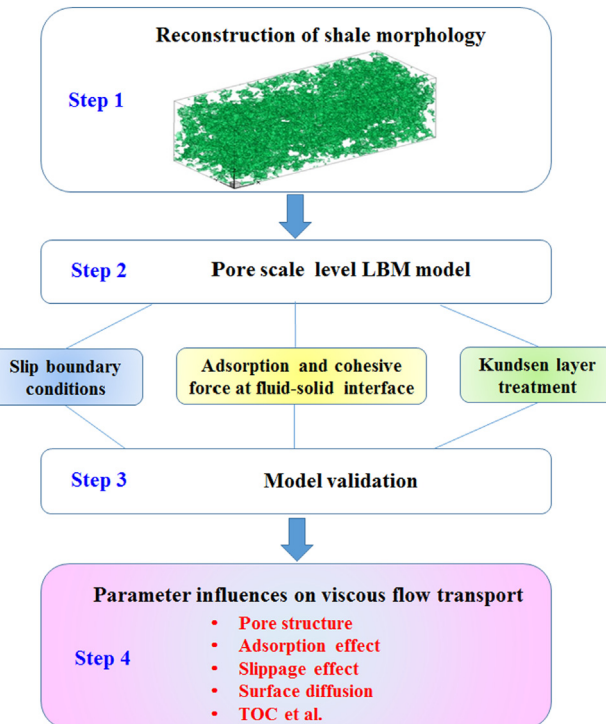


Fig. 14. Steps for investigation of shale gas transport at the pore level.

shown in Fig. 14.

5.3.1. Viscous flow with the slippage effect

The gas flow in the shale matrix is treated as a viscous flow driven by the reservoir pressure gradient at an early shale gas production stage. Owing to the numerous micrometer and nanometer pores in the

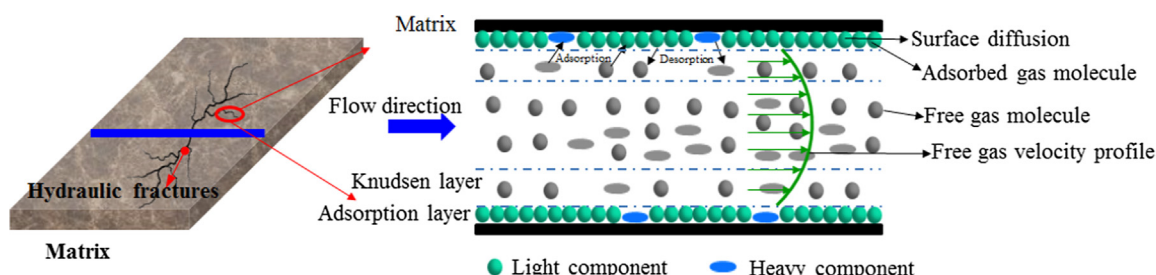


Fig. 13. Schematic of shale gas flow in kerogen pore, which includes surface diffusion and free gas molecule flow. Reprinted with permission from a modified version of Ref. [215].

shale formation, velocity slippage occurs close to the solid wall; this increases the transport capability of shale gas. The enhanced transport capability is described by the apparent permeability that is related to the pore structural features and the pressure and temperature of the shale reservoirs; these distinguish it from the concept of intrinsic permeability, which is a material-specific parameter.

There are two ways to simulate the shale gas microscale flow and predict the apparent permeability through the LBM. One is to modify the conventional LBM, in which the effective relaxation time and slippage boundary condition are used to consider the gas slippage effect; it is known as the microscopic LBM [90]. Along with the pore-scale simulation, the microscopic LBM belongs to a direct simulation method. More importantly, the apparent permeability of the shale matrix can be directly obtained because of LBM's competency in accurately capturing the slip velocity on the pore surface. The other approach is to combine the conventional LBM with other models, such as the Langmuir-slip-boundary condition, Darcy flow, slippage and surface transport [245], the dusty gas model (DGM), which is simply called DGM-LBM. The pure DGM equation for species i in a multicomponent system with local uniform total pressure is as follows

$$-\frac{1}{RT} \nabla p_i = \sum_{j \neq i} \frac{x_j J_i^D - x_i J_j^D}{D_{i,j}} + \frac{J_{i,kn}}{D_{i,kn}} \quad (18)$$

where p_i is pressure, x_i and x_j are the mole fraction of species i and j , respectively, J_i^D is the diffusion flux, $D_{i,j}$ is the binary diffusivity of species i and j , and $D_{i,kn}$ is the Knudsen diffusivity of species i . Multiple components exist in the shale reservoirs such as CH_4 , C_2H_6 and H_2O . However, CH_4 usually dominates with a volume fraction higher than 90% [21], and a single component can be assumed for which Eq. (18) is reduced to Eq. (19).

$$J_{kn} = -MD_{kn}(\nabla C) = -MD_{kn} \nabla \left(\frac{p}{zRT} \right) = -\frac{\rho}{p} D_{kn} \nabla p \quad (19)$$

where C is the gas concentration, M is the relative molecular mass, z is the compressibility factor, and D_{kn} is the Knudsen diffusivity. Knudsen demonstrated that the total flux for a single component system can be described as the sum of the viscous flow flux and Knudsen diffusion flux, as follows [246]

$$J_t = J_{vis} + J_{kn} \quad (20)$$

The first part of the Knudsen diffusion is called "viscous slip" or "slip" [247], which accounts for the slip effect. Darcy's law is typically used as follows:

$$J_{vis} = -\frac{\rho k_{\infty}}{\mu} \nabla p \quad (21)$$

Substituting Eq. (20) and Eq. (18) (the single component version of Eq. (19)) into Eq. (21), the total flux is determined as follows:

$$J = -k_{\infty} \left(1 + \frac{D_{kn}\mu}{pk_{\infty}} \right) \frac{\rho}{\mu} \nabla p \quad (22)$$

where μ is the dynamic viscosity. A correlation for apparent permeability based on Eq. (22) can be obtained, and it is easy to find that the Knudsen diffusivity is related to b_k [248]

$$k_a = k_{\infty} \left(1 + \frac{D_{kn}\mu}{pk_{\infty}} \right), D_{kn} = \frac{k_{\infty} b_k}{\mu} \approx \frac{4k_{\infty} \lambda}{\mu r}, b_k = \frac{4\lambda}{r} \quad (23)$$

where r is the radius. Based Eq. (23), the Knudsen diffusivity is estimated using a certain definition of MFP and empirical equations for the pore size of a porous medium [249]. For example, based on the definition of gas mean free path (λ) from kinetic theory [250], the following may be derived:

$$\lambda = \frac{\mu}{p} \sqrt{\frac{\pi RT}{2M}} \quad (24)$$

Freeman et al. [251] obtained the following expression for D_{kn} :

$$D_{kn} = \frac{4k_{\infty}}{2.81708 \sqrt{\frac{k_{\infty}}{\phi}}} \sqrt{\frac{\pi RT}{2M}} \quad (25)$$

where ϕ is the porosity. The DGM-LBM regards the total gas mass flow flux as the superposition of a viscous flow flux and the Knudsen diffusion flux. The intrinsic permeability in the viscous flow flux term is calculated through the conventional LBM with the no-slip boundary. Thereafter, a slip correction factor derived from the Knudsen diffusion flux term is adopted to correct the intrinsic permeability and consider the gas slippage effect. The corrected intrinsic permeability is the apparent permeability.

The modified conventional LBM, compared with the conventional LBM combining with the other models mentioned above, is more popular because it is established on the nature of slippage effect, and it can describe the slippage and high Knudsen flow behavior in arbitrarily complex pore structures [252]. However, the major problem with this approach is the necessity to set the appropriate relaxation time and slippage boundary condition on irregular porous structures. To resolve this difficult issue, considerable work has been conducted on pore structures that range from simple to complex.

Microscale and nanoscale capillaries are the simplest pore structures. These are widely used to estimate the shale gas flow behavior in shale strata because of the ease they offer for handling the regular slippage boundary condition. As a pioneer, Fathi et al. [253] adopted the microscopic single relation time -LBM (SRT-LBM) to simulate shale gas flow in the nanoscale capillary. They found that the predicted apparent permeability is higher than that given by the Klinkenberg slip theory because the gas molecules not only interact with the solid surface but also with the bulk fluid. They defined this phenomenon as the double-slip effect and further proposed a modified Klinkenberg slip equation. Subsequently, based on a similar simulation model, Zhang et al. [216] investigated the shale gas slippage flow characteristics in a single organic nanopore and concluded that the influence of the slippage boundary conditions on the gas velocity profiles and slippage effect is remarkable. Simple as the capillary model may be, it is illuminating, and it facilitates the further application of microscopic LBM in shale gas production.

The shale matrix is comprised of porous structures; consequently, it is difficult to reflect the shale gas practical flow behaviors in the reservoirs through the capillary model. In view of this, a sudden and gradual contraction of microscale channels is built to partially involve the effect of pore structure. Accordingly, a series of variable cross-section channels is constructed to study the shale gas flow behaviors by using an MRT-LBM. Thereafter, the effects of cross-section shrinking coefficient and Knudsen number on shale gas transport are identified. They found that the shale gas apparent permeability can be underestimated when the influence of the cross-section contraction is not considered [254]. Landry et al. [255] simplified the pores of nanoporous organic matter as packing spheres. The pure CH_4 viscous and slippage flow in these reconstructions is simulated with a microscopic local-effective-viscosity LBM (LEV-LBM), and the effective relaxation time is corrected at every node to involve the variance of the mean free path of a shale gas molecule in the bounded system. Their result shows that the bundle of capillary models overestimates the apparent permeability because of ignorance about the pore space connectivity and the shape.

These developments enhance the contemporary of shale flow behaviors. However, as previously mentioned, it is difficult for the microscopic LBM to address with the slippage boundary of an irregular pore surface; this limits its application in real stochastic shale pore structures based on a high-resolution scanning of shale samples. Although the conventional LBM does not have this limitation by imposing a no-slip bounce-back boundary scheme, it is unable to involve slippage velocity on the pore surface. In view of this, Chen et al. [256]

adopted the DGM-LBM mentioned above to overcome this deficiency. The conventional LBM with the bounce back boundary is employed to calculate the permeability of any complex shale structures. A slip correction factor that considers the gas slippage effect was calculated to correct the intrinsic permeability; therefore, the shale gas apparent permeability can be acquired after correction. To obtain three-dimensional (3D) porous shale structures, the Markov chain Monte Carlo (MCMC) method and two-dimensional (2D) SEM image of shale sample were integrated. The reconstructed shale structures reflect the real shale sample as substantiated by the pore structural statistical information. Thereafter, the shale gas transport behavior was simulated through the DGM-LBM, and the distribution of pressure and streamline in the reconstructed shale was acquired, as indicated in Fig. 15. They found that the Knudsen diffusion affects shale gas transport and the correction factor falls into the slip and transition regime where no Darcy flow regime is observed. Subsequently, using a similar model, Chen et al. [257] also investigated shale gas flow and diffusion in reconstructed nanoscale organic matter within which the pores are treated as intersecting spheres. They concluded that the apparent permeability of shale gas is determined by the intrinsic permeability and Knudsen diffusivity and recommended the use of Knudsen's correction factor in predicting the apparent permeability. Moreover, they proposed a correlation formula to easily obtain the organic matter apparent permeability based on their simulation results. Although the DGM-LBM can easily incorporate the influence of the complicated shale structure, the reasonableness of the slip correction factor remains debatable.

The pursuit of a proper treatment for the irregular slippage boundary condition continued. Zhao et al. [258] further developed the microscopic SRT-LBM based on the reconstructed 3D shale digital rock with the MCMC method and 2D SEM scanning images. In their work, the following advances were achieved: a regularization procedure was introduced to handle the remarkable slippage effect resulting from the high Knudsen number; irregular pore surfaces were classified and labelled in advance to implement a proper slippage boundary condition; the local pore size was calculated to obtain an accurate local effective relaxation time. Their simulation results showed that the effect of porous medium heterogeneity on gas flow capability becomes weak with the increase in Knudsen number. The Klinkenberg model with a suitable correction factor had a better accuracy in predicting the gas slippage effect. Subsequently, to further explore the influence of the rock microscopic structure on gas slippage, Zhao et al. [259] reconstructed several 2D porous structures and adopted the microscopic MRT-LBM with the regularization procedure to simulate the shale gas flow in a nanoscale shale matrix under a high Knudsen effect condition. They found that the gas flow capabilities in small pores and large pores are similar under a high Knudsen number condition (strong transition and free molecular flow regions), and the impact of a porous structural feature is weak. Compatible with their previous work, they also observed that the Klinkenberg model with a proper correction factor can capture the microscopic effect in microscale porous media.

It is acknowledged that the shale matrix is a heterogeneous and anisotropic porous medium that includes inorganic and organic matters. Observing that the pore morphology of organic matter in shales are diverse, Zheng et al. [201] classified them into three typical types, intergranular pore, micro-crack, and “honeycomb” pore structures, and reconstructed the corresponding three-dimensional porous structures as described by Song et al. [260]. Thereafter, they computed the intrinsic and apparent permeabilities of these structures using the conventional and microscopic LBM, respectively. Their results showed that both the nanoscale pore morphology and high-Knudsen effect have a significant impact on the shale gas transport behavior in the shale matrix. Notably, this finding differs from the previous study results reported by Zhao et al. [258,259]. By carefully comparing their work, we find that the inconsistency is attributed to their demarcation in the value of the high Knudsen number. In Zheng et al., $Kn < 0.59$, and the practical high

Knudsen effect is not remarkable, whereas in Zhao et al., $Kn > 1$, even up to 10, where the Knudsen effect is significant. This illustrates that the knowledge on the effect mechanism of high Knudsen number is still vague and remains a relevant research topic.

The aforementioned work focused on the single component of shale, either inorganic or organic matter. To explore the shale gas flow behavior in multicomponent shale structures, Wang et al. [261] calculated the intrinsic and apparent permeability of highly anisotropic and heterogeneous shale structures, and discussed the effects of the shale structural features and high Knudsen number effect on permeability. To upscale the pore-scale information to the field-scale calculation, Wang et al. [262] built a pore-field-iteration method. They found that the shale gas yield is overestimated at the early stage if the real shale gas effect is ignored, whereas it can be underestimated at the late stage (where the reservoir pressure decreases) if the high Knudsen number effect is ignored.

In the shale matrix, the influence of adsorbed gas is evident with the pore size smaller than 10 nm where the adsorbed shale gas layer constitutes a significant fraction of shale pores, and the pore cross-section is significantly reduced. More importantly, the late stage gas yield relies on the contribution of adsorbed gas production [263]. Hence, the effects of adsorbed gas during the gas production process are studied. The next section discusses a series of pore-scale LB models employed in the study of adsorbed gas. The research described above is indispensable for understanding the shale gas flow mechanisms in shale nanoporous structures. However, porosities in these work are generally larger than those in real shale rock (< 0.1), and the dominant transport mechanism for gas transport in tight rock may differ from that in the loosened porous structures. Thus, more attention should be paid to the gas transport mechanisms in nanoporous structures, with porosity < 0.1 .

5.3.2. Viscous flow coupled with the slippage effect and surface diffusion

The shale gas adsorbed on the surface of pores is widely assumed as the monolayer adsorption following the Langmuir isotherm theory. The amount of adsorbed gas molecules and gas coverage on the pore wall increases with the reservoir pressure. The contribution of adsorbed gas mainly includes two aspects. First, the adsorbed gas reduces the pore cross-section; this leads to an increment in the slippage effect. Thereafter, the adsorbed gas moves forward along the pore surface driven by the chemical potential gradient; this is known as surface diffusion, and the surface diffusion capability is decided by the interaction strength between the solid wall and adsorbed gas molecule [215]. To consider the decrease in pore cross-section, two major models are developed.

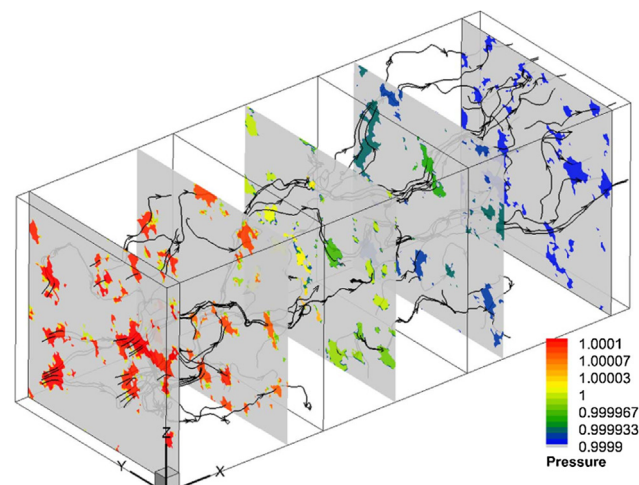


Fig. 15. Distribution of pressure and streamline in the reconstructed shale during the shale gas flow. Reprinted with permission from Ref. [256].

- (1) Adsorbed layer model. This model only focuses on the macroscopic adsorption performance rather than the microscopic behavior of every adsorbed molecule; it is assumed that the effective pore sizes (considering the adsorbed molecule) are the difference between the original pore sizes (without the adsorbed molecule) and the adsorbed layer thickness. In terms of the monolayer adsorption in the shale matrix, the adsorbed layer thickness is the diameter of the adsorbed gas molecule. Subsequently, certain researchers indicated that the shale gas coverage decreases with the increase in pore pressure, and a constant adsorbed layer thickness might misestimate the gas transport capability. Accordingly, the concept of effective thickness of the adsorbed layer is proposed; this effective thickness is a function of the gas coverage and diameter of the adsorbed gas molecule and is affected by the gas adsorption characteristic [264].
- (2) Adsorption site model. This model is built from the microscopic adsorption behavior of shale gas molecules. It artificially constructs the adsorbed gas molecule at potential adsorption sites derived from the assumption of the Langmuir adsorption theory [265]. The adsorbed gas molecule is constructed in the following process: first, all potential adsorption sites are labeled; second, the adsorbed gas molecules are stochastically placed without mutual interactions at the potential adsorption sites. The quantity of adsorbed molecules is determined by the gas coverage [266].

The adsorbed layer model is initially employed in the analytical model with the capillary structure because of its simplicity [264]. This model was first coupled with the microscale LBM in the work of Ren et al. [215]. They simulated the shale gas flow and surface diffusion in a nano-channel and estimated the contribution of the adsorbed layer on total mass flow rate as the channel height increased. However, it is difficult to extend this model to a simulation of a real shale rock

because of the difficulty in determining the adsorbed layer. Allan and Mavko [266] established the adsorption site model; they induced adsorbed molecules on the pore surfaces of reconstructed 3D rock structures and assumed that the adsorbed molecules are immobile particles adhering on the adsorption sites, and no interaction exists among these molecules. Thereafter, they calculated the permeability of kerogen with the LBM and found that the effective permeability is lower than the Darcy permeability at all pore pressures because of the presence of adsorbed gas. Zhao et al. [267] adopted this model to investigate the shale gas flow in the shale matrix with a regularization LB model; they analyzed the effects of adsorbed gas, surface area and residual water saturation on the apparent permeability of the shale matrix. Moreover, they verified that the adsorption reduced the gas transport space and affected the permeability, especially under a high Kn condition. The adsorption site model partly involves the effect of adsorbed gas, but the calculated permeability may be underestimated because it ignores the surface diffusion derived from the adsorbed gas and the increase in slippage effect caused by the reduced pore size.

To incorporate the movement of the adsorbed gas molecules, Fathi and Akkutlu [252] proposed the novel Langmuir-slip LB model, in which the transport of adsorbed gas is treated as a wall movement; the movement velocity is the combination of local wall velocity caused by the adsorbed gas and free gas slippage velocity far from the wall with one mean free path. They found that beyond the existing critical Knudsen number, the gas transport capability improves; the slippage effect and surface transport cause remarkable molecular streaming. Later, Zuo et al. [268] developed a new boundary scheme to incorporate the Langmuir slip boundary into the microscopic SRT-LBM and simulated the shale gas transport process in a tree-like porous structure. Unfortunately, the change in the transport space occupied by the adsorbed gas is ignored in these works.

Indeed, the nature of the physical adsorption of gas is the process

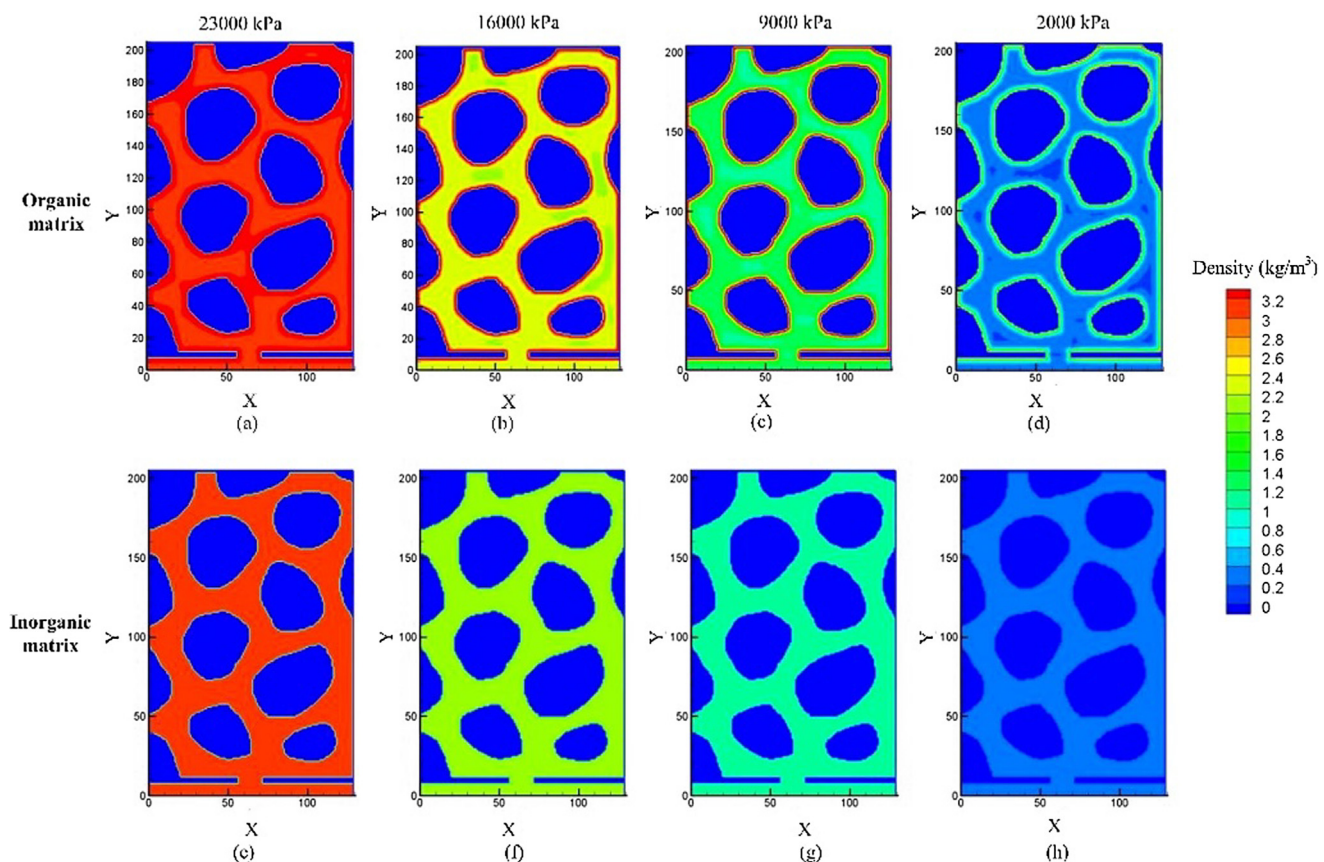


Fig. 16. Gas density distribution in organic and inorganic porous media under different pressures. Reprinted with permission from a modified version of Ref. [275].

whereby van der Waals forces cause gas molecules to adhere to a surface. The gas adsorption behavior can be captured if a proper interaction force is exactly implemented. Based on this idea, a new microscopic LBM with an external force term that represents the interaction between solid surfaces and adsorbed gas molecules is developed to handle the adsorption effect [269]. For example, Ning et al. [270] simulated the complex transport behaviors of shale gas in 2D porous structures with an external adsorptive force, and found that the adsorbed gas surface diffusion is significant when the Kn is large (approximately 0.5), and the adsorption effects weaken as the pore size increases. Ning et al. [271] investigated the CH_4 flow in 3D reconstructed nanoporous kerogen. They found that permeability decreases as the pressure increases, and it is overestimated when the adsorption effect is ignored. To further estimate the effect of adsorbed gas, Ning et al. [272] reconstructed multi-scale digital rocks composed of kerogen and other inorganic matters; they predicted the apparent permeability of the reconstructed rocks and found that the ignoring surface diffusion can reduce the gas permeability in the shale matrix.

It is noteworthy that the adsorptive force is a key parameter in estimating the contribution of adsorbed gas in the abovementioned model. To represent this force accurately, the related adsorption parameters should be predicted by the DFT, GCMC, and MD methods. Being aware of this problem, Ning et al. [273] coupled the MD results into the LBM and further proposed an upscaling workflow to predict the permeability of the multiscale shale matrix. They found that the permeability of a nano-CT digital rock is significantly smaller than kerogen permeability. Zhang and Sun [274] coupled the LBM with a dynamic sorption model, which includes the absorbed amount, advection diffusion, and free flow velocities, to study the gas flow and transport in the shale matrix. They reported that the free flow velocity will not be slowed with an increase in adsorbed shale gas amount. Similarly, Zhao et al. [275] also treated the MD results as the input parameters and compared the shale gas transport differences between porous organic matter with adsorbed gas and inorganic matter without adsorption gas; the comparison is shown in Fig. 16. The results reveal that the gas production in organic matter is significantly influenced by the excess adsorption curve of shale gas. Although the adsorbed gas increases the gas reserves, it is difficult to produce and leads to a lower gas recovery of the organic porous medium.

In these works, although the adsorptive force considers the adhesion of adsorbed gas on the wall, the correction for the slip boundary condition is neglected. The slip boundary condition that is suitable for single free gas should not be imposed directly in this situation where

the presence of adsorbed gas changes the gas-wall interaction. The surface diffusion velocity derived from the adsorbed gas also influences the slip velocity adjacent to the wall. Therefore, in the future work, the slip boundary condition should be corrected to involve the multiple effects, based on the results from the DFT, GCMC, and MD methods.

6. Shale gas flow and transfer at macropore level

6.1. General knowledge

At the macropore level, the zone size of the shale matrix ranges from a few macro meters to several kilometers ($Kn < 0.001$). Thus, the complex pore and fracture structures in the shale gas reservoir control the complicated flow mechanism. This is because, with the pressure decreasing, shale gas molecules desorb from the shale matrix micropore surface. After the desorbed shale gas molecules converge in the fracture, system free gas is produced. Subsequently, differences in the concentration and pressure between the matrix and fracture systems are formed, and shale gas in the shale matrix migrates to the reservoir system (wellbore); a mass flow is also induced. Therefore, the gas transport process includes adsorption /desorption, Knudsen diffusion, and viscous flow in the entire exploitation process [276], as shown in Fig. 17.

In fact, accurate models to describe the shale gas transport should include the complex shale gas transport mechanism along with the phase behavior in the shale nanopores and different fracture systems of the shale matrix; permeability, diffusion, and mass flow all affect the recovery time and amount of shale gas production [277,278]. Thus, the GCMC and MD results such as the adsorbed amount, adsorbed heat, and diffusion coefficient are adopted as the input parameters of macro-methods. The properties of mass flow in shale matrix can be divided into the mesoscopic and macropore, which can be solved by LBM and macro-methods coupled together.

6.2. Shale matrix diffusivity

The shale gas diffusion caused by the concentration difference is an important gas transport factor in the shale matrix; this is different from the molecule diffusion described in Section 4. The diffusion in the pores consists of Fick diffusion ($Kn \leq 0.1$), transition diffusion ($0.1 < Kn < 10$), and Knudsen diffusion ($Kn \geq 10$) according to the value of Kn [279]. The free volume theory [280], bi-disperse diffusion model [281], semi-analytical model [282], analytical model considering the effect of

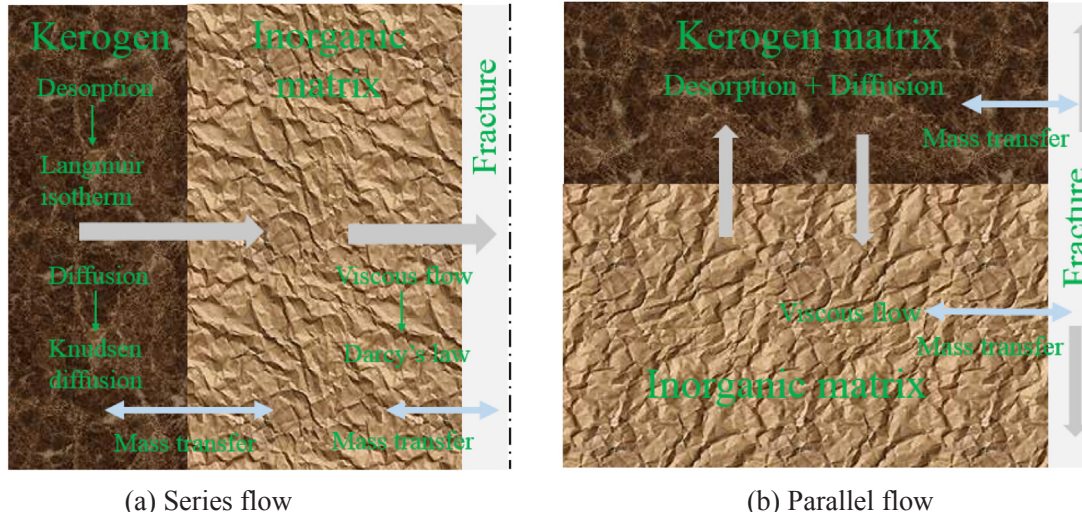


Fig. 17. Gas flow and transport sequence for series and parallel flow in the shale matrix, respectively. Reprinted with permission from a modified version of Ref. [276].

the Knudsen diffusion, bulk diffusion and slip flow [18], the approaching equilibrium adsorption-diffusion method [283], reconstructed shale matrix model [284], and pressure pulse method [285] are built to study the diffusion behavior of shale gas in the shale matrix. However, most models simply adopt the basic diffusion model coupled with other factors that affect the shale gas diffusion in the shale crack.

The laws of shale gas diffusion in the shale crack are obtained through a number of different diffusion models. For example, the diffusion in the shale crack is shale gas concentration-dependent. The effective diffusivity increases with an increase in pressure, and it decreases with temperature increase [280]. However, the diffusion coefficients decrease with an increase in the amount of adsorbed gas [286]. Knudsen diffusion performs a key function in gas transport when the shale matrix pore diameter is $< 1 \mu\text{m}$ [287]. Gao et al. [284] found that a high organic content corresponds to a low gas diffusivity. This is because that the amount of shale gas desorption can increase the pore space in the organic matter. The pore channel controls the homogenized diffusivity in the inorganic matter, whereas the organic matter can be treated as the gas source and changes the mechanisms of shale gas transport in the shale matrix.

6.3. Shale matrix permeability

Permeability is the measurement of the ability of a porous medium to allow fluid flow through it. Permeability is an important property of porous media, the transport of a fluid flow through porous media is introduced to the reservoir simulators. It is usually determined either experimentally or numerically based on Darcy's law. For a fluid flow within the continuum flow region, permeability is only affected by the porous structures of a porous medium and is independent of the fluid type. When the size of pores in a porous medium is comparable to the mean free path of gas, slippage occurs on the pore walls. Gas slippage and its effects on permeability in tight porous media was first studied by Klinkenberg in 1941 [288]. Klinkenberg showed that slippage on the rock surface can increase the measured gas permeability (apparent

permeability). He proposed the following first-order equation which relates the gas permeability to the intrinsic permeability for steady state and laminar flow through a porous medium

$$k_a = k_\infty f_c, f_c = \left(1 + \frac{b_k}{p}\right) \quad (26)$$

where f_c is the correction factor. k_∞ is called Klinkenberg's corrected permeability, which is the liquid permeability, or the intrinsic permeability unaffected by slippage. Eq. (26) is well established, and the linear dependence of k_a with the reciprocal p is widely observed in many rocks. k_d only depends on the porous structures of a porous medium. b_k is the Klinkenberg's slippage factor, which is expressed as

$$\frac{b_k}{p} = \frac{4c\lambda}{r} \approx 4Kn, c \approx 1 \quad (27)$$

Various expressions of b_k have been proposed in the literature. Heid et al. [249] and Jones and Owens [289] proposed similar expressions relating b_k to k_d . Sampath and Keighin [290] and Florence et al. [291] related b_k to k_d/ε . Beskok and Karniadakis [292] developed a second-order correlation

$$f_c = (1 + \alpha(Kn)Kn) \left[1 + \frac{4Kn}{1 - bKn} \right], \alpha(Kn) = \frac{1.358}{1 + 0.170Kn^{-0.4348}} \quad (28)$$

where b is the slip coefficient and is equal to -1 for slip flow. $\alpha(Kn)$ is the rarefaction coefficient and its expression is proposed by Civan [293] with a simplified expression. Eq. (28) is also called Beskok and Karniadakis-Civan's correlation in the present study. This equation covers the entire four flow regimes, and such ability to describe all the flow regimes in one equation alone with a simple form is really useful [293].

In the oil/gas industry, Darcy's law [Eq. (21)] has been broadly adopted to describe a fluid flow in a porous medium. However, the conventional Darcy's law cannot realistically describe the variety of flow regimes other than the viscous flow regime such as Knudsen diffusion [21]. The current reservoir-scale models therefore should be improved if applied to shale gas modeling. Javadpour [37] proposed to

Table 3

Built permeability models reported in literature.

Model description	Comments	References
A flow equation that considers slip and pore geometry effect	The simplified circular pore model leads the value of shale gas apparent permeability to be overestimated	Afsharpoor et al. [299]
An organic pore permeability model that considers adsorption and desorption, Knudsen and surface diffusion, viscous flow, real gas effects, stress dependence, and phase behavior	The model has predicted the value of the apparent organic pore permeability successfully	Song et al. [300]
A pressure-dependent permeability model that contains the coupling of matrix flow with both multiple flow regimes and stress-strain relationship	The built model can predict the hydrostatic permeability at the laboratory scale	Wang et al. [301]
A permeability model that considers the effects of higher-order slip effect	The model only depends on Langmuir sorption isotherm data, pore size, and pressure of shale sample [302,303]	Singh et al. [304]
A semi-empirical method that considers the analytical solution of the continuity equation including the effect of the gas desorption	The model can capture the effects of pore pressure on shale gas permeability	Alfi et al. [305]
A permeability model that considers the porous-elastic and superposition of fluid-dynamics effects	The model predicts well the apparent permeability during the depletion of the shale gas reservoir, with the pressure varying from 10,000 to 2000 kPa	Fink et al. [306]
A permeability model that considers the Knudsen diffusion and viscous flow of free gas and the adsorbed gas surface diffusion	The surface diffusion is decisive when the shale matrix pore radius is small or the shale reservoir pressure is low; otherwise, the viscous flow is decisive	Zhang et al. [307]
A permeability model that considers the micro / nano-pores and natural fracture as well as the effects of the liquid slip, pore size distribution and geometry and the organic content	The value of the permeability in the horizontal direction is almost twice higher than that in the vertical direction	Feng et al. [308]
A permeability model that considers bulk-gas transport regimes, organic pores, gas desorption, and surface diffusion in the nanotubes (organic) and slit nanopores (inorganic)	The surface diffusion is the domination once the pore size of organic matter is $< 2 \text{ nm}$. While for inorganic pore, the transport capacity increases with an increase in the pore radius	Sun et al. [309]
A micro-continuum model that considers the resolved pore and nano-porous region	The total shale matrix permeability has a relationship with the time scale when the pressure is fixed; Stokes flow controls the permeability early whereas the surface diffusion controls it at later time	Guo et al. [310]
A pore structure model that considers the effect of the real gas	With organic pore radius of $< 20 \text{ nm}$, the permeability is overestimated at least 40% of the CH_4 permeability	Song et al. [311]
A shale apparent permeability model that considers the variable boundary conditions	The results obtained from the different boundary conditions match well with the experimental data	Peng et al. [312]

adopt the apparent permeability rather than the intrinsic permeability in Darcy's law, where the flux term can still be expressed in the form of the Darcy equation. This scheme is of great practical importance as it is really convenient for the current commercial numerical simulation software in the oil/gas industry. Correspondingly, recently efforts have been devoted to incorporate other influencing factors, such as adsorption, surface diffusion, and mechanical compression, into the apparent permeability [294]. The permeability in the fracture system is also a key property in the process of shale gas production prediction; the permeability of shale can control the imbibition rate [295,296]. Moreover, the fracture aperture, displacement, fracture propagation, and different physical, chemical and mechanical mechanisms are also sensitive to permeability [37,291,293,297,298].

6.3.1. Permeability prediction of macroscale shale matrix

A series of permeability models built to study the permeability in the shale matrix are listed in Table 3.

In the list in Table 3, it can be noted that the factors affecting shale gas permeability are varied; to a certain extent, no model can consider all factors. Song et al. [313] included the CH₄ permeability with the surface diffusion caused by the adsorbed phase and transport caused by bulk state CH₄, as shown in Fig. 18.

The factors, such as the anisotropic ratio of Young's modulus [314], principal stress [315,316], stresses [317], surface coverage [318], pore pressures [319,320], the TOC and structural parameters of both organic and inorganic systems [321], and the heterogeneity of the shale gas reservoir [322] on the permeability in the shale matrix are discussed in detail. Sheng et al. [323] found that the compressibility becomes the key factor affecting the permeability of inorganic materials with the pore size smaller than 10 nm.

Moreover, the influences of permeability on shale gas transport and production are also investigated. Cao et al. [324] found that the effect of flow regimes is close to the permeability of an inorganic matrix. Fracture compressibility, which will decrease with the increase in shale permeability, is significantly influenced by the flow direction; it also varies with the shale matrix mineralogical composition. Pressure diffusion is also affected by the shale gas permeability. Bustin et al. [325] found that the permeability below which gas production is sub-economic varies with the fracture spacing; the permeability also has a

considerable effect on the shale gas production with a large fracture permeability.

6.3.2. Permeability prediction of representative elementary volume scale shale matrix

Each component in the shale has its own pore characteristics [55,86,326,327]. Therefore, the contents and distributions of OM and different inorganic minerals in the shale matrix, which are affected by the mechanical compaction and diagenesis, significantly affect the porosity and permeability of the shale matrix [52]. The "elementary building block" (EBB) model is proposed to consider such relationship between pore morphology and mineralogy. Each component in the shale matrix can be considered as an EBB. A detailed analysis of the pore characteristics in each EBB can be performed on the high-resolution images of shale microstructures provided by ion beam - SEM and broad ion Beam-SEM [55,86,326,327]. A set of morphologic parameters, including pore area, pore perimeter, pore long/short axis length, orientation, convex hull, circularity, convexity, and elongation, can be adopted to comprehensively quantify the pore morphology [86]. EBBs can be further classified based on the pore type proposed by Louck et al. [52], such as EBB with Interparticle (InterP) pores, EBB with IntraP pores, and OM as an independent EBB. The highly heterogeneous microstructures and compositions of the shale can be obtained by combining the right amount of different homogeneous EBB (compositions) and distributing them in a proper way (distributions) [327].

A representative elementary volume (REV)-scale shale matrix is reconstructed based on the EBB model which accounts for distribution and pore morphology of each constituent, and the flowchart of the reconstruction procedure is schematically shown in Fig. 19(a). A four-EBB system is considered including calcite, pyrite, OM and clay. Clay is served as the matrix embedded in which are the grains of other EBB. A 3D REV-scale matrix can be generated by using a reconstruction method called the quartet structure generation set [328]. The granular shapes of calcite, clay and OM embedded in the clay are similar to those observed in the SEM images [51]. Each EBB can be assigned with a specific porosity, porosity for calcite, pyrite, OM and clay as shown in Fig. 19(b). It is worth mentioning that the complex nanosize domain is now actually smaller than a single node with homogeneous assumption in the REV-scale domain. Fully resolving the nanoscale porous

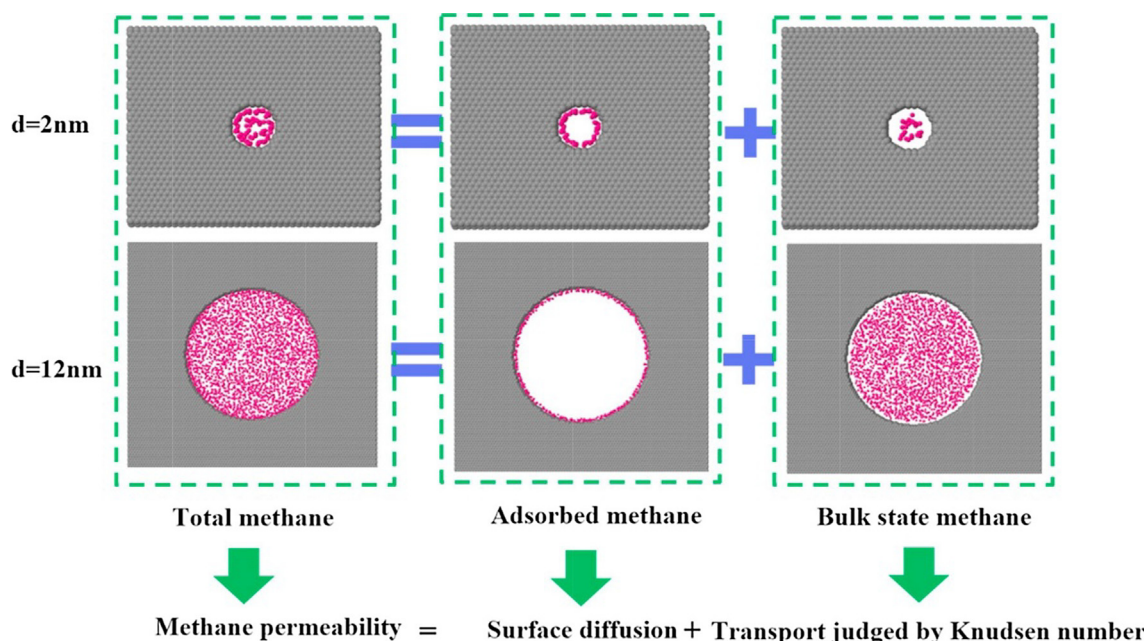


Fig. 18. Contribution of adsorbed CH₄ and CH₄ gas on the total CH₄ permeability with the pore sizes at 2 and 12 nm, respectively, which includes the surface diffusion and transport judged by Knudsen number. Reprinted with permission from Ref. [313].

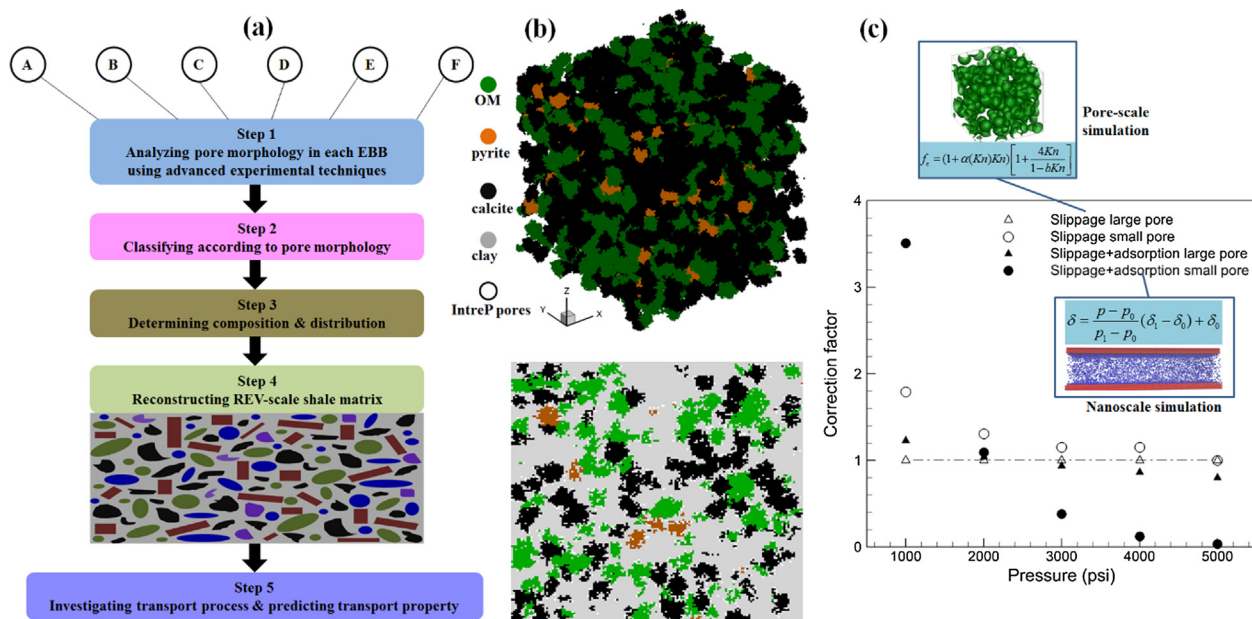


Fig. 19. Properties of shale matrix reconstructed using the elementary building block model;(a) Steps of building block model;(b) A reconstructed 3D REV-scale structures;(c) Effects of slippage and adsorption on the correction factor considering slippage and that without considering slippage. Reprinted with permission from Ref. [333].

structures in the study of the REV with size of hundreds of microns is impractical because huge computational resources would be required [329].

Wang et al. [330] modified the force term in the generalized Navier-Stokes equations for an isothermal fluid flow in porous media proposed by Nihiarasu et al. [331] to incorporate the effects of the gas slippage phenomenon (Klinkenberg's effect)

$$\nabla \cdot \mathbf{u} = 0 \quad (29a)$$

$$\frac{\partial \mathbf{u}}{\partial t} + (\mathbf{u} \cdot \nabla) \frac{\mathbf{u}}{\phi} = -\frac{1}{\rho} \nabla(\phi p) + v \nabla^2 \mathbf{u} + \mathbf{F} \quad (29b)$$

$$\mathbf{F} = -\frac{\phi v}{k_a} \mathbf{u} + \varepsilon \mathbf{G} \quad (29c)$$

where \mathbf{u} is the superficial velocity vector, and v is the kinematic viscosity, ϕ is the porosity of the shale matrix. The force term \mathbf{F} represents the linear (Darcy) drag force due to the presence of porous media and other external body forces \mathbf{G} . The nonlinear (Forchheimer) drag force is not considered because the flow rate is extremely low in low-permeability tight porous media such as the shale matrix [21]. The simulation results of shale gas transport are upscaled into the REV-scale study by using the second-order correlation Beskok and Karniadakis-Civan correlations [292] to determine k_a based on k_d (Eq. (28)). The intrinsic permeability k_d is determined by a relationship between local porosity and permeability fitted from the experimental data [19].

Sensitive studies of several parameters are conducted for their effects on the effective permeability of the REV-scale shale matrix, k_{REV} . For OM with relatively higher porosity, k_{REV} increases as the TOC increases. The effective permeability not only depends on the property and volume fraction of each constituent, but also on the details of the microstructures such as grain size. For fine-grained mudrocks, the grain size in the shale varies from a few microns to tens of microns [51,52]. It is found that no matter whether the permeability of a certain constituent is higher or lower than the clay matrix, decreasing the grain size leads to higher REV-scale k_{REV} based on the uniformity principle of field (velocity, temperature) gradient [332]. Interparticle pores, which are widely observed between grains and crystals in shale samples especially those from young or shallow-buried sediments [52], are important components of shale pore systems and can contribute

significantly to the effective pore networks in the shale matrix.

The effects of complex physical processes including slippage and adsorption on the effective permeability of the REV shale matrix are also studied. The nanoscale and pore-scale results in previous sections are upscaled into the REV-scale study. The slippage is considered using the Beskok and Karniadakis-Civan correlations, as shown in Fig. 19(c). Two cases are considered, with one having averaged pore size of approximately 41 nm (large pore case) and the other 1.69 nm (small pore case). With only the slippage effect considered, for the large pore case, Kn is low and the slippage effect is almost negligible, which leads to the ratio between apparent permeability and intrinsic permeability, namely the correction factor, very close to unity; for the smaller pore case, the Kn number is relatively high and the slippage effect becomes remarkable. The lower the pressure is, the higher the correction factor. The MFP increases as the pressure drops, resulting in higher Kn , which can be inferred from Fig. 19(c).

As previously discussed, adsorption affects the gas transport in a pore in two ways: it reduces the pore size and changes the gas-wall interaction. The latter one, is very complicated and still requires further investigations, even qualitative one. Therefore, only the former effect is considered. The pressure-dependent thickness of the adsorption layer, proposed based on the nanoscale GCMC and MD simulations, is subtracted from the local pore radius. The results indicate that adsorption plays complicated roles on the effective permeability. Actually, adsorption has two opposite effects on k_{REV} . On the one hand, the adsorption layer reduces the pore size and thus leads to a lower permeability. On the other hand, as the pore size decreases, Kn increases and the slippage effects are stronger, resulting in a higher permeability. Which effect plays a dominant role depends on the pressure. Under higher pressure, the former effect dominates as the thickness of adsorption increases with pressure, whereas, under lower pressure, the latter effect prevails because of the high Kn . Therefore, the correction factor is less than unity under higher pressures and greater than unity under lower pressures. Particularly for the small pore case at a pressure of 5000 psi (1psi = 6894.75 Pa), the correction factor for the small pore case is almost zero, indicating that the pore is almost completely occupied by the adsorbed layer; and for a pressure of 1000 psi, the correction factor is as high as 3.5, implying the strong effect of slippage in the pore with reduced size as shown in Fig. 19(c).

Lately, Naraghi and Javadpour [329] conducted similar studies. They reconstructed a two-EBB system with OM as one EBB and all the other inorganic matter as another EBB. OM patches are randomly dispersed within the inorganic mineral EBB. The pore radius was assigned to OM and inorganic mineral EBB using a pore size distribution experimentally obtained, based on which the local permeability was calculated. Their studies also demonstrated the important role of TOC, slippage and adsorption on the effective permeability of the REV-scale shale matrix. Subsequently, Chen et al. [333] simulated gas transport in a multicomponent shale matrix that included clay, calcite, pyrite, and organic matter, and discussed the effects of organic content, grain size, and interparticle pores on the shale matrix permeability. It was found that the presence of small gains and interparticle pores can improve the permeability of the shale matrix. The contribution of adsorption in the permeability depends greatly on the pore pressure. Wang et al. [334] predicted the gas permeability in the shale matrix considering the surface diffusion of the adsorbed gas. They emphasized that the permeability is significantly influenced by surface diffusion. The contribution of surface diffusion is larger than the Knudsen diffusion and viscous flow in the low pressure and small pores.

6.4. Shale gas flow in the shale matrix

6.4.1. Shale gas flow in the shale matrix at macroscale

After undergoing adsorption and desorption, diffusion, and permeation, the shale gas in the shale matrix crystal migrates to the fracture system and flows into the wellbore. Apart from the MD and LB methods, which can calculate the shale gas flow in the micro-level and pore-level, the finite volume method (Navier-Stokes equation [335–337], semi-analytical modeling [338,339], empirical equation methods [340,341], fracture modeling [321,342–344], and pore network modeling [345,346]), is widely adopted to describe the shale gas

flow during shale transport. The Navier-Stokes equations for shale gas flow in the shale matrix can be expressed as

$$\frac{\partial(\phi\rho)}{\partial t} + \nabla \cdot (\rho\mathbf{u}) = S \quad (30a)$$

$$\frac{\partial(\rho\mathbf{u})}{\partial t} + (\mathbf{u} \cdot \nabla) \frac{(\rho\mathbf{u})}{\phi} = -\nabla(\phi p) + \nu\nabla^2(\rho\mathbf{u}) + \rho F \quad (30b)$$

where S is the source that represents the shale gas production rate. The varied expression formulas for shale gas flow can be obtained from Eqs. (30a) and (30b). Table 4 summarizes the models of shale gas flow in the shale matrix reported in the literature.

The list in Table 4 indicates that although several models that describe the shale gas transport in the shale matrix have been built, there is no model that can include all the factors that affects shale gas transport. In fact, a general model, which can consider all the factors that affect the shale gas flow, should be developed.

6.4.2. Shale gas flow in the shale matrix at representative elementary volume scale

A REV of a porous medium is the smallest volume for which large fluctuations of observed quantities no longer occur, and thus, scale characteristics of a porous flow hold [362]. When a volume is smaller than the correlation length of the heterogeneity in a porous medium, a measured property tends to vary, while in the REV, the heterogeneity can be confidently averaged [363]. The introduction of REV, where a heterogeneous field is replaced with a hypothetical homogeneous one, is critical because for large-scale models (e.g., at reservoir scale) of engineering interest, the heterogeneities at a smaller scale cannot be included explicitly due to computational limitations [362].

Determining the REV size of the shale matrix is challenging owing to the heterogeneous shale matrix with complex porous structures and

Table 4
Models for shale gas flow in the shale matrix reported in the literature.

Model description	Comments	References
A dual-continuum shale gas transport model that includes the effect of adsorption, diffusion and rock stress sensitivity	The slippage has an obvious influence on the low permeability formations	Hao et al. [347]
A multi-scale model that includes the equation of free gas state, adsorption isotherm, and mass balance equations	The shale gas production rate depends on the kerogen component	Akkutlu et al. [348]
A micro-scale multiple-porosity model that considers the natural fractures, organic and inorganic matter	The complex flow mechanisms can be extended to the shale reservoir by upscaling techniques	Yan et al. [349]
The fracture network model that considers that the adsorbed and free gas are stored and slip flow, and non-Darcy flow in the pore spaces	The production data can be used for estimating in a period lasting three years	Kudapa et al. [350]
A semi-analytical model for the complex horizontal wells with nanopores and hydraulic fractures that considers the shale gas slippage, diffusion and desorption, and pressure-dependent fracture	The gas transport mechanism, complex fracture geometries and pressure-dependent fractures perform a key role in controlling the well shale gas productivity and recovery	Hu et al. [351]
A gas flow in the organic matter model that considers matrix shrinkage, diffusion, adsorption layer thickness, and stress sensitivity	The effect of matrix shrinkage and diffusion on shale gas production is ignored, while the adsorption layer thickness and stress sensitivity have an impact on shale gas production	Cao et al. [352]
The mathematical model that contains the motion equation for shale gas transport in the multi-scale shale matrix	With the increase in fracture length, the flow rate first increases and thereafter becomes a stability	Song et al. [353]
A nonlinear transport model that incorporates the important physical processes such as transition flow, continuous flow, Knudsen diffusion, slip flow and adsorption and desorption	It can produce a nonlinear advection-diffusion, associated with highly nonlinear convective flux, compressibility coefficients, and diffusivity	Ali et al. [354]
A discrete fracture model that considers the complex network of fractures	The developed model can accurately capture the coupled process by a few multi-scale basis functions	Akkutlu et al. [355]
A multi-scale model for shale gas transport in the shale matrix that couples the MD, GCMC and LB methods	The gas transport in the micro-scale organic pores is significant and has a nontrivial impact on the cumulative shale gas recovery from an unconventional reservoir	Takbiri-Borujeni et al. [356]
A triple-porosity and discrete fracture network model that considers the gas slippage and Knudsen diffusion	The intra-porosity connections have negligible influence on the shale gas flux, whereas they have different levels of importance in the shale gas production	Yan et al. [357]
A gas transport model that combines the MD simulations, pore network model, and analytical model	Shale gas transport is influenced by pressure in the shale reservoir	Yu et al. [358]
A hybrid model that considers the hydraulic and micro-fractures	Hydraulic fracture length has influence on the gas production below the critical values	Liu et al. [359]
Temporal scale analysis that considers heterogeneity and anisotropy	The propagation of pressure can be influenced appropriately in the temporal scale analysis	Li et al. [360]
A multiple transport considers the real gas effect-adsorption coupling	Surface diffusion plays a key effect when the nano pore is < 2 nm	Wu et al. [361]

varying compositions [364]. For the shale gas transport investigation, heterogeneity specifically applies to the variability that affects the fluid flow and mass transport, such as the geometrical parameters (e.g., porosity, specific surface area) and the transport properties (e.g., permeability, effective diffusivity) [365]. Therefore, the REV for shale gas transport may differ for the different parameters or properties under consideration [365,366]. One approach to obtain the REV size is to measure the properties of a large sample, then divide it into subdomains and perform measurements on the smaller subdomains. Owing to the structural heterogeneity, the REVs at different locations of a sufficiently large sample may be different [363]. Therefore, Zhang et al. [367] proposed the concept of a statistical REV (sREV), defined as the REV above which the statistics of the measured property vary insignificantly. For example, the mean value of the measured property becomes approximately constant and the coefficient of variation (COV, defined as the standard deviation normalized by the mean value) is less than a certain value. Under a COV of 20%, the sREV of a 3D kerogen ($3.4 \times 1.4 \times 1.2 \mu\text{m}^3$) obtained using high-resolution FIB-SEM was established as 360 nm and 960 nm with porosity and permeability as the measured property, respectively [366]. A shale rock sample with size of approximately $65 \times 65 \times 65 \mu\text{m}^3$, with X-ray images, was divided into several subdomains. The porosity of the original sample and the subdomains was measured and the determined sREV size was approximately 30 μm . While the FIB-SEM has the advantage of high resolution up to a few nanometers, it suffers from limited view areas [86]. Therefore, an undesirable scenario may occur if the sample size is not large enough for REV analysis. Keller et al. [364] thus extrapolated their REV analysis curves, and estimated the REV size of a few hundred microns while their samples imaged by FIB-SEM were only $\sim 10 \mu\text{m}^3$ in size. Recently, Saraji and Piri [365] found that for their 3D shale structures ($5 \times 5 \times 5 \sim 30 \times 30 \times 30 \mu\text{m}^3$) obtained by FIB-SEM, the REV size with porosity and permeability was close to the sample size; however, the analysis performed on 2D SEM images with size an order of magnitude higher than the 3D structures led to the REV size (in 2D case, a more accurate term is the representative elementary area, REA) between 300 and 1000 μm , considerably higher than in the 3D analysis. The discrepancy between the above 2D and 3D analysis further demonstrated the sensitivity of the REV size to the sample size, and the sample should be sufficient for the REV analysis. BIB-SEM allows a view area up to 1 mm^2 , which is sufficient for the REA analysis [51,55,86,326,327]. The mineral content is used as the measured

property to determine the REA [55,327], and it is reported that the typical size of the shale REA is between 100 and 200 μm^2 , for example, $140 \times 140 \text{ in } \mu\text{m}^2$ [55] and $140 \times 100 \text{ in } \mu\text{m}^2$ [326].

Based on the REV-scale LBM, Chen et al. [368] simulated the gas flow in the heterogeneous shale matrix that considers the Klinkenberg's effect. They found that Klinkenberg's effect played a key role in the low permeability shale, and this effect increased significantly as the Knudsen number. Moreover, the fractures can greatly improve the gas flow ability leading to a higher global permeability of the shale matrix. Similarly, Zhao et al. [369] used the LBM combining a quartet structure generation set to simulate velocity distributions inside the reconstructed porous media. They found that the gas transport behaviors will be affected by the amount of adsorbed gas in the pore surface. Zhang et al. [370] modelled the oil transport in the heterogeneous shale matrix at the REV-scale, in which the slip effect and varying viscosity of oil are fully considered. Their results indicated that the overall permeability of the shale matrix depended significantly on the total organic carbon content, as a large slip velocity occurred in the nanopores of organic material compared with the inorganic material. Lately, Ren et al. [218] studied the condition of shale gas with/without CO_2 injection. They found that the slip velocity along the micropore and gas-mixture velocity at the outlet become higher with the molar fraction of CH_4 increased.

6.4.3. Multicomponent and multiphase flows at macroscale

Because of the H_2O or CO_2 being injected into the shale fracture to desorb the shale gas molecules [297,371], multicomponent and multiphase flows exist in the shale gas production process. During the shale exploitation, 30%-70% water is still within the reservoir. A two phase flow will take place during the shale gas extraction. As they are formed during the generation of gas/oil, the nanosize pores in the organic matter are generally considered to be gas/oil wetting [19]. Therefore, the solid surface of the organic matter is hydrophobic for the water. The capillary pressure required for water invading into the pores in organic matters are extremely large, due to the nanosize characteristics. Therefore, liquid water is not likely to be present in nanosize pores within the organic matter in which thus single-phase flow occurs. This is commonly recognized in the literature [372]. Of course, models for the multicomponent and multiphase flows existing in the shale gas production process are also built. Hu et al. [351] adopted the semi-analytical model of multiple gas flow in shale matrix nanopores. They

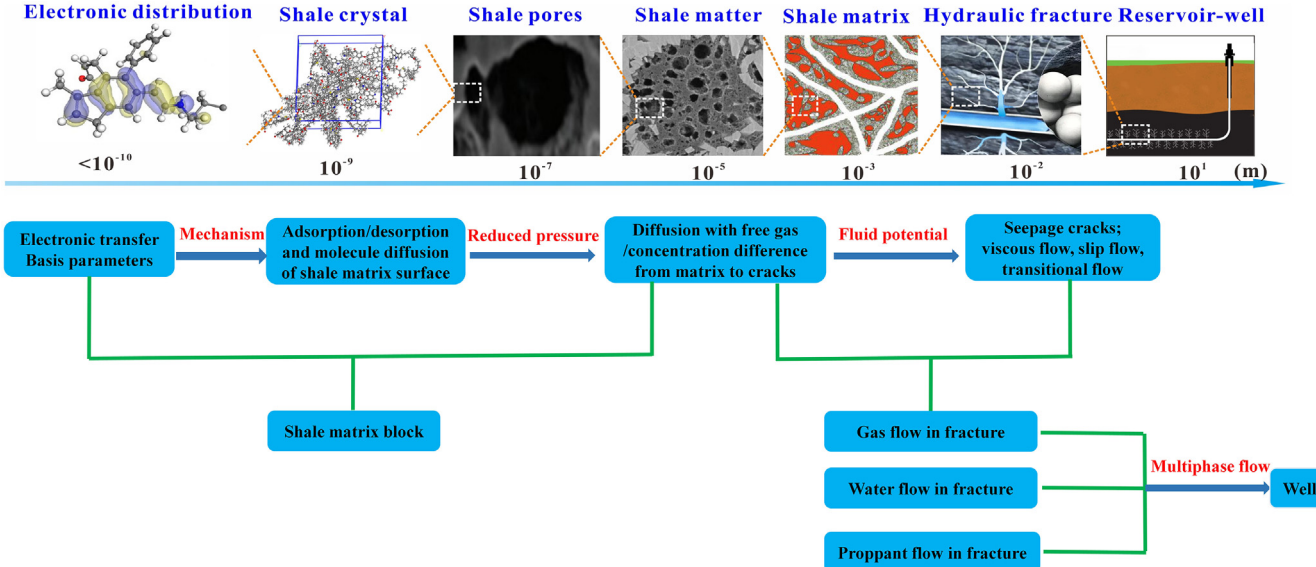


Fig. 20. Characteristic and model description of multicomponent and multiphase flows in a shale reservoir. Reprinted with permission from a modified version of Ref. [374].

found that the pressure-dependent fracture, multiple gas transport mechanisms, and complex fracture geometries perform a key function in controlling the well shale gas productivity and recovery. Osholake et al. [373] considered a multiphase flow on the performance of the designed a multistage hydraulic fracturing process. They found that the result enables engineers to improve the design fracture treatments and better manage the wells in the Marcellus shale gas reservoir. Cao et al. [374] reported that the gas transport in the shale matrix is affected by the multiple transport mechanisms, and the coexistence of multiscale - pore space increases the fluid flow complexity, which is summarized in Fig. 20.

7. Shale gas production at multi-scale level

7.1. General knowledge

The shale gas production rate is the primary factor to assess the amount of shale production that can be produced from the unknown shale matrix. The adsorption isotherms in the shale matrix with different constituents cannot be simply estimated as the sum of the isotherms of individual constituents [375]. The shale production rate is determined by several factors, such as internal factors (shale matrix components, and gas species) and external factors (temperature, pressure, depth, and transport state) together with the flow condition [276]. It is difficult to consider all the factors in one model; therefore, simplified models for predicting shale gas production are widely reported in the literature [376–378]. A typical curve of shale gas production is shown in Fig. 21. The shale gas flow rate will build up when the shale reservoir permeability increases with the removal of liquid during period I. Then, the fracturing liquid is cleared away from the well with flowback fluid to increase the shale gas production during period II. Lastly, the large background fractures in the connected network full of shale gas will be flushed out during period III. The damage zones increase connectivity with the shale matrix and sustain production, and matrix processes, namely, diffusion and desorption, will control the late production during the III period. It is also noted that the trend of shale gas production vs. time varies; the corresponding model should be able to describe this trend. However, every decline curve model has limitations and does not forecast production from the shale gas reservoirs. Especially, when the shale matrix content is different, the shale gas production varies, as shown in Fig. 22. Therefore, the accuracy of the models for shale gas production prediction should be progressively enhanced.

7.2. Factors impacting shale gas production

The shale production rate is determined by geological characteristics [381–384] and flow properties [385–387], such as internal factors (shale matrix components, and gas species) and external factors (temperature, pressure, depth, and transport state). The detailed relationships are shown in Fig. 23.

Numerous investigations have been reported pertaining to factors that affect shale gas production. For example, the quantitative prediction of the adsorbed gas content is distinctly important in the selection of favorable areas and resource assessment for shale gas production because the decline curve in the long term shale gas production is determined by the stage of the adsorbed gas release [388]. Wang et al. [389] considered that gas production from shale gas reservoirs can be enhanced by increasing the reservoir temperature because of the increased desorption of the adsorbed gas. However, Xue et al. [210] discovered that the effects of adsorbed shale gas on the total shale gas production are minimal. They are just dependent on several aspects, such as porosity, reservoir permeability, adsorption behavior, gas flooding pressure, shale channel pore size, temperature, shale component, and hydraulic fracturing effect. Yu et al. [390] assumed that the fractures contribute to the shale gas production once the fracture

spacing is small enough because of the existence of fracture interference. Subsequently, Song et al. [353] observed that the adsorption parameters, initial inorganic matrix permeability, effective stress and flow regimes (Knudsen number) all have an impact on shale gas production. Thereafter, Peng et al. [391] reported that the natural fracture permeability, inorganic pore permeability, Young's modulus of shale matrix, and natural fracture porosity all have positive relationships with the shale gas production rate. Nevertheless, the percentage of adsorbed gas content has negative relationships with the shale gas production rate. The petro-physical properties of shale matrix pores namely, the apparent permeability effective pore radius and porosity, are affected by adsorption and desorption during the gas depressurizing production [392]. Geng et al. [393] discovered that the size of the maximum inorganic pore has a significant influence on the cumulative shale gas production, which can reach up to 13.9% among several fractal pore size parameters. When the number of natural fractures increases to a certain quantity, the shale gas production gradually increases although the abundant natural fractures exist in the shale gas reservoir. The complex shale matrix fracture network can help improve shale gas production. The cumulative shale gas production can increase with an increase in the flow conductivity, hydraulic fracture half-length, number of fractures, and pore spacing. The rapid shale gas production rate at the early gas production stage results in the fast depletion of reservoir energy; for example, the depletion has a negative influence on shale gas production. Zhu et al. [394] noted that the operation for shale gas production enhancement may also be unsuccessful because the connection between the created fracture and the borehole is not strong enough. Presently, no one has found a law that can predict the key factor on shale gas production.

Moreover, Luo et al. [395] found that the gas diffusion mechanism in the nano and micro- scale shale matrix blocks has a significant influence on shale gas production (especially at the early time for shale gas production). A fracture-completed horizontal well with the specific configurations of a quad-porosity shale gas reservoir also has an influence on shale gas production [396,397].

7.3. Models for predicting shale gas production

Because of the varied factors that affect shale gas production, several models have been developed to forecast the shale gas production in the shale gas reservoir. For example, You et al. [398] combined the fractal model with the fuzzy theory to improve the accuracy of the shale

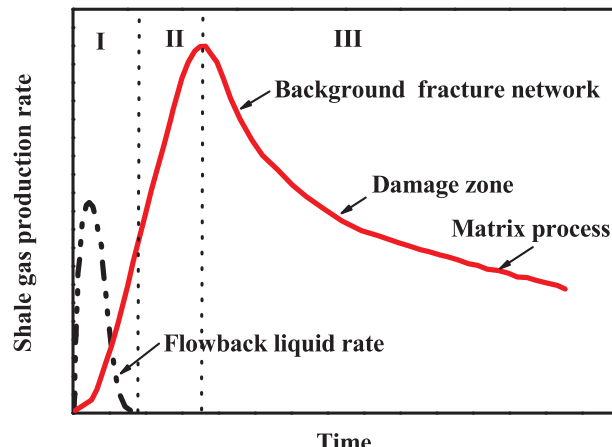


Fig. 21. Profile of shale gas production from a hydraulically fractured reservoir; time periods I, II, and III; period I: increase of shale gas production; period II: peak of shale gas production; period III: decrease of shale gas production, which includes the three processes of background fracture network, damage zone, and matrix process. Reprinted with permission from a modified version of Ref. [379].

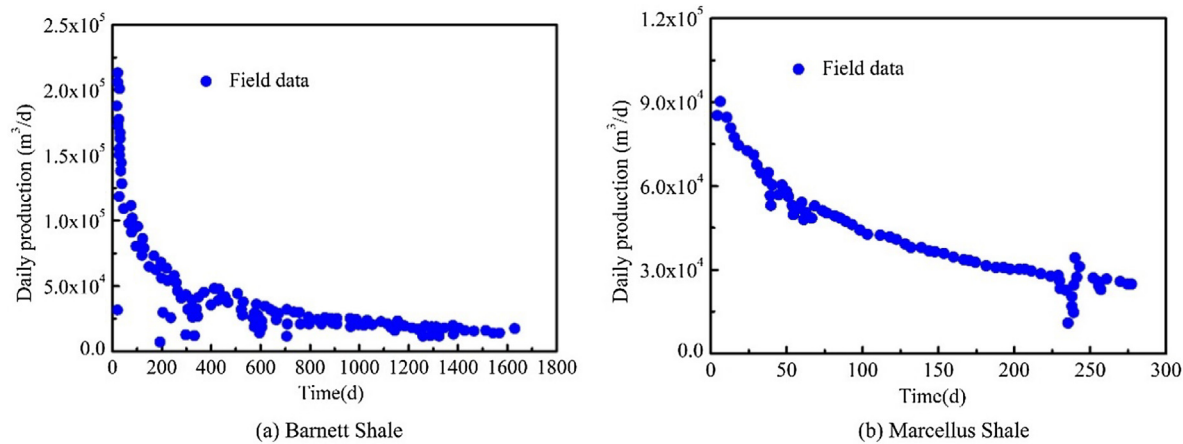


Fig. 22. Shale gas production of the two typical shale gas reservoirs. Reprinted with permission from a modified version of Refs. [324,380].

gas production prediction. Then, Miao et al. [399] built a novel early-late decline model by adopting two fitting parameters, which are only dependent on the characteristics between dense gas self-diffusion / adsorbed gas surface diffusion and shale gas production. Subsequently, another model that incorporates multi-component formulation, CO_2 injection and multiple fractures was also built [371]. They found that the shale gas production lasting for 10 years is followed by the three operation stages, namely, a five-year injection of CO_2 , the brief soaking period, and the final production. Guo et al. [400] analyzed the productivity of different architecture types. They found that the incipient shale gas productivity of blast-fractured wells increases non-linearly with an increase in the number of fracture penetration and radial fractures. The benefit becomes steady as the number of explosives increases with increasing fracture depth. Thereafter, a 3D fracture initiation numerical model for the perforated horizontal wellbore was built [401]. The variations of apparent parameters of gas flow regimes and matrix pores during gas production were found, together with the effective pore radius, apparent permeability and porosity increase during gas production. If the impacts of the adsorbed gas on gas production are ignored, then gas production will be obviously overestimated. The cumulative shale gas production varies slightly when the

increase in adsorption layer thicknesses, but the shale gas recovery factors decrease [402]. Subsequently, transport models that are modified by the Darcy's equation considering the apparent permeability were developed [287]. It was found that shale gas fractures have a significant influence on shale gas production. Shale gas will not be produced economically if the shale matrixes exist without fractures. The shale blocks among the hydraulic fractures can be also regarded as the shale matrixes. It was found that Langmuir parameters will affect both the gas extraction processes and the cumulative gas production [324]. Zhu et al. [376] proposed a multi-physical modeling that included time-lapse, three-dimensional stress; this model includes multiple year scale dynamic production data. A model that has a potential to detect the leaking shale gas from a geologic formation was developed [403]. They found that only 81 days are needed for the rapid detection; however, this method requires that the monitoring well perforation zone be at the same depth as the leakage release point. Then, Lu et al. [404] built a production decline model that incorporates multiple mechanisms for a multi-fractured horizontal well in the shale gas reservoir. They found that the model parameters all have their own sensitivity intensity and influence period. Based on this, Zhang et al. [405] established a triple-continuum model that incorporates a shale

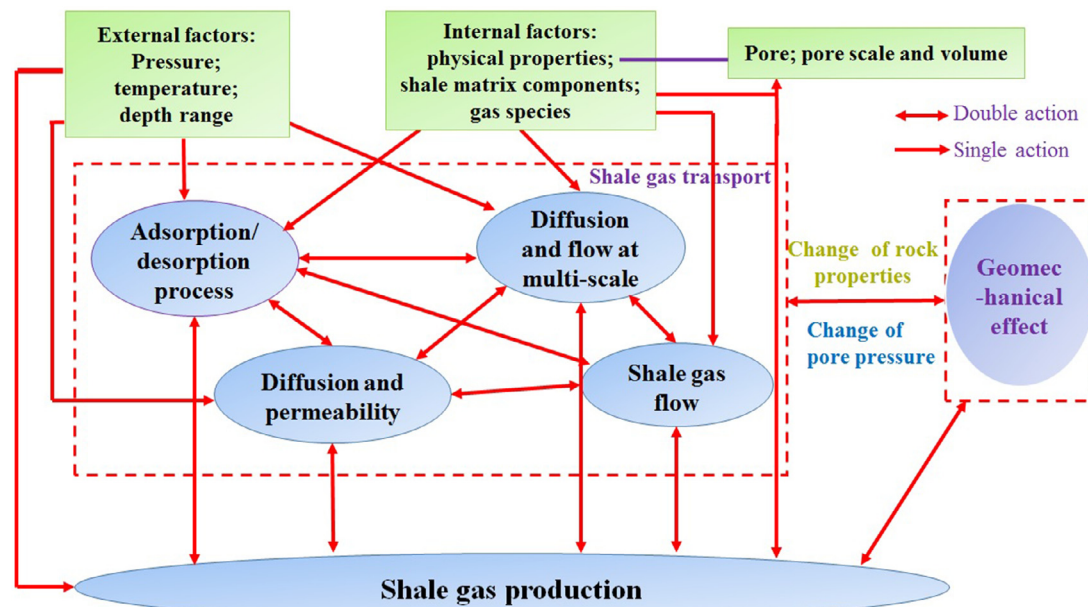


Fig. 23. Factors affecting shale gas production; internal factors (shale matrix components, and gas species) and external factors (temperature, pressure, depth, and transport state) are coupled together during the shale gas production.

matrix with an extremely low permeability, highly permeable hydraulic fracture, and less permeable natural fracture. They reported that the gas rate increases with the increase in meshing size, hydraulic fracture half-length, pressure, and Langmuir volume; however, it increases with a decrease in the spacing of the hydraulic fractures. Hu et al. [406] also established a model considering the full tensor permeability, fluid mass conservation equation, and continuum method. They discovered that the reservoir volume becomes wider in bandwidth and shorter in length with the decrease in the horizontal principal stress difference and natural fracture azimuth angle. Russian et al. [407] presented a multi-continuum physical model, which can be able to reproduce the decreasing shale gas rates compared with experimental data. They also noted that the fracture properties control the decline curve shape at the early time. Then, the properties of shale rocks, which include the heterogeneity, control the shale gas production decline curve before the shale gas production rate drops exponentially. Novotny et al. [408]

established a multi-porosity model for predicting the shale gas production in the shale gas reservoir, which is constructed within the upscaling procedure framework. They found that the pressure equation solutions are strongly determined by the effective hydraulic conductivity and the constitutive response of the retardation parameters, which considers the process of shale gas adsorption and desorption in the kerogen nanopores. Wang et al. [409] built a model including the multi-stage fractured horizontal well; the complex model also contains the influence of viscous flow, surface diffusion, and Knudsen diffusion along with the adsorption layer thickness. They reported that the presence of the adsorption layer in the nanopore surfaces can reduce the effective porosity and pore radius; those results will low the shale gas production from the fractured wells. Considering the adsorption layer and a decrease in pore radius, the production reduction rate will increase. Once the size of the shale matrix pore radius is < 10 nm, the shale gas production from multi-stage fractured wells increases with a

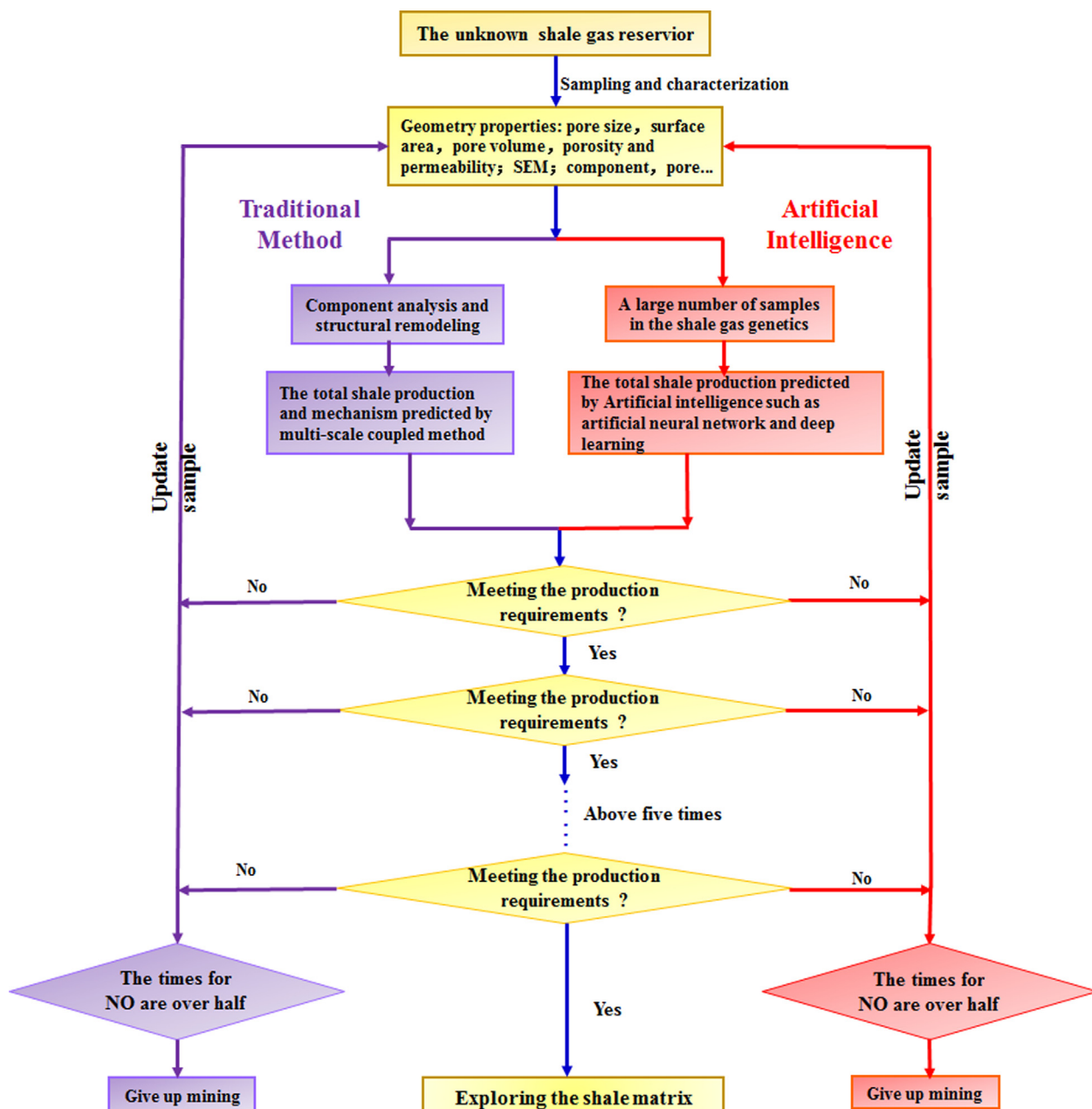


Fig. 24. Genome map for predicting and exploring the shale gas production; two methods (traditional and artificial method) are used together; the traditional method based on multi-scale coupled method; artificial intelligence based on the sample prediction.

decrease in the pore pressure because of the coupled factors of Knudsen diffusion, adsorption layers, and surface diffusion.

To date, the model that describes the coupled effect between factors and shale gas production remains less reported. The model about the optimal infrastructure for shale gas production is also difficult to be determined [410].

8. Species diversity in shale gas production genome

From nanosize pores in kerogen to kilometers of the reservoir scale, the length scale covered during the shale gas generation, migration and production is over 12 magnitudes. Such wide length scale spanned during shale gas extraction, together with the existence of the multi-porosity and multi-permeability systems, the phenomena acting at different scale, and the strongly coupled multiple physicochemical processes, pose great challenges to the simulation of the transport processes in the shale gas reservoirs. A systematic multi-scale analysis is thus required for investigating the multi-scale gas transport processes. To date, such multi-scale studies, especially those particularly focusing on nano/micro/meso/macro-scale, are still in their infancy. Modeling the coupled multiple processes remains a conceptual and mathematical challenge. The challenge arises primarily from (1) the inherent heterogeneity and the uncertainties associated with the characterization of the porous structures of the shale matrix, and (2) the difficulties in conceptualizing and describing coupled physicochemical processes in such a complex system. The heterogeneous nature of shale reservoirs makes it difficult to generate predictive models, resulting in great uncertainty in the gas production forecast. Therefore, various models that describe the adsorption and desorption or gas diffusion and transport have been developed to accurately predict the shale gas production in the unknown shale gas reservoir. In fact, many factors affect the shale gas production, making this aim difficult to be realized. This condition is similar to the directional screening of materials. In recent years, the Materials Genome Initiative, which will accelerate the advanced materials innovation [411–413], has been proposed and successfully used in zeolite [414], metal-organic frameworks [415,416], and covalent organic frameworks [417]. In the present work, the Materials Genome Initiative can be introduced into the prediction of shale gas production

in a similar, which is called the shale gas production genome model. The whole prediction process of shale gas production in the unknown shale gas reservoir is shown in Fig. 24. The proposed models can make it easy to explore the shale gas reservoir. These computational simulations of the gas production genome methods also provide experimental guides for the design of novel materials for gas storage applications. In fact, although there exists the difficulty/limitation of such approaches, which need to have a training set of similar gas shale case studies to train/calibrate the artificial intelligence (AI) machinery (*i.e.* neural network), the AI has been used to predict the properties of shale gas [418–420].

9. Conclusions and outlook

9.1. Conclusions

The production of shale gas is a typical multi-scale process ranging from the electronic level to the macropore level, accompanied by multiple transport mechanisms including gas flow, adsorption, desorption, and diffusion. In this review, the basic transport process of shale gas in the shale gas reservoirs is briefly introduced. The multi-scale phenomena involving shale gas molecules desorbing from the inorganic and organic matrix crystals at the atomic level, diffusion in the crystals at the molecular level and micropores, and flow and diffusion in the mesoscopic pores and macropores are elucidated. The corresponding multi-scale models that describe the above phenomena are discussed in detail. Insight into the whole process of shale gas production model, *i.e.*, the model of the shale gas production genome is proposed according to multi-scale models used in shale gas production prediction. The proposed model of shale gas production genome can be used to guide new shale gas mining; moreover, it can aid understanding the shale transport mechanism, and the optimized exploitation of shale gas reservoir processes in unknown areas.

9.2. Outlook

Increasing and sustaining production while decreasing environmental impacts depends on understanding the physical mechanisms

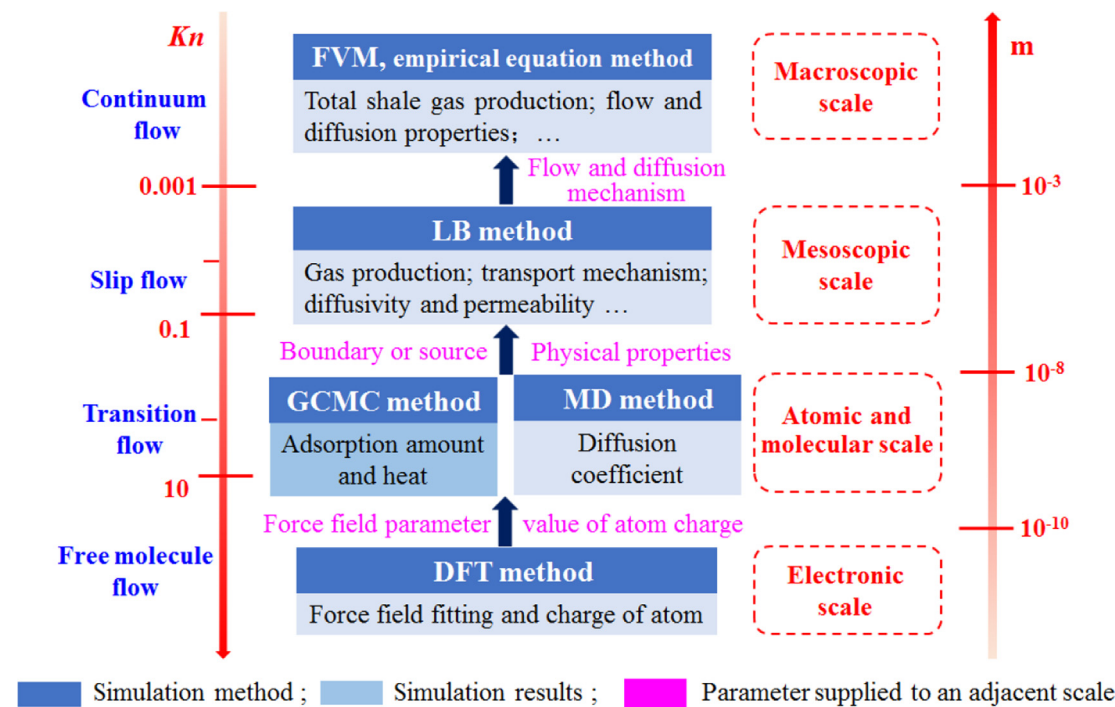


Fig. 25. Computation methods at different scales and intrinsic relationships between two adjacent scale models for shale gas transport in the shale matrix.

that determine extraction. Thus, in recent years, the accurate forecast of production from shale reservoirs has elicited a growing interest from the industry. So far, various techniques to predict shale gas production have been built. Among them, decline curve analysis models have been widely recognized as the easiest and most efficient approach to apply in the prediction of shale gas production. Unfortunately, every decline curve model has also its own limitations that hinder the forecast of production from shale gas reservoirs with full confidence. Furthermore, although the computational performance of computers is significantly enhanced nowadays, the numerical construction process of actual core samples remains time-consuming, with each study case requiring separate modeling. Looking ahead to the future studies, various challenges remain in the predicting the shale gas production by computers. Some of these challenges are listed as follows:

(1) Multicomponent adsorption phase and various substances in the shale matrix

Several types of adsorbates exist in the shale gas and substances in the shale matrix. An accurate model that describes the adsorbate in the shale gas and substances in the shale matrix should be developed. In this regard, knowing the adsorption process in the shale matrix can estimate the total gas concentration in the reservoir; moreover, it aids in achieving the objective of optimizing the production process design and the development of new methods to enhance the desorption process. The GCMC simulations based on the first principle can be used to build the structure of the shale matrix and the adsorption mechanism, and to screen the best adsorption shale matrix. The coupled method enables a quantum chemical description of the interaction between coordination frameworks and adsorbate molecules.

(2) Multi-scale coupled phenomena in the shale matrix

Shale gas transport at the nanoscale level is complex because of the various novel phenomena including surface diffusion, single file diffusion, slippage flow, friction, and activated transport at the interface. The Klinkenberg effect has also been included in Darcy's law to account for slippage; however, such effects are questionable for shale gas

because of the strong interactions between the shale gas molecules and shale matrix. Because the multi-scale coupled phenomenon should be described by different scale governing equations in the shale matrix, a multi-scale approach is needed where the molecular force field parameters required for GCMC simulations can be derived from the first-principle calculations. Moreover, the simulations at different scales allow the investigation of the physicochemical processes underlying the geochemical and transport behavior of these fluids in the interparticle pores and at the surface of the shale matrix. Up-scaling, which is used to describe the scales from the molecule level to the macroscopic level without ignoring the fundamental role of interfaces on the mesoscopic scale, provides a means to capture the complex phenomena, such as the electro kinetic couplings and multi-scale phenomena, as shown in Fig. 25. The parameters such as adsorption amount, diffusion, mass flow, and so on obtained by multi-scale methods can be furtherly used to optimize exploitation of shale gas reservoir processes in unknown areas as described by Striolo and Cole [421] and Sharma et al. [422].

(3) Interface information coupling exchange in the multi-scale method

Owing to the scale effect existing in the mass transfer in the shale matrix, the multi-scale method should be adopted. The interface information exchange between two different scales is considered. Different scales have different information exchange techniques as shown in Fig. 26. The multi-scale method includes domain decomposition, serial, equation free, and embedding. The microscopic and macroscopic models can be fully decoupled. For example, one can simply use separate microscopic simulations to determine the coefficients for the macroscopic models. The information transfer is one-way, such as in the DFT-GCMC, DFT-MD, GCMC-MD, GCMC-MD-LBM-FVM methods. However, as no close forms for constitutive laws exist between two close scales, the unknown terms in the governing equations such as that for stress, should be calculated from the microscopic simulations "on-the-fly". The "two-way" information exchange between two adjacent scales is employed during the whole computation of scales. The two adjacent scale variables are denoted by operators, which include the reconstruction operator or lifting operator and the compression operator or restriction operator. The detail of the interface

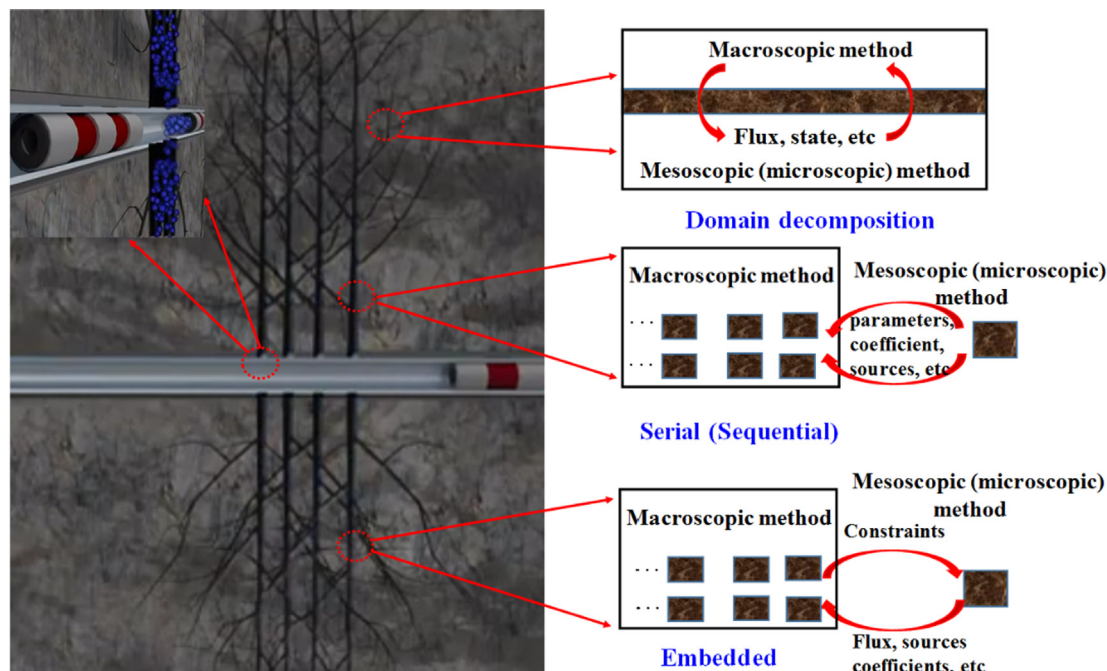


Fig. 26. Different multiscale methods in information exchange techniques during the shale gas production. Reprinted with permission from a modified version of Ref. [423].

information coupling exchange can be found in Ref. [423].

Acknowledgements

This work was supported by the National Natural Science Foundation of China (No. 51806178), the Fundamental Research Funds for the Central Universities (No. G2018KY0303), Natural Science Basic Research Plan in Shaanxi Province of China (No. 2019JQ-622) and the 111 Project (B16038). Hui Wang thanks Prof. David S Sholl for helpful discussions during a visit to his group at the Georgia Institute of Technology.

References

- [1] Wang Q, Li R. Research status of shale gas: a review. *Renew Sustain Energy Rev* 2017;74:715–20.
- [2] Middleton RS, Gupta R, Hyman JD, Viswanathan HS. The shale gas revolution: barriers, sustainability, and emerging opportunities. *Appl Energy* 2017;199:88–95.
- [3] Greco E, Aceleanu MI, Albulescu CT. The economic, social and environmental impact of shale gas exploitation in Romania: a cost-benefit analysis. *Renew Sustain Energy Rev* 2018;93:691–700.
- [4] Cooper J, Stamford L, Azapagic A. Economic viability of UK shale gas and potential impacts on the energy market up to 2030. *Appl Energy* 2018;215:577–90.
- [5] Yuan JH, Luo DK, Feng LY. A review of the technical and economic evaluation techniques for shale gas development. *Appl Energy* 2015;148:49–65.
- [6] Hammond GP, O'Grady Á. Indicative energy technology assessment of UK shale gas extraction. *Appl Energy* 2017;185:1907–18.
- [7] Lin BQ, Kuang YM. Natural gas subsidies in the industrial sector in China: National and regional perspectives. *Appl Energy* 2020;260:114329.
- [8] Yang Y, Wang L, Fang Y, Mou C. Integrated value of shale gas development: a comparative analysis in the United States and China. *Renew Sustain Energy Rev* 2017;76:1465–78.
- [9] Mevawala C, Jiang Y, Bhattacharyya D. Techno-economic optimization of shale gas to dimethyl ether production processes via direct and indirect synthesis routes. *Appl Energy* 2019;238:119–34.
- [10] Vengosh A, Jackson RB, Warner N, Darragh TH, Kondash A. A critical review of the risks to water resources from Unconventional shale gas development and hydraulic fracturing in the United States. *Environ Sci Technol* 2014;48:8334–48.
- [11] Castro-Alvarez F, Marsters P, Ponce de León Barido D, Kammen, DM. Sustainability lessons from shale development in the United States for Mexico and other emerging unconventional oil and gas developers. *Renew Sustain Energy Rev* 2018;82:1320–32.
- [12] King G. 2010. Thirty years of gas shale fracturing: what have we learned? SPE 133456. In: SPE annual technical conference and exhibition. Florence, Italy.
- [13] Nicot JP, Scanlon BR. Water use for shale-gas production in Texas. *U.S. Environ Sci Technol* 2012;46:3580–6.
- [14] Scanlon BR, Reedy RC, Nicot JP. Comparison of water use for hydraulic fracturing for unconventional oil and gas versus conventional oil. *Environ Sci Technol* 2014;48:12386–93.
- [15] Middleton RS, Carey JW, Currier RP, Hyman JD, Kang QJ, Karra S, et al. Shale gas and non-aqueous fracturing fluids: Opportunities and challenges for supercritical CO₂. *Appl Energy* 2015;147:500–9.
- [16] Li W, Wang C, Shi Z, Wei Y, Zhou H, Deng K. The description of shale reservoir pore structure based on method of moments estimation. *PLoS ONE* 2016;11:e0151631.
- [17] Saif T, Lin QY, Butcher AR, Bijeljic B, Blunt MJ. Multi-scale multi-dimensional microstructure imaging of oil shale pyrolysis using X-ray micro-tomography, automated ultra-high resolution SEM, MAPS Mineralogy and FIB-SEM. *Appl Energy* 2017;202:628–47.
- [18] Tian S, Wang T, Li G, Sheng M, Liu Q, Zhang S. An analytical model for shale gas transport in circular tube pores. *Int J Heat Mass Transf* 2018;127:321–8.
- [19] Wang F, Reed R. 2009. Pore networks and fluid flow in gas shales. SPE124253. In: Annual Technical Conference and Exhibition. New Orleans, Louisiana.
- [20] Sondergeld CH, Newsham KE, Comisky JT, Rice MC, Rai CS. 2010. Petrophysical considerations in evaluating and producing shale gas resources. In: SPE 131768. SPE Unconventional Gas Conference. Pittsburgh, Philadelphia, USA.
- [21] Javadpour F, Fisher D, Unsworth M. Nanoscale gas flow in shale gas sediments. *J Can Pet Technol* 2007;46:55–61.
- [22] Zhang L, Xiong Y, Li Y, Wei M, Jiang W, Lei R, et al. DFT modeling of CO₂ and Ar low-pressure adsorption for accurate nanopore structure characterization in organic-rich shales. *Fuel* 2017;204:1–11.
- [23] Cipolla CL, Lolon E, Mayerhofer MJ. 2009. Reservoir modeling and production evaluation in shale-gas reservoirs IPTC13185. In: International Petroleum Technology Conference. Doha, Qatar.
- [24] Bažant ZP, Salvatiato M, Chau VT, Viswanathan H, Zubelewicz A. Why fracking works. *J Appl Mech* 2014;81:101010.
- [25] Rijken P, Cooke ML. Role of shale thickness on vertical connectivity of fractures: application of crack-bridging theory to the Austin Chalk, Texas. *Tectonophysics* 2001;337:117–33.
- [26] Li P, Jiang Z, Zheng M, Bi H, Chen L. Estimation of shale gas adsorption capacity of the Longmaxi Formation in the Upper Yangtze Platform, China. *J Nat Gas Sci Eng* 2016;34:1034–43.
- [27] Burnham AK. Porosity and permeability of Green River oil shale and their changes during retorting. *Fuel* 2017;203:208–13.
- [28] Zhang LH, Shan BC, Zhao YL, Guo ZL. Review of micro seepage mechanisms in shale gas reservoirs. *Int J Heat Mass Transf* 2019;139:144–79.
- [29] Sutra E, Spada M, Burgherr P. Chemicals usage in stimulation processes for shale gas and deep geothermal systems: a comprehensive review and comparison. *Renew Sustain Energy Rev* 2017;77:1–11.
- [30] Curtis JB. Fractured shale-gas systems. *Aapg Bulletin* 2002;86:1921–38.
- [31] Wang Y, Zhu Y, Liu S, Zhang R. Methane adsorption measurements and modeling for organic-rich marine shale samples. *Fuel* 2016;172:301–9.
- [32] Dang W, Zhang JC, Tang X, Wei XL, Li ZM, Wang CH, et al. Investigation of gas content of organic-rich shale: a case study from Lower Permian shale in southern North China Basin, central China. *Geosci Front* 2018;9:559–75.
- [33] Rani S, Padmanabhan E, Prusty BK. Review of gas adsorption in shales for enhanced methane recovery and CO₂ storage. *J Petrol Sci Eng* 2019;175:634–43.
- [34] Guo C, Xu J, Wu K, Wei, Liu, S. Study on gas flow through nano pores of shale gas reservoirs. *Fuel* 2105;143:107–117.
- [35] Kaiser MJ. Profitability assessment of Haynesville shale gas wells. *Energy* 2012;38:315–30.
- [36] Ross DJK, Bustin RM. The importance of shale composition and pore structure upon gas storage potential of shale gas reservoirs. *Mar Pet Geol* 2009;26:916–27.
- [37] Javadpour F. Nanopores and apparent permeability of gas flow in mudrocks (shales and siltstone). *J Can Pet Technol* 2009;48:16–21.
- [38] Darabia H, Ettehada A, Javadpour F, Sepehrnoori K. Gas flow in ultra-tight shale strata. *J Fluid Mech* 2012;710:641–58.
- [39] Passey Q, Bohacs K, Esch W, Klimentidis R, Sinha S. 2010. From oil-prone source rock to gas-producing shale reservoir-geology and petrophysical characterization of unconventional shale-gas reservoirs, SPE 131350. In: CPS/SPE International Oil and Gas Conference and Exhibition in China. Beijing, China.
- [40] Zhang RH, Zhang LH, Wang RH, Zhao YL, Zhang DL. Research on transient flow theory of a multiple fractured horizontal well in a composite shale gas reservoir based on the finite-element method. *J Nat Gas Sci Eng* 2016;33:587–98.
- [41] Zhang T, Li X, Wang X, Li J, Sun Z, Feng D, et al. A discrete model for apparent gas permeability in nanoporous shale coupling initial water distribution. *J Nat Gas Sci Eng* 2018;59:80–96.
- [42] Yu H, Chen J, Zhu Y, Wang F, Wu H. Multiscale transport mechanism of shale gas in micro-/nano-pores. *Int J Heat Mass Transf* 2017;111:1172–80.
- [43] Gai H, Tian H, Cheng P, Zhou Q, Li T, Wang X, et al. Influence of retained bitumen in oil-prone shales on the chemical and carbon isotopic compositions of natural gases: implications from pyrolysis experiments. *Mar Pet Geol* 2019;101:148–61.
- [44] Han H, Cao Y, Chen SJ, Lu JG, Huang CX, Zhu HH, et al. Gao YInfluence of particle size on gas-adsorption experiments of shales: an example from a Longmaxi Shale sample from the Sichuan Basin, China. *Fuel* 2016;186:750–7.
- [45] Bhownilk S, Dutta P. A study on the effect of gas shale composition and pore structure on methane sorption. *J Nat Gas Sci Eng* 2019;62:144–56.
- [46] Wu T, Zhao H, Tesson S, Firoozabadi A. Absolute adsorption of light hydrocarbons and carbon dioxide in shale rock and isolated kerogen. *Fuel* 2019;235:855–67.
- [47] Shi J, Shen G, Zhao H, Sun N, Song X, Guo Y, et al. Porosity at the interface of organic matter and mineral components contribute significantly to gas adsorption on shales. *J CO₂ Utilization* 2018;28:73–82.
- [48] Klewiah I, Berawala DS, Walker HCA, Andersen PØ, Nadeau PH. Review of experimental sorption studies of CO₂ and CH₄ in shales. *J Nat Gas Sci Eng* 2020;73:103045.
- [49] Sondergeld CH, Ambrose RJ, Rai CS, Moncrieff J. 2010. Micro-structural studies of gas shales, SPE 131771. In: SPE Unconventional gas conference. Pittsburgh, Pennsylvania, USA.
- [50] Curtis ME, Ambrose RJ, Sondergeld CH. 2010. Structural characterization of gas shales on the micro- and nano-scales, SPE 137693. Canadian Unconventional Resources and International Petroleum Conference: Reservoir Description and Dynamics. Calgary, Alberta, Canada: Society of Petroleum Engineers.
- [51] Loucks RG, Reed RM, Ruppel SC, Jarvie DM. Morphology, genesis, and distribution of nanometer-scale pores in siliceous mudstones of the mississippian barnett shale. *Int J Sedim Res* 2009;79:848–61.
- [52] Loucks RG, Reed RM, Stephen C, Ruppel Hammes U. Spectrum of pore types and networks in mudrocks and a descriptive classification for matrix-related mudrock pores. *AAPG Bull* 2012;96:1071–98.
- [53] Milner M, McLin R, Petriello J. 2010. Imaging texture and porosity in mudstones and shales: comparison of secondary and ion-milled backscatter SEM methods, SPE-138975. In: CSUG/SPE Canadian Unconventional Resources and International Petroleum Conference, Calgary, Alberta, Canada.
- [54] Curtis ME, Cardott BJ, Sondergeld CH, Rai CS. Development of organic porosity in the Woodford Shale with increasing thermal maturity. *Int J Coal Geol* 2012;103:26–31.
- [55] Klaver J, Desbois G, Urai JL, Little R. BIB-SEM study of the pore space morphology in early mature posidonia shale from the Hils area, Germany. *Int J Coal Geol* 2012;103:12–25.
- [56] Loucks RG, Reed RM, Ruppel SC, Hammes U. Preliminary classification of matrix pores in mudrocks. *Gulf Coast Association of Geological Societies Transactions* 2010;60:435–41.
- [57] Wan Y, Pan Z, Tang S, Connell LD, Down DD, Camilleri M. An experimental investigation of diffusivity and porosity anisotropy of a Chinese gas shale. *J Nat Gas Sci Eng* 2015;23:70–9.
- [58] Jin X, Wang XQ, Yan WP, Meng SW, Liu XD, Jiao H, et al. Exploration and casting of large scale microscopic pathways for shale using electrodeposition. *Appl Energy* 2019;247:32–9.

- [59] Zhou S, Yan G, Xue H, Guo W, Li X. 2D and 3D nanopore characterization of gas shale in Longmaxi formation based on FIB-SEM. *Mar Pet Geol* 2016;73:174–80.
- [60] Xiong J, Liu X, Liang L. Experimental study on the pore structure characteristics of the Upper Ordovician Wufeng Formation shale in the southwest portion of the Sichuan Basin, China. *J Nat Gas Sci Eng* 2015;22:530–9.
- [61] Zheng X, Zhang B, Sanei H, Bao H, Meng Z, Wang C, et al. Pore structure characteristics and its effect on shale gas adsorption and desorption behavior. *Mar Pet Geol* 2019;100:165–78.
- [62] Saif T, Lin QY, Gao Y, Al-Khulaif Y, Marone F, Hollis D, et al. 4D in situ synchrotron X-ray tomographic microscopy and laser-based heating study of oil shale pyrolysis. *Appl Energy* 2019;235:1468–75.
- [63] Ma Y, Pan Z, Zhong N, Connell LD, Down DL, Lin W, et al. Experimental study of anisotropic gas permeability and its relationship with fracture structure of Longmaxi shales, Sichuan Basin, China. *Fuel* 2016;180:106–15.
- [64] Pan Z, Ma Y, Connell LD, Down DL, Camilleri M. Measuring anisotropic permeability using a cubic shale sample in a triaxial cell. *J Nat Gas Sci Eng* 2015;26:336–44.
- [65] Liu D, Yuan P, Liu HM, Li T, Tan DY, Yuan WW, et al. High-pressure adsorption of methane on montmorillonite, kaolinite and illite. *Appl Clay Sci* 2013;85:25–30.
- [66] Hu H, Zhang T, Wiggins-Camacho JD, Ellis GS, Lewan MD, Zhang X. Experimental investigation of changes in methane adsorption of bitumen-free Woodford Shale with thermal maturation induced by hydrous pyrolysis. *Mar Pet Geol* 2015;59:114–28.
- [67] Ji W, Song Y, Jiang Z, Wang X, Bai Y, Xing J. Geological controls and estimation algorithms of lacustrine shale gas adsorption capacity: a case study of the triassic strata in the southeastern Ordos Basin, China. *Int J Coal Geol* 2014;134:61–73.
- [68] Wang J, Wang B, Li Y, Yang Z, Gong H, Dong M. Measurement of dynamic adsorption-diffusion process of methane in shale. *Fuel* 2016;172:37–48.
- [69] Carrier B, Vandamme M, Pellenq RJM, Van DH. Elastic properties of swelling clay particles at finite temperature upon hydration. *J Phys Chem C* 2014;118:8933–43.
- [70] Zhao H, Wu T, Firoozabadi A. High pressure sorption of various hydrocarbons and carbon dioxide in Kimmeridge Blackstone and isolated kerogen. *Fuel* 2018;224:412–23.
- [71] Ettimin SR, Javadpour F, Maini BB, Chen Z. Measurement of gas storage processes in shale and of the molecular diffusion coefficient in kerogen. *Int J Coal Geol* 2014;123:10–9.
- [72] Xu H, Zhou W, Zhang R, Liu S, Zhou Q. Characterizations of pore, mineral and petrographic properties of marine shale using multiple techniques and their implications on gas storage capability for Sichuan Longmaxi gas shale field in China. *Fuel* 2019;241:360–71.
- [73] Zou J, Rezaee R, Liu K. Effect of temperature on methane adsorption in shale gas reservoirs. *Energy Fuels* 2017;31:12081–21292.
- [74] Sang Q, Li Y, Zhu C, Zhang SA, Dong M. Experimental investigation of shale gas production with different pressure depletion schemes. *Fuel* 2016;186:293–304.
- [75] Sang Q, Li Y, Yang Z, Zhu C, Yao J, Dong M. Experimental investigation of gas production processes in shale. *Int J Coal Geol* 2016;159:30–47.
- [76] Merey S. Analysis of the effect of experimental adsorption uncertainty on CH₄ production and CO₂ sequestration in Dadas shale gas reservoir by numerical simulations. *J Petrol Sci Eng* 2019;178:1051–66.
- [77] Gensterblum Y, Ghanizadeh A, Cuss RJ, Amann-Hildenbrand A, Krooss BM, Clarkson CR, et al. Gas transport and storage capacity in shale gas reservoirs - a review. Part A: transport processes. *J Unconventional Oil Gas Resour* 2015;12:87–122.
- [78] Wang H, Qu Z, Yin Y, Bai JQ, Yu B. Review of molecular simulation method for gas adsorption/desorption and diffusion in shale matrix. *J Therm Sci* 2019;28:1–6.
- [79] Liu X, Zhang D. A review of phase behavior simulation of hydrocarbons in confined space: Implications for shale oil and shale gas. *J Nat Gas Sci Eng* 2019;68:102901.
- [80] Wang J, Chen L, Kang Q, Rahman SS. The lattice Boltzmann method for isothermal micro-gaseous flow and its application in shale gas flow: a review. *Int J Heat Mass Transf* 2016;95:94–108.
- [81] Birdsell DT, Rajaram H, Dempsey D, Viswanathan HS. Hydraulic fracturing fluid migration in the subsurface: a review and expanded modeling results. *Water Resour Res* 2015;51:7159–88.
- [82] Wang L, Wang S, Zhang R, Wang C, Xiong Y, Zheng X, et al. Review of multi-scale and multi-physical simulation technologies for shale and tight gas reservoirs. *J Nat Gas Sci Eng* 2017;37:560–78.
- [83] Yunna W, Kaifeng C, Yisheng Y, Tiantian F. A system dynamics analysis of technology, cost and policy that affect the market competition of shale gas in China. *Renew Sustain Energy Rev* 2015;45:235–43.
- [84] Liu HH, Ranjith PG, Georgi DT, Lai BT. Some key technical issues in modelling of gas transport process in shales: a review. *Geomechanics and Geophysics for Geo-Energy and Geo-Resources* 2016;2:231–43.
- [85] Hyman JD, Jiménez-Martínez J, Viswanathan HS, Carey JW, Porter ML, Rougier E, et al. Understanding hydraulic fracturing: a multi-scale problem. *Philos Trans R Soc A: Math Phys Eng Sci* 2016;374:20150426.
- [86] Klaver J, Desbois G, Little R, Urai JL. BIB-SEM characterization of pore space morphology and distribution in postmatrix to overmatrix samples from the Haynesville and Bossier Shales. *Mar Pet Geol* 2015;59:451–66.
- [87] Britt L, Schoeffler J. 2009. The geomechanics of a shale play: what makes a shale prospective SPE 125525. In: SPE Eastern Regional Meeting, (Charleston, West Virginia).
- [88] Soliman MY, East LE, Augustine JR. 2010. Fracturing design aimed at enhancing fracture complexity. In: SPE EUROPEC/EAGE Annual Conference and Exhibition, (Barcelona, Spain).
- [89] Guo T, Zhang S, Qu Z, Zhou T, Xiao Y, Gao J. Experimental study of hydraulic fracturing for shale by stimulated reservoir volume. *Fuel* 2014;128:373–80.
- [90] Mosavat N, Hasamdarabadi B, Pourafshary P. Gaseous slip flow simulation in a micro/nano pore-throat structure using the lattice Boltzmann model. *J Petrol Sci Eng* 2019;177:93–103.
- [91] Yang Y, Wang K, Zhang L, Sun H, Zhang K, Ma J. Pore-scale simulation of shale oil flow based on pore network model. *Fuel* 2019;251:683–92.
- [92] Odoh SO, Cramer CJ, Truhlar DG, Gagliardi L. Quantum-chemical characterization of the properties and reactivities of metal-organic frameworks. *Chem Rev* 2015;115:6051–111.
- [93] Yuan Y, Rezaee R, Verrall M, Hu S-Y, Zou J, Testani N. Pore characterization and clay bound water assessment in shale with a combination of NMR and low-pressure nitrogen gas adsorption. *Int J Coal Geol* 2018;194:11–21.
- [94] Abdelrasoul A, Zhang H, Cheng C-H, Doan H. Applications of molecular simulations for separation and adsorption in zeolites. *Microporous Mesoporous Mater* 2017;242:294–348.
- [95] Evans JD, Fraux G, Gaillac R, Kohen D, Trouselet F, Vanson J-M, et al. Computational chemistry methods for nanoporous materials. *Chem Mater* 2017;29:199–212.
- [96] Yang Q, Liu D, Zhong C, Li JR. Development of computational methodologies for metal-organic frameworks and their application in gas separations. *Chem Rev* 2013;113:8261–323.
- [97] Huang S, Ding G, Wu Y, Huang H, Lan X, Zhang J. A semi-analytical model to evaluate productivity of shale gas wells with complex fracture networks. *J Nat Gas Sci Eng* 2018;50:374–83.
- [98] Ru X, Cheng Z, Song L, Wang H, Li J. Experimental and computational studies on the average molecular structure of Chinese Huadian oil shale kerogen. *J Mol Struct* 2012;1030:10–8.
- [99] Momma K, Izumi F. VESTA 3 for three-dimensional visualization of crystal, volumetric and morphology data. *J Appl Crystallogr* 2011;44:1272–6.
- [100] Momma K, Izumi F. VESTA: a three-dimensional visualization system for electronic and structural analysis. *J Appl Crystallogr* 2008;41:653–8.
- [101] Pan S, Wang Q, Bai J, Chi M, Cui D, Wang Z, et al. Molecular structure and electronic properties of oil shale kerogen: an experimental and molecular modeling study. *Energy Fuels* 2018;32:12394–404.
- [102] Guan X-H, Liu Y, Wang D, Wang Q, Chi M-S, Liu S, et al. Three-dimensional structure of a huadian oil shale kerogen model: an experimental and theoretical study. *Energy & Fuel* 2015;29:4122–36.
- [103] Qajar A, Daigle H, Prodanović M. The effects of pore geometry on adsorption equilibrium in shale formations and coal-beds: Lattice density functional theory study. *Fuel* 2016;163:205–13.
- [104] Wei M, Zhang L, Xiong Y, Li J, Peng PA. Nanopore structure characterization for organic-rich shale using the non-local-density functional theory by a combination of N₂ and CO₂ adsorption. *Microporous Mesoporous Mater* 2016;227:88–94.
- [105] Hantal G, Brochard L, Dias Soeiro Cordeiro MN, Ulm FJ, Pellenq RJM. Surface chemistry and atomic-scale reconstruction of kerogen-silica composites. *J Phys Chem C* 2018;118:2429–38.
- [106] Zhang B, He G, Shan Y, He H. Experimental and DFT study of the adsorption of N₂O on transition ion-exchanged ZSM-5. *Catal Today* 2019;327:177–81.
- [107] Sun W, Li H, Li H, Li S, Cao X. Adsorption mechanisms of ibuprofen and naproxen to UiO-66 and UiO-66-NH₂: batch experiment and DFT calculation. *Chem Eng J* 2019;360:645–53.
- [108] Amaya-Roncancio S, García Blanco AA, Linares DH, Sapag K. DFT study of hydrogen adsorption on Ni/graphene. *Appl Surf Sci* 2018;447:254–60.
- [109] Wales DJ, Doye JPK. Global optimization by basin-hopping and the lowest energy structures of Lennard-Jones clusters containing up to 110 Atoms. *J Phys Chem A* 1997;101:5111–6.
- [110] Calvo F, Doye JPK, Wales DJ. Quantum partition functions from classical distributions: application to rare-gas clusters. *J Chem Phys* 2001;114:7312–29.
- [111] Schaef HT, Glezakou VA, Owen AT, Ramprasad S, Martin PF, McGrail BP. Surface Condensation of CO₂ onto Kaolinite. *Environ Sci Technol Lett* 2014;1:142–5.
- [112] Wang S, Zhou G, Ma Y, Gao L, Song R, Jiang G, et al. Molecular dynamics investigation on the adsorption behaviors of H₂O, CO₂, CH₄ and N₂ gases on calcite (110) surface. *Appl Surf Sci* 2016;385:616–21.
- [113] Chen J, Min F-F, Liu L-Y, Liu C-F. Mechanism research on surface hydration of kaolinite, insights from DFT and MD simulations. *Appl Surf Sci* 2019;476:6–15.
- [114] Sun H, Zhao H, Qi N, Li Y. Molecular insights into the enhanced shale gas recovery by carbon dioxide in kerogen slit nanopores. *J Phys Chem C* 2017;121:10233–41.
- [115] Chen G, Lu S, Liu K, Han T, Xu C, Xue Q, et al. GCMC simulations on the adsorption mechanisms of CH₄ and CO₂ in K-ilite and their implications for shale gas exploration and development. *Fuel* 2018;224:521–8.
- [116] Liu Y, Li HA, Tian Y, Jin Z, Deng H. Determination of the absolute adsorption/desorption isotherms of CH₄ and n-C₄H₁₀ on shale from a nano-scale perspective. *Fuel* 2018;218:67–77.
- [117] Liu Y, Wilcox J. CO₂ adsorption on carbon models of organic constituents of gas shale and coal. *Environ Sci Technol* 2011;45:809–14.
- [118] Liu X-Q, Xue Y, Tian Z-Y, Mo J-J, Qiu N-X, Chu W, et al. Adsorption of CH₄ on nitrogen- and boron-containing carbon models of coal predicted by density-functional theory. *Appl Surf Sci* 2013;285:190–7.
- [119] Zhu Y-Q, Su H, Jing Y, Guo J, Tang J. Methane adsorption on the surface of a model of shale: a density functional theory study. *Appl Surf Sci* 2016;387:379–84.
- [120] Qajar A, Daigle H, Prodanović M. Methane dual-site adsorption in organic-rich shale-gas and coalbed systems. *Int J Coal Geol* 2015;149:1–8.
- [121] Li T, Tian H, Chen J, Cheng L. Application of low pressure gas adsorption to the characterization of pore size distribution of shales: an example from Southeastern Chongqing area, China. *J Natural Gas Geosci* 2016;1:221–30.
- [122] Huo P, Zhang D, Yang Z, Li W, Zhang J, Jia S. CO₂ geological sequestration: displacement behavior of shale gas methane by carbon dioxide injection. *Int J*

- Greenhouse Gas Control 2017;66:48–59.
- [123] Liu JL, Xi S, Chapman Walter G. Competitive sorption of CO₂ with gas mixtures in nanoporous shale for enhanced gas recovery from density functional theory. *Langmuir* 2019;35:8144–58.
- [124] Wu Y-S, Li J, Ding D, Wang C, Di Y. A generalized framework model for the simulation of gas production in unconventional gas reservoirs. SPE-163609-PA 2014;19: 845–857.
- [125] Yang T, Li X, Zhang D. Quantitative dynamic analysis of gas desorption contribution to production in shale gas reservoirs. *J Unconventional Oil Gas Resour* 2015;9:18–30.
- [126] Huang L, Ning Z, Wang Q, Zhang W, Cheng Z, Wu X, et al. Effect of organic type and moisture on CO₂/CH₄ competitive adsorption in kerogen with implications for CO₂ sequestration and enhanced CH₄ recovery. *Appl Energy* 2018;210:28–43.
- [127] Chen G, Lu S, Zhang J, Xue Q, Han T, Xue H, et al. Keys to linking GCMC simulations and shale gas adsorption experiments. *Fuel* 2017;199:14–21.
- [128] Zhai Z, Wang X, Jin X, Sun L, Li J, Cao D. Adsorption and diffusion of shale gas reservoirs in modeled clay minerals at different geological depths. *Energy Fuels* 2014;28:7467–73.
- [129] Chen G, Zhang J, Lu S, Pervukhina M, Dewhurst DN. Adsorption behavior of hydrocarbon on illite. *Energy Fuels* 2016;30:9114–912.
- [130] Xiong J, Liu X, Liang L, Zeng Q. Adsorption behavior of methane on kaolinite. *Ind Eng Chem Res* 2017;56:6229–38.
- [131] Croteau T, Bertram AK, Patey GN. Water adsorption on kaolinite surfaces containing trenches. *J Phys Chem A* 2010;114:2171–8.
- [132] Aljamaan H, Al Ismail M, Kovsek AR. Experimental investigation and Grand Canonical Monte Carlo simulation of gas shale adsorption from the macro to the nano scale. *J Nat Gas Sci Eng* 2017;48:119–37.
- [133] Sun H, Zhao H, Qi N, Qi X, Zhang K, Sun W, et al. Mechanistic insight into the displacement of CH₄ by CO₂ in calcite slit-nanopores: the effect of competitive adsorption. *RSC Advance* 2016;6:104456–62.
- [134] Wang H, Qu ZG, Zhang W, Chang YX, He YL. Experimental and numerical study of CO₂ adsorption on Ni/DOBDC metal-organic framework. *Appl Therm Eng* 2014;73:1501–9.
- [135] Dubbeldam D, Calero S, Ellis DE, Snurr RQ. RASPA: molecular simulation software for adsorption and diffusion in flexible nanoporous materials. *Mol Simul* 2016;42:81–101.
- [136] Dubbeldam D, Torres-Knoop A, Walton KS. On the inner workings of Monte Carlo codes. *Mol Simul* 2013;39:1253–92.
- [137] Frenkel D, Smit B, Ratner MA. Understanding Molecular Simulation: From Algorithms to Applications. Academic Press, Inc.; 1996.
- [138] Tan SL, Loi QK, Do DD, Nicholson D. On the canonical isotherms for bulk fluid, surface adsorption and adsorption in pores: a common thread. *J Colloid Interface Sci* 2019;548:25–36.
- [139] Chen C, Ozcan A, Yazaydin AO, Ladewig BP. Gas permeation through single-crystal ZIF-8 membranes. *J Membr Sci* 2019;575:209–16.
- [140] Wang H, Qu ZG, Zhou L. Coupled GCMC and LBM simulation method for visualizations of CO₂/CH₄ gas separation through Cu-BTC membranes. *J Membr Sci* 2018;550:448–61.
- [141] Wang H, Qu ZG, Zhang W, Yu QN, He YL. Experimental and numerical study of CO₂ adsorption on copper benzene-1,3,5-tricarboxylate (Cu-BTC) metal organic framework. *Int J Heat Mass Transf* 2016;92:859–63.
- [142] Zhai Z, Wang X, Jin X, Sun L, Li J, Cao D. Adsorption and diffusion of shale gas reservoirs in modeled clay minerals at different geological depths. *Energy Fuels* 2014;28:7467–73.
- [143] Wang S, Feng Q, Ming Z, Javadpour F, Hu Q. Supercritical methane diffusion in shale nanopores: effects of pressure, mineral types, and moisture content. *Energy Fuels* 2017;32:169–80.
- [144] Liu J, Xie H, Wang Q, Chen S, Hu Z. The effect of pore size on shale gas recovery with CO₂ sequestration: insight into molecular mechanisms. *Energy Fuels* 2019;33:2897–907.
- [145] Chen G, Lu S, Liu K, Xue Q, Han T, Xu C, et al. Critical factors controlling shale gas adsorption mechanisms on different minerals investigated using GCMC simulations. *Mar Pet Geol* 2019;100:31–42.
- [146] Xiong J, Liu K, Liu X, Liang L, Zeng Q. Molecular simulation of methane adsorption in slit-like quartz pores. *RSC Adv* 2016;6:110808–19.
- [147] Zhou W, Zhang Z, Wang H, Yan Y, Liu X. Molecular insights into competitive adsorption of CO₂/CH₄ mixture in shale nanopores. *RSC Adv* 2018;8:33939–46.
- [148] Zhang J, Clennell MB, Liu K, Pervukhina M, Chen G, Dewhurst DN. Methane and carbon dioxide adsorption on illite. *Energy Fuels* 2016;30:10643–52.
- [149] Ho TA, Wang Y, Criscenti LJ. Chemo-mechanical coupling in kerogen gas adsorption/desorption. *PCCP* 2018;20:12390–5.
- [150] Lin K, Yuan Q, Zhao Y-P. Using graphene to simplify the adsorption of methane on shale in MD simulations. *Comput Mater Sci* 2017;133:99–107.
- [151] Zhang H, Zeng X, Zhao Z, Zhai Z, Cao D. Adsorption and selectivity of CH₄/CO₂ in functional group rich organic shales. *J Nat Gas Sci Eng* 2017;39:82–9.
- [152] Zhao T, Li X, Ning Z, Zhao H, Li M. Molecular simulation of methane adsorption on type II kerogen with the impact of water content. *J Petrol Sci Eng* 2018;161:302–10.
- [153] Vasileiadis M, Peristeras LD, Papavasileiou KD, Economou IG. Transport properties of shale gas in relation to kerogen porosity. *J Phys Chem C* 2018;122:6166–77.
- [154] Wang T, Tian S, Li G, Sheng M, Ren W, Liu Q, et al. Molecular Simulation of CO₂/CH₄ Competitive Adsorption on Shale Kerogen for CO₂ Sequestration and Enhanced Gas Recovery. *J Phys Chem C* 2018;122:17009–18.
- [155] Ho TA, Wang Y, Xiong Y, Criscenti LJ. Differential retention and release of CO₂ and CH₄ in kerogen nanopores: implications for gas extraction and carbon sequestration. *Fuel* 2018;220:1–7.
- [156] Yang N, Liu S, Yang X. Molecular simulation of preferential adsorption of CO₂ over CH₄ in Na-montmorillonite clay material. *Appl Surf Sci* 2015;356:1262–71.
- [157] Rao Q, Leng Y. Methane aqueous fluids in montmorillonite clay interlayer under natural geological conditions: a grand canonical Monte Carlo and molecular dynamics simulation study. *J Phys Chem B* 2014;118:10956–65.
- [158] Makaremi M, Jordan KD, Guthrie GD, Myshakin EM. Multiphase monte carlo and molecular dynamics simulations of water and CO₂ intercalation in montmorillonite and beidellite. *J Phys Chem C* 2015;119:15112–24.
- [159] Jin Z, Firoozabadi A. Effect of water on methane and carbon dioxide sorption in clay minerals by Monte Carlo simulations. *Fluid Phase Equilib* 2014;382:10–20.
- [160] Wang S, Feng Q, Javadpour F, Hu Q, Wu K. Competitive adsorption of methane and ethane in montmorillonite nanopores of shale at supercritical conditions: a grand canonical Monte Carlo simulation study. *Chem Eng J* 2019;355:76–90.
- [161] Zhang T, Ellis GS, Ruppel SC, Milliken K, Yang R. Effect of organic-matter type and thermal maturity on methane adsorption in shale-gas systems. *Org Geochem* 2012;47:120–31.
- [162] Yuan W, Li X, Pan Z, Connell LD, Li S, He J. Experimental investigation of interactions between water and a lower silurian Chinese shale. *Energy Fuels* 2014;28:4925–33.
- [163] Kadoura A, Narayanan Nair AK, Sun S. Adsorption of carbon dioxide, methane, and their mixture by montmorillonite in the presence of water. *Microporous Mesoporous Mater* 2016;225:331–41.
- [164] Wang Q, Huang L. Molecular insight into competitive adsorption of methane and carbon dioxide in montmorillonite: effect of clay structure and water content. *Fuel* 2019;239:32–43.
- [165] Li W, Pang X, Snape C, Zhang B, Zheng D, Zhang X. A molecular simulation study on methane adsorption capacity and mechanism in clay minerals: effect of clay type, pressure and water saturation in shales. *Energy Fuels* 2019;33(2):765–78.
- [166] Zhang H, Cao DP. Molecular simulation of displacement of shale gas by carbon dioxide at different geological depths. *Chem Eng Sci* 2016;156:121–7.
- [167] Zhang J, Liu K, Clennell MB, Dewhurst DN, Pervukhina M. Molecular simulation of CO₂/CH₄ competitive adsorption and induced clay swelling. *Fuel* 2015;160:309–17.
- [168] Huang H, Sun W, Xiong F, Chen L, Li X, Gao T, et al. A novel method to estimate subsurface shale gas capacities. *Fuel* 2018;232:341–50.
- [169] Zhang L, Liu C, Li QB. Molecular simulations of competitive adsorption behavior between CH₄-C₂H₆ in K-illite clay at supercritical conditions. *Fuel* 2020;260:116358.
- [170] Hao Y, Yuan L, Li P, Zhao W, Li D, Lu D. Molecular simulations of methane adsorption behavior in illite nanopores considering basal and edge surfaces. *Energy Fuels* 2018;32:4783–96.
- [171] Zhang B, Kang J, Kang T. Monte Carlo simulations of methane adsorption on kaolinite as a function of pore size. *J Nat Gas Sci Eng* 2018;49:410–6.
- [172] Sun H, Sun W, Zhao H, Sun Y, Zhang D, Qi X, et al. Adsorption properties of CH₄ and CO₂ in quartz nanopores studied by molecular simulation. *RSC Adv* 2016;6:32770–8.
- [173] Vandenbroucke M, Largeau C. Kerogen origin, evolution and structure. *Org Geochem* 2007;38:719–833.
- [174] Hu H. Methane adsorption comparison of different thermal maturity kerogens in shale gas system. *Chin J Geochem* 2014;33:425–30.
- [175] Li Y, Hu Z, Liu X, Duan X, Gao S, Wang W, et al. Pressure-dependent equilibrium molecular simulation of shale gas and its distribution and motion characteristics in organic-rich nano-slits. *Fuel* 2019;237:1040–9.
- [176] Xiong J, Liu X, Liang L, Zeng Q. Adsorption of methane in organic-rich shale nanopores: an experimental and molecular simulation study. *Fuel* 2017;200:299–315.
- [177] Bousige C, Gimbleau CM, Vix-Guterl C, Pomerantz AE, Suleimenova A, Vaughan G, et al. Realistic molecular model of kerogen's nanostructure. *Nat Mater* 2016;15:576–82.
- [178] Liu Y, Zhu Y, Li W, Xiang J, Wang Y, Li J, et al. Molecular simulation of methane adsorption in shale based on grand canonical Monte Carlo method and pore size distribution. *J Nat Gas Sci Eng* 2016;30:119–26.
- [179] Li Z-Z, Min T, Kang Q, He Y-L, Tao W-Q. Investigation of methane adsorption and its effect on gas transport in shale matrix through microscale and mesoscale simulations. *Int J Heat Mass Transf* 2016;98:675–86.
- [180] Li Y, Hu Z, Liu X, Gao S, Duan X, Chang J, et al. Insights into interactions and microscopic behavior of shale gas in organic-rich nano-slits by molecular simulation. *J Nat Gas Sci Eng* 2018;59:309–25.
- [181] Wang T, Tian S, Li G, Sheng M. Selective adsorption of supercritical carbon dioxide and methane binary mixture in shale kerogen nanopores. *J Nat Gas Sci Eng* 2018;50:181–8.
- [182] Zhou B, Xu R, Jiang P. Novel molecular simulation process design of adsorption in realistic shale kerogen spherical pores. *Fuel* 2016;180:718–26.
- [183] Yu H, Fan J, Chen J, Zhu Y, Wu H. Pressure-dependent transport characteristic of methane gas in slit nanopores. *Int J Heat Mass Transf* 2018;123:657–67.
- [184] Wang ZH, Hu SD, Guo P, Meng WJ, Ou ZP, Xiao C, Qiu SF. Molecular simulations of the adsorption of shale gas in organic pores. *Mater Res Innovations* 2015;19.
- [185] He J, Ju Y, Kulasiński K, Zheng L, Lammers L. Molecular dynamics simulation of methane transport in confined organic nanopores with high relative roughness. *J Nat Gas Sci Eng* 2019;62:202–13.
- [186] Ju Y, He J, Chang E, Zheng L. Quantification of CH₄ adsorption capacity in kerogen-rich reservoir shales: an experimental investigation and molecular dynamic simulation. *Energy* 2019;170:411–22.
- [187] Jiang W, Lin M. Molecular dynamics investigation of conversion methods for excess adsorption amount of shale gas. *J Nat Gas Sci Eng* 2018;49:241–9.
- [188] Michalec L, Lfsal M. Molecular simulation of shale gas adsorption onto overmature

- type II model kerogen with control microporosity. *Mol Phys* 2017;115:1086–103.
- [189] Song R, Cui M. Molecular simulation on competitive adsorption mechanism of CH₄/CO₂ on shale kerogen. *Arabian J Geosci* 2018;11:403.
- [190] Wu T, Firoozabadi A. Effect of microstructural flexibility on methane flow in kerogen matrix by molecular dynamics simulations. *The Journal of Physical Chemistry C* 2019;123:10874–80.
- [191] Trobec R, Janezic D. Comparison of parallel verlet and implicit runge-kutta methods for molecular dynamics integration. *J Chem Inf Comput Sci* 1995;35:100–5.
- [192] Chen W-H, Wu C-H, Cheng H-C. Modified Nosé-Hoover thermostat for solid state for constant temperature molecular dynamics simulation. *J Comput Phys* 2011;230:6354–66.
- [193] Li Y, Hu Z, Duan X, Wang X, Shi J, Zhan H. The general form of transport diffusivity of shale gas in organic-rich nano-slits-A molecular simulation study using darken approximation. *Fuel* 2019;249:457–71.
- [194] Sun H, Zhao H, Qi N, Qi X, Zhang K, Li Y. Molecular insight into the micro-behaviors of CH₄ and CO₂ in montmorillonite slit-nanopores. *Mol Simul* 2017;43:1004–11.
- [195] Kadoura A, Narayanan Nair AK, Sun S. Molecular dynamics simulations of carbon dioxide, methane, and their mixture in montmorillonite clay hydrates. *J Phys Chem C* 2016;120:12517–29.
- [196] Wang H, Wang X, Jin X, Cao D. Molecular dynamics simulation of diffusion of shale oils in montmorillonite. *J Phys Chem C* 2016;120:8986–91.
- [197] Sharma A, Namsani S, Singh JK. Molecular simulation of shale gas adsorption and diffusion in inorganic nanopores. *Mol Simul* 2015;41:414–22.
- [198] Wang S, Feng Q, Ming Z, Javadpour F, Hu Q. Supercritical methane diffusion in shale nanopores: effects of pressure, mineral types, and moisture content. *Energy Fuels* 2017;32(1):169–80.
- [199] Zhang B, Kang J, Kang T. Molecular simulation of methane adsorption and its effect on kaolinite swelling as functions of pressure and temperature. *Mol Simul* 2018;44:789–96.
- [200] Nan YL, Li WH, Jin ZH. Slip length of methane flow under shale reservoir conditions: effect of pore size and pressure. *Fuel* 2020;259:116237.
- [201] Zheng J, Wang Z, Gong W, Ju Y, Wang M. Characterization of nanopore morphology of shale and its effects on gas permeability. *J Nat Gas Sci Eng* 2017;47:83–90.
- [202] Chen J, Wang F, Liu H, Wu H. Molecular mechanism of adsorption/desorption hysteresis: dynamics of shale gas in nanopores. *Sci China Phys Mech Astronomy* 2016;60:014611.
- [203] Song X, Guo Y, Zhang J, Sun N, Shen G, Chang X, et al. Fracturing with carbon dioxide: from microscopic mechanism to reservoir Application. *Joule* 2019;3(8):1913–26.
- [204] Urban JJ. Emerging scientific and engineering opportunities within the water-energy nexus. *Joule* 2017;1:665–88.
- [205] Yuan Q, Zhu X, Lin K, Zhao Y-P. Molecular dynamics simulations of the enhanced recovery of confined methane with carbon dioxide. *PCCP* 2015;17:31887–93.
- [206] Zeng K, Jiang P, Lun Z, Xu R. Molecular simulation of carbon dioxide and methane adsorption in shale organic nanopores. *Energy Fuels* 2019;33(3):1785–96.
- [207] Wu T, Zhang D. Impact of adsorption on gas transport in nanopores. *Sci Rep* 2016;6:23629.
- [208] Kazemi M, Takbiri-Borujeni A. Flow of gases in organic nanoscale channels: a boundary-driven molecular simulation study. *Energy Fuels* 2016;30(10):8156–63.
- [209] Barisik M, Beskok A. Scale effects in gas nano flows. *Phys Fluids* 2014;26:052003.
- [210] Xue Q, Tao Y, Liu Z, Lu S, Li X, Wu T, et al. Mechanism of oil molecules transportation in nano-sized shale channel: MD simulation. *RSC Adv* 2015;5:25684–92.
- [211] Liu B, Qi C, Zhao X, Teng G, Zhao L, Zheng H, et al. Nanoscale Two-phase flow of methane and water in shale inorganic matrix. *J Phys Chem C* 2018;122:26671–9.
- [212] Lee T, Boquet L, Coasne B. Activated desorption at heterogeneous interfaces and long-time kinetics of hydrocarbon recovery from nanoporous media. *Nature Communication* 2016;7:11890.
- [213] Sun Z, Shi J, Wu K, Xu B, Zhang T, Chang Y, et al. Transport capacity of gas confined in nanoporous ultra-tight gas reservoirs with real gas effect and water storage mechanisms coupling. *Int J Heat Mass Transf* 2018;126:1007–18.
- [214] Yin Y, Qu ZG, Zhang JF. An analytical model for shale gas transport in kerogen nanopores coupled with real gas effect and surface diffusion. *Fuel* 2017;210:569–77.
- [215] Ren J, Guo P, Guo Z, Wang Z. A lattice Boltzmann model for simulating gas flow in kerogen pores. *Transp Porous Media* 2015;106:285–301.
- [216] Zhang X, Xiao L, Shan X, Guo L. Lattice Boltzmann simulation of shale gas transport in organic nano-pores. *Sci Rep* 2014;4:4843.
- [217] Yin Y, Qu ZG, Zhang JF. Pore-scale prediction of the effective mass diffusivity of heterogeneous shale structure using the lattice Boltzmann method. *Int J Heat Mass Transf* 2019;133:976–85.
- [218] Ren J, Zheng Q, Guo P, Peng S, Wang Z, Du J. Pore-scale lattice Boltzmann simulation of two-component shale gas flow. *J Nat Gas Sci Eng* 2019;61:46–70.
- [219] Yin Y, Qu ZG, Zhang JF. Multiple diffusion mechanisms of shale gas in nanoporous organic matter predicted by the local diffusivity lattice Boltzmann model. *Int J Heat Mass Transf* 2019;143:118571.
- [220] Succi S, Foti E, Higuera F. Three-dimensional flows in complex geometries with the Lattice Boltzmann Method. *EPL (Europhysics Letters)* 1989;10:433.
- [221] Chen S, Doolen GD. Lattice Boltzmann method for fluid flows. *Annu Rev Fluid Mech* 1998;30:329–64.
- [222] Yan YY, Zu YQ, Dong B. LBM, a useful tool for mesoscale modelling of single-phase and multiphase flow. *Appl Therm Eng* 2011;31:649–55.
- [223] Zhang T, Li X, Wang X, Li J, Li W, Zhao W, et al. Modelling the water transport behavior in organic-rich nanoporous shale with generalized lattice Boltzmann method. *Int J Heat Mass Transf* 2018;127:123–34.
- [224] Qiu L-C, Tian L, Liu X-J, Han Y. A 3D multiple-relaxation-time LBM for modeling landslide-induced tsunami waves. *Eng Anal Boundary Elem* 2019;102:51–9.
- [225] Mountrakis L, Lorenz E, Malaspina O, Alwayyed S, Chopard B, Hoekstra AG. Parallel performance of an IB-LBM suspension simulation framework. *J Comput Sci* 2015;9:45–50.
- [226] Ma B, Shi L, Huang C, Xu Q. Effects of nanoscale pore structure on permeability and relative permeability loss analyzed by GPU enhanced Multiple-Relaxation-Time LBM. *Int J Heat Mass Transf* 2018;117:584–94.
- [227] Li Q, He YL, Tang GH, Tao WQ. Lattice Boltzmann modeling of microchannel flows in the transition flow regime. *Microfluid Nanofluid* 2011;10:607–18.
- [228] Manjhi N, Verma N, Salem K, Mewes D. Lattice Boltzmann modelling of unsteady-state 2D concentration profiles in adsorption bed. *Chem Eng Sci* 2006;61:2510–21.
- [229] Nie X, Doolen G, Chen S. Lattice-Boltzmann simulations of fluid flows in MEMS. *J Stat Phys* 2002;107:279–89.
- [230] Tang GH, Tao WQ, He YL. Lattice Boltzmann method for gaseous microflows using kinetic theory boundary conditions. *Phys Fluids* 2005;17:058101.
- [231] Zhang Y, Qin R, Emerson DR. Lattice Boltzmann simulation of rarefied gas flows in microchannels. *Phys Rev E* 2005;71:047702.
- [232] Zhang Y-H, Gu X-J, Barber RW, Emerson DR. Capturing Knudsen layer phenomena using a lattice Boltzmann model. *Phys Rev E* 2006;74:046704.
- [233] Guo ZL, Zhao TS, Shi Y. Physical symmetry, spatial accuracy, and relaxation time of the lattice Boltzmann equation for microgas flows. *J Appl Phys* 2006;99:074903.
- [234] Guo ZL, Shi BC, Zheng CG. An extended Navier-Stokes formulation for gas flows in the Knudsen layer near a wall. *EPL (Europhysics Letters)* 2007;80:24001.
- [235] Maxwell JC. On stresses in rarified gases arising from inequalities of temperature. *Philos Trans R Soc Lond* 1879;170:3411–21.
- [236] Dongari N, Agrawal A, Agrawal A. Analytical solution of gaseous slip flow in long microchannels. *Int J Heat Mass Transf* 2007;50:3411–21.
- [237] Langmuir I. The adsorption of gases on plane surfaces of glass, mica and platinum. *J Am Chem Soc*; 40:1361–403.
- [238] Myong RS. A generalized hydrodynamic computational model for rarefied and microscale diatomic gas flows. *J Comput Phys* 2004;195:655–76.
- [239] Succi S. Mesoscopic Modeling of slip motion at fluid-solid interfaces with heterogeneous catalysis. *Phys Rev Lett* 2002;89:064502.
- [240] Guo Z, Shi B, Zhao TS, Zheng C. Discrete effects on boundary conditions for the lattice Boltzmann equation in simulating microscale gas flows. *Phys Rev E* 2007;76:056704.
- [241] Guo Z, Zheng C, Shi B. Lattice Boltzmann equation with multiple effective relaxation times for gaseous microscale flow. *Phys Rev E* 2008;77:036707.
- [242] Chen S, Tian Z. Simulation of microchannel flow using the lattice Boltzmann method. *Physica A* 2009;388:4803–10.
- [243] Zhang W-M, Meng G, Wei X. A review on slip models for gas microflows. *Microfluid Nanofluid* 2012;13:845–82.
- [244] Zhang J. Lattice Boltzmann method for microfluidics: models and applications. *Microfluid Nanofluid* 2011;10:1–28.
- [245] Gupta N, Fathi E, Belyadi F. Effects of nano-pore wall confinements on rarefied gas dynamics in organic rich shale reservoirs. *Fuel* 2018;220:120–9.
- [246] Knudsen M. Effusion and the molecular flow of gases through openings. *Ann Phys* 1909;333:75–130.
- [247] Kast W, Hohenhanner CR. Mass transfer within the gas-phase of porous media. *Int J Heat Mass Transf* 2000;43:807–23.
- [248] Thorstenson DC, Pollock DW. Gas transport in unsaturated zones: multicomponent systems and the adequacy of Fick's laws. *Water Resour Res* 1989;25:477–507.
- [249] Heidi JG, McMahon JJ, Nielsen RF, Yuster ST. Study of the permeability of rocks to homogeneous fluids, API50230: Drilling and Production Practice. New York, New York, USA: American Petroleum Institute; 1950. p. 230–46.
- [250] Loeb LB. The kinetic theory of gases, 2Ed. New York: McGraw-Hill Co., Inc.; 2004.
- [251] Freeman CM, Moridis GJ, Blasingame TA. A numerical study of microscale flow behavior in tight gas and shale gas reservoir systems. *Transp Porous Media* 2011;90:253–68.
- [252] Fathi E, Akkutlu IY. Lattice Boltzmann Method for simulation of shale gas transport in kerogen. *SPE J* 2013;18(01):27–37.
- [253] Fathi E, Tinni A, Akkutlu IY. Correction to Klinkenberg slip theory for gas flow in nano-capillaries. *Int J Coal Geol* 2012;103:51–9.
- [254] Li X, Fan J, Yu H, Zhu Y, Wu H. Lattice Boltzmann method simulations about shale gas flow in contracting nano-channels. *Int J Heat Mass Transf* 2018;122:1210–21.
- [255] Landry CJ, Prodanović M, Eichhubl P. Direct simulation of supercritical gas flow in complex nanoporous media and prediction of apparent permeability. *Int J Coal Geol* 2016;159:120–34.
- [256] Chen L, Zhang L, Kang Q, Viswanathan HS, Yao J, Tao W. Nanoscale simulation of shale transport properties using the lattice Boltzmann method: permeability and diffusivity. *Sci Rep* 2015;5:8089.
- [257] Chen L, Kang Q, Pawar R, He Y-L, Tao W-Q. Pore-scale prediction of transport properties in reconstructed nanostructures of organic matter in shales. *Fuel* 2015;158:650–8.
- [258] Zhao J, Yao J, Zhang M, Zhang L, Yang Y, Sun H, et al. Study of gas flow characteristics in tight porous media with a microscale lattice Boltzmann Model. *Sci Rep* 2016;6:32393.
- [259] Zhao J, Yao J, Li A, Zhang M, Zhang L, Yang Y, et al. Simulation of microscale gas flow in heterogeneous porous media based on the lattice Boltzmann method. *J Appl Phys* 2016;120:084306.
- [260] Song W, Yao J, Ma J, Couples GD, Li Y, Sun H. Pore-scale numerical investigation into the impacts of the spatial and pore-size distributions of organic matter on shale gas flow and their implications on multiscale characterisation. *Fuel*

- 2018;216:707–21.
- [261] Wang Z, Jin X, Wang X, Sun L, Wang M. Pore-scale geometry effects on gas permeability in shale. *J Nat Gas Sci Eng* 2016;34:948–57.
- [262] Wang Z, Guo Y, Wang M. Permeability of high-Kn real gas flow in shale and production prediction by pore-scale modeling. *J Nat Gas Sci Eng* 2016;28:328–37.
- [263] Mengal SA, Wattenbarger RA. Accounting for adsorbed gas in shale gas reservoirs. SPE Middle East Oil and Gas Show and Conference. Manama, Bahrain: Society of Petroleum Engineers; 2011.
- [264] Xiong X, Devegowda D, Michel Villazon GG, Sigal RF, Civan F. 2012. A fully-coupled free and adsorptive phase transport model for shale gas reservoirs including non-darcy flow effects. In: SPE Annual Technical Conference and Exhibition, (San Antonio, Texas, USA: Society of Petroleum Engineers).
- [265] Qu ZG, Yin Y, Wang H, Zhang JF. Pore-scale investigation on coupled diffusion mechanisms of free and adsorbed gases in nanoporous organic matter. *Fuel* 2020;260:116423.
- [266] Allan A, Mavko G. The effect of adsorption and Knudsen diffusion on the steady-state permeability of microporous rocks. *Geophysics* 2013;78:75–83.
- [267] Zhao T, Zhao H, Li X, Ning Z, Wang Q, Zhao W, et al. Pore scale characteristics of gas flow in shale matrix determined by the regularized lattice Boltzmann method. *Chem Eng Sci* 2018;187:245–55.
- [268] Zuo H, Deng S-C, Li H-B. Boundary scheme for lattice Boltzmann modeling of micro-scale gas flow in organic-rich pores considering surface diffusion. *Chin Phys B* 2019;28:030202.
- [269] Sm C, Dani O. Lattice Boltzmann method for modeling liquid-vapor interface configurations in porous media. *Water Resour Res* 2004;40:W01509.
- [270] Ning Y, Jiang Y, Liu H, Qin G. Numerical modeling of slippage and adsorption effects on gas transport in shale formations using the lattice Boltzmann method. *J Nat Gas Sci Eng* 2015;26:345–55.
- [271] Ning Y, He S, Chen T, Jiang Y, Qin G. Simulation of shale gas transport in 3D complex nanoscale-pore structures using the Lattice Boltzmann Method. SPE Asia Pacific Unconventional Resources Conference and Exhibition. Brisbane, Australia: Society of Petroleum Engineers; 2015.
- [272] Ning Y, He S, Liu H, Wang H, Qin G. 2016. Permeability prediction considering surface diffusion for gas shales by Lattice Boltzmann simulations on multi-scale reconstructed digital rocks. In: International Petroleum Technology Conference, (Bangkok, Thailand: International Petroleum Technology Conference).
- [273] Ning Y, He S, Liu H, Wang H, Qin G. 2016. Upscaling in Numerical Simulation of Shale Transport Properties by Coupling Molecular Dynamics Simulation with Lattice Boltzmann Method. In: SPE/AAPG/SEG Unconventional Resources Technology Conference, (San Antonio, Texas, USA: Unconventional Resources Technology Conference).
- [274] Zhang T, Sun S. A coupled Lattice Boltzmann approach to simulate gas flow and transport in shale reservoirs with dynamic sorption. *Fuel* 2019;246:196–203.
- [275] Zhao J, Yao J, Zhang L, Sui H, Zhang M. Pore-scale simulation of shale gas production considering the adsorption effect. *Int J Heat Mass Transf* 2016;103:1098–107.
- [276] Sang G, Elsworth D, Miao X, Mao X, Wang J. Numerical study of a stress dependent triple porosity model for shale gas reservoirs accommodating gas diffusion in kerogen. *J Nat Gas Sci Eng* 2016;32:423–38.
- [277] Bezyan Y, Ebadi M, Gerami S, Rafati R, Sharifi M, Koroteev D. A novel approach for solving nonlinear flow equations: the next step towards an accurate assessment of shale gas resources. *Fuel* 2019;236:622–35.
- [278] Wang X, Sheng JJ. Multi-scaled pore network modeling of gas-water flow in shale formations. *J Petrol Sci Eng* 2019;177:899–908.
- [279] Mi L, Jiang H, Li J. The impact of diffusion type on multiscale discrete fracture model numerical simulation for shale gas. *J Nat Gas Sci Eng* 2014;20:74–81.
- [280] Li G, Meng Z. A preliminary investigation of CH₄ diffusion through gas shale in the Paleozoic Longmaxi Formation, Southern Sichuan Basin, China. *J Nat Gas Sci Eng* 2016;36:1220–7.
- [281] Zou J, Rezaee R, Yuan Y. Investigation on the adsorption kinetics and diffusion of methane in shale samples. *J Petrol Sci Eng* 2018;171:951–8.
- [282] Zhang M, Ayala LF. Variable rate and pressure integral solutions to the nonlinear gas diffusivity equation in unconventional systems. *Fuel* 2019;235:1100–13.
- [283] Yang Z, Wang W, Dong M, Wang J, Li Y, Gong H, et al. A model of dynamic adsorption-diffusion for modeling gas transport and storage in shale. *Fuel* 2016;173:115–28.
- [284] Gao F, Liu J, Wang JG, Ju Y, Leung CF. Impact of micro-scale heterogeneity on gas diffusivity of organic-rich shale matrix. *J Nat Gas Sci Eng* 2017;45:75–87.
- [285] Bai J, Kang Y, Chen M, Liang L, You L, Li X. Investigation of multi-gas transport behavior in shales via a pressure pulse method. *Chem Eng J* 2019;360:1667–77.
- [286] Obliger A, Ulm F-J, Pellenq R. Impact of nanoporosity on hydrocarbon transport in shales' organic matter. *Nano Lett* 2018;18:832–7.
- [287] Yao J, Sun H, Fan D-Y, Wang C-C, Sun Z-X. Numerical simulation of gas transport mechanism in tight shale gas reservoirs. *Pet Sci* 2013;10:528–37.
- [288] Klinkenberg LJ. The permeability of porous media to liquids and gases. Paper presented at: Drilling and Production Practice. New York, New York, USA: American Petroleum Institute; 1941.
- [289] Jones FO, Owens WW. A laboratory study of low-permeability gas sands. *J Petrol Technol* 1980;32:1631–40.
- [290] Sampath K, Keighin C. Factors affecting gas slippage in tight sandstones of cretaceous age in the Uinta basin. *J Petrol Technol* 1982;34:2715–20.
- [291] Florence F A, Rushing JA, Newsham KE, Blasingame TA. 2007. Improved permeability prediction relations for low permeability sands, SPE 107954. In: Paper presented at: SPE Rocky Mountain Oil & Gas Technology Symposium: Flow in Porous Media (Denver, Colorado, USA, Society of Petroleum Engineers).
- [292] Beskok A, Karniadakis G. Report: a model for flows in channels, pipes, and ducts at micro and nano scales. *Microscale Thermophys Eng* 1999;3:43–77.
- [293] Civan F. Effective correlation of apparent gas permeability in tight porous media. *Transport Porous Med* 2010;82:375–84.
- [294] Wu K, Li X, Wang C, Yu W, Chen Z. Model for surface diffusion of adsorbed gas in nanopores of shale gas reservoirs. *Ind Eng Chem Res* 2015;54:3225–36.
- [295] Birdsell DT, Rajaram H, Lackey G. Imbibition of hydraulic fracturing fluids into partially saturated shale. *Water Resour Res* 2015;51:6787–96.
- [296] Zhang T, Li X, Li J, Feng D, Li P, Zhang Z, et al. Numerical investigation of the well shut-in and fracture uncertainty on fluid-loss and production performance in gas-shale reservoirs. *J Nat Gas Sci Eng* 2017;46:421–35.
- [297] Kim J, Moridis GJ. Numerical analysis of fracture propagation during hydraulic fracturing operations in shale gas systems. *Int J Rock Mech Min Sci* 2015;76:127–37.
- [298] Ziarani AS, Aguilera R. Knudsen's permeability correction for tight porous media. *Transport Porous Med* 2012;91:239–60.
- [299] Afsharpour A, Javadpour F. Liquid slip flow in a network of shale noncircular nanopores. *Fuel* 2016;180:580–90.
- [300] Song W, Yao J, Li Y, Sun H, Zhang L, Yang Y, et al. Apparent gas permeability in an organic-rich shale reservoir. *Fuel* 2016;181:973–84.
- [301] Wang Y, Liu S, Zhao Y. Modeling of permeability for ultra-tight coal and shale matrix: a multi-mechanistic flow approach. *Fuel* 2018;232:60–70.
- [302] Zhang T, Li X, Sun Z, Feng D, Miao Y, Li P, et al. An analytical model for relative permeability in water-wet nanoporous media. *Chem Eng Sci* 2017;174:1–12.
- [303] Zhang T, Li X, Li J, Feng D, Wu K, Shi J, et al. A fractal model for gas-water relative permeability in inorganic shale with nanoscale pores. *Transp Porous Media* 2018;122:305–31.
- [304] Singh H, Javadpour F. Langmuir slip-Langmuir sorption permeability model of shale. *Fuel* 2016;164:28–37.
- [305] Alfi M, Hosseini SA, Enriquez D, Zhang T. A new technique for permeability calculation of core samples from unconventional gas reservoirs. *Fuel* 2019;235:301–5.
- [306] Fink R, Krooss BM, Gensterblum Y, Amann-Hildenbrand A. Apparent permeability of gas shales -Superposition of fluid-dynamic and poro-elastic effects. *Fuel* 2017;199:532–50.
- [307] Zhang Y, Li D, Sun X, Song Z, Shi D, Su Y. A new model for calculating the apparent permeability of shale gas in the real state. *Nat Gas Ind B* 2018;5:245–52.
- [308] Feng Q, Xu S, Wang S, Li Y, Gao F, Xu Y. Apparent permeability model for shale oil with multiple mechanisms. *J Petrol Sci Eng* 2019;175:814–27.
- [309] Sun Z, Li X, Shi J, Zhang T, Sun F. Apparent permeability model for real gas transport through shale gas reservoirs considering water distribution characteristic. *Int J Heat Mass Transf* 2017;115:1008–19.
- [310] Guo B, Ma L, Tchelapi HA. Image-based micro-continuum model for gas flow in organic-rich shale rock. *Adv Water Resour* 2018;122:70–84.
- [311] Song W, Yao J, Ma J, Li Y, Han W. A pore structure based real gas transport model to determine gas permeability in nanoporous shale. *Int J Heat Mass Transf* 2018;126:151–60.
- [312] Peng Y, Liu J, Pan Z, Qu H, Connell L. Evolution of shale apparent permeability under variable boundary conditions. *Fuel* 2018;215:46–56.
- [313] Song W, Yao B, Yao J, Li Y, Sun H, Yang Y, et al. Methane surface diffusion capacity in carbon-based capillary with application to organic-rich shale gas reservoir. *Chem Eng J* 2018;352:644–54.
- [314] Chen D, Pan Z, Ye Z. Dependence of gas shale fracture permeability on effective stress and reservoir pressure: Model match and insights. *Fuel* 2015;139:383–92.
- [315] Li M, Yin G, Xu J, Cao J, Song Z. Permeability evolution of shale under anisotropic true triaxial stress conditions. *Int J Coal Geol* 2016;165:142–8.
- [316] Tahmasebi P, Javadpour F, Sahimi M. Stochastic shale permeability matching: Three-dimensional characterization and modeling. *Int J Coal Geol* 2016;165:231–42.
- [317] Cui G, Liu J, Wei M, Shi R, Elsworth D. Why shale permeability changes under variable effective stresses: new insights. *Fuel* 2018;213:55–71.
- [318] Kazemi M, Takbiri-Borujeni A. An analytical model for shale gas permeability. *Int J Coal Geol* 2015;146:188–97.
- [319] Ling K, He J, Pei P, Ge J, Qin W. A new correlation to evaluate the fracture permeability changes as reservoir is depleted. *J Petrol Sci Eng* 2016;145:336–45.
- [320] Zhang Q, Liu Y, Chen T, Yu X, Wang J, Wang T. Simulations of methane partial oxidation by CFD coupled with detailed chemistry at industrial operating conditions. *Chem Eng Sci* 2016;142:126–36.
- [321] Geng L, Li G, Zitha P, Tian S, Sheng M. A fractal permeability model for shale gas flow through heterogeneous matrix systems. *J Nat Gas Sci Eng* 2016;35:593–604.
- [322] Bai F, Sun Y, Liu Y, Guo M. Evaluation of the porous structure of Huadian oil shale during pyrolysis using multiple approaches. *Fuel* 2017;187:1–8.
- [323] Sheng G, Javadpour F, Su Y. Effect of microscale compressibility on apparent porosity and permeability in shale gas reservoirs. *Int J Heat Mass Transf* 2018;120:56–65.
- [324] Cao P, Liu J, Leong Y-K. A fully coupled multiscale shale deformation-gas transport model for the evaluation of shale gas extraction. *Fuel* 2016;178:103–17.
- [325] Bustin AMM, Bustin RM. Importance of rock properties on the producibility of gas shales. *Int J Coal Geol* 2012;103:132–47.
- [326] Houben ME, Desbois G, Urai JL. Pore morphology and distribution in the Shaly facies of Opalinus Clay (Mont Terri, Switzerland): Insights from representative 2D BIB-SEM investigations on mm to nm scale. *Appl Clay Sci* 2013;71:82–97.
- [327] Houben ME, Desbois G, Urai JL. A comparative study of representative 2D microstructures in Shaly and Sandy facies of Opalinus Clay (Mont Terri, Switzerland) inferred from BIB-SEM and MIP methods. *Mar Pet Geol* 2014;49:143–61.
- [328] Wang M, Wang J, Pan N, Chen S. Mesoscopic predictions of the effective thermal conductivity for microscale random porous media. *Phys Rev E* 2007;75:036702.

- [329] Naraghi ME, Javadpour F. A stochastic permeability model for the shale-gas systems. *Int J Coal Geol* 2015;140:111–24.
- [330] Wang JJ, Kang QJ, Chen L, Rahman SS. Pore-scale lattice Boltzmann simulation of micro-gaseous flow considering surface diffusion effect. *Int J Coal Geol* 2017;169:62–73.
- [331] Nithiarasu P, Seetharamu KN, Sundararajan T. Natural convective heat transfer in a fluid saturated variable porosity medium. *Int J Heat Mass Transf* 1997;40:3955–67.
- [332] Wang M, Pan N, Wang J, Chen S. Mesoscopic simulations of phase distribution effects on the effective thermal conductivity of microgranular porous media. *J Colloid Interface Sci* 2007;311:562–70.
- [333] Chen L, Kang Q, Dai Z, Viswanathan HS, Tao WQ. Permeability prediction of shale matrix reconstructed using the elementary building block model. *Fuel* 2015;160:346–56.
- [334] Wang J, Chen L, Kang Q, Rahman SS. Apparent permeability prediction of organic shale with generalized lattice Boltzmann model considering surface diffusion effect. *Fuel* 2016;181:478–90.
- [335] Lorincz P, Burns AD, Lesnic D, Fisher QJ, Crook AJ, Grattoni C, et al. Modelling of gas flow in shale using a finite volume method. *Appl Math Model* 2017;49:394–414.
- [336] Sun F, Yao Y, Li G, Dong M. Transport behaviors of real gas mixture through nanopores of shale reservoir. *J Petrol Sci Eng* 2019;177:1134–41.
- [337] You Y, Han X, Wang X, Jiang X. Evolution of gas and shale oil during oil shale kerogen pyrolysis based on structural characteristics. *J Anal Appl Pyrol* 2019;138:203–10.
- [338] Fan D, Etehadtavakkol A. Semi-analytical modeling of shale gas flow through fractal induced fracture networks with microseismic data. *Fuel* 2017;193:444–59.
- [339] Wu Y, Cheng L, Huang S, Bai Y, Jia P, Wang S, et al. An approximate semi-analytical method for two-phase flow analysis of liquid-rich shale gas and tight light-oil wells. *J Petrol Sci Eng* 2019;176:562–72.
- [340] Lu M, Pan Z, Connell LD, Lu Y. A coupled, non-isothermal gas shale flow model: Application to evaluation of gas-in-place in shale with core samples. *J Petrol Sci Eng* 2017;158:361–79.
- [341] Kim J, Jang Y, Seoomon H, Sung W. The sorption-corrected multiwell deconvolution method to identify shale gas reservoir containing sorption gas. *J Petrol Sci Eng* 2017;159:717–23.
- [342] Xu C, Li P, Lu Z, Liu J, Lu D. Discrete fracture modeling of shale gas flow considering rock deformation. *J Nat Gas Sci Eng* 2018;52:507–14.
- [343] Cai J, Lin D, Singh H, Wei W, Zhou S. Shale gas transport model in 3D fractal porous media with variable pore sizes. *Mar Pet Geol* 2018;98:437–47.
- [344] Zhao Y-L, Zhang L-H, Shan B-C. Mathematical model of fractured horizontal well in shale gas reservoir with rectangular stimulated reservoir volume. *J Nat Gas Sci Eng* 2018;59:67–79.
- [345] Wang X, Sheng JJ. Pore network modeling of the Non-Darcy flows in shale and tight formations. *J Petrol Sci Eng* 2018;163:511–8.
- [346] Li Y, Kalantari-Dahaghi A, Zolfaghari A, Dong P, Negahban S, Zhou D. Fractal-based real gas flow model in shales: An interplay of nano-pore and nano-fracture networks. *Int J Heat Mass Transf* 2018;127:1188–202.
- [347] Hao Y, Wang W, Yuan B, Su Y, An J, Shu H. Shale gas simulation considering natural fractures, gas desorption, and slippage flow effects using conventional modified model. *J Pet Explor Prod Technol* 2018;8:607–15.
- [348] Akkutlu IY, Efendiev YI, Savatorova V. Multi-scale asymptotic analysis of gas transport in shale matrix. *Transp Porous Media* 2015;107:235–60.
- [349] Yan B, Wang Y, Killough JE. Beyond dual-porosity modeling for the simulation of complex flow mechanisms in shale reservoirs. *Comput Geosci* 2016;20:69–91.
- [350] Kudapa V K, Gupta DK, Sharma P. Modeling of gas flow within the shale fracture network. Springer Singapore); Singapore; 2018.
- [351] Hu X, Yu W, Liu M, Wang M, Wang W. A multiscale model for methane transport mechanisms in shale gas reservoirs. *J Petrol Sci Eng* 2019;172:40–9.
- [352] Cao C, Zhao Q, Gao C, Sun J, Xu J, Zhang P, et al. Discrete fracture model with multi-field coupling transport for shale gas reservoirs. *J Petrol Sci Eng* 2017;158:107–19.
- [353] Song H, Yu M, Zhu W, Wu P, Lou Y, Wang Y, et al. Numerical investigation of gas flow rate in shale gas reservoirs with nanoporous media. *Int J Heat Mass Transf* 2015;80:626–35.
- [354] Ali I, Malik NA. A realistic transport model with pressure-dependent parameters for gas flow in tight porous media with application to determining shale rock properties. *Transp Porous Media* 2018;124:723–42.
- [355] Akkutlu IY, Efendiev Y, Vasilyeva M, Wang Y. Multiscale model reduction for shale gas transport in poroelastic fractured media. *J Comput Phys* 2018;353:356–76.
- [356] Takbiri-Borujeni A, Fathi E, Kazemi M, Belyadi F. An integrated multiscale model for gas storage and transport in shale reservoirs. *Fuel* 2019;237:1228–43.
- [357] Yan B, Mi L, Wang Y, Tang H, An C, Killough JE. Multi-porosity multi-physics compositional simulation for gas storage and transport in highly heterogeneous shales. *J Petrol Sci Eng* 2018;160:498–509.
- [358] Yu H, Zhu Y, Jin X, Liu H, Wu H. Multiscale simulations of shale gas transport in micro/nano-porous shale matrix considering pore structure influence. *J Nat Gas Sci Eng* 2019;64:28–40.
- [359] Liu LJ, Xiao J, Sun H, Huang ZQ, Yan X, Li LL. Compositional modeling of shale condensate gas flow with multiple transport mechanisms. *J Petrol Sci Eng* 2019;172:1186–201.
- [360] Li B, Su Y, Li X, Wang W, Husein MM, Aguilera R. Temporal scale analysis of shale gas dynamic coupling flow. *Fuel* 2019;239:587–600.
- [361] Wu K, Chen Z, Li X, Guo C, Wei M. A model for multiple transport mechanisms through nanopores of shale gas reservoirs with real gas effect-adsorption-mechanic coupling. *Int J Heat Mass Transf* 2016;93:408–26.
- [362] Bear J. Dynamics of fluids in porous media. New York: Elsevier; 1972.
- [363] Nordahl K, Ringrose P. Identifying the representative elementary volume for permeability in heterolithic deposits using numerical rock models. *Math Geosci* 2008;40:753–71.
- [364] Keller LM, Holzer L, Schuetz P, Gasser P. Pore space relevant for gas permeability in Opalinus clay: Statistical analysis of homogeneity, percolation, and representative volume element. *J Geophys Res* 2013;118:2799–812.
- [365] Saraji S, Piri M. The representative sample size in shale oil rocks and nano-scale characterization of transport properties. *Int J Coal Geol* 2015;146:42–54.
- [366] Chen C, Hu D, Westacott D, Loveless D. Nanometer-scale characterization of microscopic pores in shale kerogen by image analysis and pore-scale modeling. *Geochem Geophys Geosy* 2013;14:4066–75.
- [367] Zhang D, Zhang R, Chen S, Soll WE. Pore scale study of flow in porous media: Scale dependency, REV, and statistical REV. *J Geophys Res* 2000;27:1195–8.
- [368] Chen L, Fang W, Kang Q, De'Haven Hyman J, Viswanathan HS, Tao W-Q. Generalized lattice Boltzmann model for flow through tight porous media with Klinkenberg's effect. *Phys Rev E* 2015;91:033004.
- [369] Zhao J, Fu D, Li Y, Jiang Y, Xu W, Chen X. REV-scale simulation of gas transport in shale matrix with lattice Boltzmann method. *J Nat Gas Sci Eng* 2018;57:224–37.
- [370] Zhang T, Li X, Yin Y, He M, Liu Q, Huang L, et al. The transport behaviors of oil in nanopores and nanoporous media of shale. *Fuel* 2019;242:305–15.
- [371] Fathi E, Akkutlu IY. Multi-component gas transport and adsorption effects during CO₂ injection and enhanced shale gas recovery. *Int J Coal Geol* 2014;123:52–61.
- [372] Aplin AC, Matenaar IF, McCarty DK, van der Pluijm BA. Influence of mechanical compaction and clay mineral diagenesis on the microfabric and pore-scale properties of deep-water gulf of Mexico mudstones. *Clays Clay Miner* 2006;54:500–14.
- [373] Osholake T, Yilin Wang J, Ertekin T. Factors affecting hydraulically fractured well performance in the marcellus shale gas reservoirs. *J Energy Res Technol* 2012;135.
- [374] Cao P, Liu J, Leong Y-K. A multiscale-multiphase simulation model for the evaluation of shale gas recovery coupled the effect of water flowback. *Fuel* 2017;199:191–205.
- [375] Heller R, Zoback M. Adsorption of methane and carbon dioxide on gas shale and pure mineral samples. *Journal of Unconventional Oil and Gas Resources* 2014;8:14–24.
- [376] Zhu H, Tang X, Liu Q, Li K, Xiao J, Jiang S, et al. 4D multi-physical stress modelling during shale gas production: a case study of Sichuan Basin shale gas reservoir, China. *J Petrol Sci Eng* 2018;167:929–43.
- [377] Li Q, Li P, Pang W, Li D, Liang H, Lu D. A new method for production data analysis in shale gas reservoirs. *J Nat Gas Sci Eng* 2018;56:368–83.
- [378] Li J, Wu K, Chen Z, Wang W, Yang B, Wang K, et al. Effects of energetic heterogeneity on gas adsorption and gas storage in geologic shale systems. *Appl Energy* 2019;251:113368.
- [379] Umeozor EC, Jordaan SM, Gates ID. On methane emissions from shale gas development. *Energy* 2018;152:594–600.
- [380] Yuan J, Jiang R, Cui Y, Xu J, Wang Q, Zhang W. The numerical simulation of thermal recovery considering rock deformation in shale gas reservoir. *Int J Heat Mass Transf* 2019;138:719–28.
- [381] Zou C, Zhao Q, Dong D, Yang Z, Qiu Z, Liang F, et al. Geological characteristics, main challenges and future prospect of shale gas. *J Nat Gas Geosci* 2017;2:273–88.
- [382] Liu Q, Chen Y, Wang W, Liu H, Hu X, Xie Y. A productivity prediction model for multiple fractured horizontal wells in shale gas reservoirs. *J Nat Gas Sci Eng* 2017;42:252–61.
- [383] Chen Y, Jiang S, Zhang D, Liu C. An adsorbed gas estimation model for shale gas reservoirs via statistical learning. *Appl Energy* 2017;197:327–41.
- [384] Crow DJG, Giarola S, Hawkes AD. A dynamic model of global natural gas supply. *Appl Energy* 2018;218:452–69.
- [385] Chen KP, Shen D. Mechanism of fluid production from the nanopores of shale. *Mech Res Commun* 2018;88:34–9.
- [386] Huang JW, Jin TY, Barrufet M, Killough J. Evaluation of CO₂ injection into shale gas reservoirs considering dispersed distribution of kerogen. *Appl Energy* 2020;260:114285.
- [387] Zhang KQ, Jia N, Li SY, Liu LR. Static and dynamic behavior of CO₂ enhanced oil recovery in shale reservoirs: experimental nanofluidics and theoretical models with dual-scale nanopores. *Appl Energy* 2019;255:113752.
- [388] Ho TA, Criscienti LJ, Wang Y. Nanostructural control of methane release in kerogen and its implications to wellbore production decline. *Sci Rep* 2016;6:28053.
- [389] Wang Y, Liao B, Qiu L, Wang D, Xue Q. Numerical simulation of enhancing shale gas recovery using electrical resistance heating method. *Int J Heat Mass Transf* 2019;128:1218–28.
- [390] Yu W, Luo Z, Javadpour F, Varavei A, Sepehrnoori K. Sensitivity analysis of hydraulic fracture geometry in shale gas reservoirs. *J Petrol Sci Eng* 2014;113:1–7.
- [391] Peng Y, Liu J, Pan Z, Connell LD. A sequential model of shale gas transport under the influence of fully coupled multiple processes. *J Nat Gas Sci Eng* 2015;27:808–21.
- [392] Tahmasebi P, Javadpour F, Sahimi M. Multiscale and multiresolution modeling of shales and their flow and morphological properties. *Sci Rep* 2015;5:16373.
- [393] Geng L, Li G, Wang M, Li Y, Tian S, Pang W, et al. A fractal production prediction model for shale gas reservoirs. *J Nat Gas Sci Eng* 2018;55:354–67.
- [394] Zhu G-P, Yao J, Sun H, Zhang M, Xie M-J, Sun Z-X, et al. The numerical simulation of thermal recovery based on hydraulic fracture heating technology in shale gas reservoir. *J Nat Gas Sci Eng* 2016;28:305–16.
- [395] Luo S, Zeng L, Xu D, Kathe M, Chung E, Deshpande N, et al. Shale gas-to-syngas chemical looping process for stable shale gas conversion to high purity syngas with a H₂: CO ratio of 2: 1. *Energy Environ Sci* 2014;7:4104–17.
- [396] Patwardhan SD, Famoori F, Gunaji RG, Govindarajan SK. Simulation and mathematical modeling of stimulated shale gas reservoirs. *Ind Eng Chem Res*

- 2014;53:19788–805.
- [397] Gu M, Dao E, Mohanty KK. Investigation of ultra-light weight proppant application in shale fracturing. *Fuel* 2015;150:191–201.
- [398] You X-T, Liu J-Y, Jia C-S, Li J, Liao X-Y, Zheng A-W. Production data analysis of shale gas using fractal model and fuzzy theory: Evaluating fracturing heterogeneity. *Appl Energy* 2019;250:1246–59.
- [399] Miao Y, Li X, Lee J, Zhou Y, Wu K, Sun Z, et al. A new rate-decline analysis of shale gas reservoirs: coupling the self-diffusion and surface diffusion characteristics. *J Petrol Sci Eng* 2018;163:166–76.
- [400] Guo B, Shan J, Feng Y. Productivity of blast-fractured wells in liquid-rich shale gas formations. *J Nat Gas Sci Eng* 2014;18:360–7.
- [401] Li Y, Liu G, Li J, Yu L, Zhang T, Lu J. Improving fracture initiation predictions of a horizontal wellbore in laminated anisotropy shales. *J Nat Gas Sci Eng* 2015;24:390–9.
- [402] Wang J, Luo H, Liu H, Lin J, Li L, Lin W. Influences of adsorption/desorption of shale gas on the apparent properties of matrix pores. *Pet Explor Dev* 2016;43:158–65.
- [403] Zhang L, Anderson N, Dilmore R, Soeder DJ, Bromhal G. Leakage detection of marcellus shale natural gas at an upper devonian gas monitoring well: a 3-D numerical modeling approach. *Environ Sci Technol* 2014;48:10795–803.
- [404] Lu T, Liu S, Li Z. A new approach to model shale gas production behavior by considering coupled multiple flow mechanisms for multiple fractured horizontal well. *Fuel* 2019;237:283–97.
- [405] Zhang W, Xu J, Jiang R. Production forecast of fractured shale gas reservoir considering multi-scale gas flow. *J Pet Explor Prod Technol* 2017;7:1071–83.
- [406] Hu Y, Li Z, Zhao J, Tao Z, Gao P. Prediction and analysis of the stimulated reservoir volume for shale gas reservoirs based on rock failure mechanism. *Environmental Earth Sciences* 2017;76:546.
- [407] Russian A, Gouze P, Dentz M, Gringarten A. Multi-continuum approach to modelling shale gas extraction. *Transp Porous Media* 2015;109:109–30.
- [408] Novotny AA, Murad MA, Lima SA. An adjoint-based optimization method for gas production in shale reservoirs. *Acta Geotech* 2018;13:833–52.
- [409] Wang W, Yao J, Sun H, Song W-H. Influence of gas transport mechanisms on the productivity of multi-stage fractured horizontal wells in shale gas reservoirs. *Pet Sci* 2015;12:664–73.
- [410] Arredondo-Ramírez K, Ponce-Ortega JM, El-Halwagi MM. Optimal planning and infrastructure development for shale gas production. *Energy Convers Manage* 2016;119:91–100.
- [411] Jain A, Ong SP, Hautier G, Chen W, Richards WD, Dacek S, et al. Commentary: the materials project: a materials genome approach to accelerating materials innovation. *APL Mater* 2013;1:011002.
- [412] Chung YG, Gómez-Gualdrón DA, Li P, Leperi KT, Deria P, Zhang H, et al. In silico discovery of metal-organic frameworks for precombustion CO₂ capture using a genetic algorithm. *Sci Adv* 2016;2:e1600909.
- [413] Collins SP, Daff TD, Piotrkowski SS, Woo TK. Materials design by evolutionary optimization of functional groups in metal-organic frameworks. *Sci Adv* 2016;2:e1600954.
- [414] Boyd P, Lee Y, Smit B. Computational development of the nanoporous materials genome. *Nature Reviews Material* 2017;2:17037.
- [415] Keskin S. Screening for selectivity. *Nature. Energy* 2019. <https://doi.org/10.1038/s41560-019-0514-z>.
- [416] Simon CM, Kim J, Gomez-Gualdrón DA, Camp JS, Chung YG, Martin RL, et al. The materials genome in action: identifying the performance limits for methane storage. *Energy Environ Sci* 2015;8:1190–9.
- [417] Lan Y, Han X, Tong M, Huang H, Yang Q, Liu D, et al. Materials genomics methods for high-throughput construction of COFs and targeted synthesis. *Nat Commun* 2018;9:5274.
- [418] Wu YK, Misra S, Sondergeld C, Curtis M, Jernigen J. Machine learning for locating organic matter and pores in scanning electron microscopy images of organic-rich shales. *Fuel* 2019;253:662–76.
- [419] Kamrava S, Tahmasebi P, Sahimi M. Enhancing images of shale formations by a hybrid stochastic and deep learning algorithm. *Neural Networks* 2019;118:310–20.
- [420] Wang SH, Chen Z, Chen SN. Applicability of deep neural networks on production forecasting in Bakken shale reservoirs. *J Petrol Sci Eng* 2019;179:112–25.
- [421] Striolo A, Cole DR. Understanding shale gas: recent progress and remaining challenges. *Energy Fuels* 2017;31:10300–10.
- [422] Sharma S, Agrawal V, Akondi RN. Role of biogeochemistry in efficient shale oil and gas production. *Fuel* 2020;259:116207.
- [423] Tong Z-X, He Y-L, Tao W-Q. A review of current progress in multiscale simulations for fluid flow and heat transfer problems: the frameworks, coupling techniques and future perspectives. *Int J Heat Mass Transf* 2019;137:1263–89.